Department of Information Engineering

Padova University, Padova, Italy

Ph.D. School on Information Engineering

Section: *Bioengineering* - Cycle: *XXVI*

Quantitative neuroimaging of perfusion with arterial spin labeling: deconvolution and physiology-based models

Headmaster of the school: Prof. Matteo Bertocco

Supervisor: Prof. Alessandra Bertoldo

PhD candidate: Marco Castellaro

To Sabrina

Quantitative neuroimaging of perfusion with arterial spin labeling: deconvolution and physiology-based models

ABSTRACT

Perfusion studies with Magnetic Resonance Imaging (MRI) techniques traditionally require the injection of exogenous contrast agents. Arterial Spin Labeling (ASL) technique permits to use water contained in the blood as an endogenous contrast agent, reducing the intrinsic invasively process required by this kind of examination.Furthermore it increases patient's comfort and reduces cost effective of perfusion measurements in clinical environment. This key feature allows to estimate perfusion in particular patients, like children or in case of allergy to the tracer. Another advantage is the possibility to monitor perfusion levels over time and since the quantification process allows to estimate perfusion in absolute unit, it is possible to easily compare subjects in longitudinal studies.

The organization of this thesis is composed by an introductive section, in which the principles of ASL are introduced (Chapter 1) and more general MRI concepts are reviewed (Chapter 2). Chapter 3 will cover the existing MRI sequences used to perform the labeling and how it is possible to measure its traveling through tissues.

Chapter 4 describes state-of-the-art for the quantification process. Models are required in this process in order to accurately describe the labeling and the readout steps. The most used model to perform quantification has been proposed by Buxton et al. (1998). However, this model

simplifies the tracer kinetics reducing the exchange phenomena to a simple mono compartment model. Other more complex models have been presented, which can take into account the capillary system (Parkes and Tofts, 2002) or the macro vascular component in major arteries (Chappell et al., 2010). Estimators usually employed with Buxton model are non linear least squares. However, in the last years also Bayesian framework has been proposed, based on a Variational Bayes approach (Chappell et al., 2009).

The creation of new ASL sequences like Quantitative Star Labeling of Arterial Region (QUASAR) (Petersen et al., 2006) has permitted to use more flexible techniques, like deconvolution, to estimate the impulse response of the system with as input a function retrieved directly from the data. Methods used to solve this problem are based on truncated Singular Value Decomposition (SVD) (Wu et al., 2003). However, these techniques suffer the impossibility to introduce any constraint on the stability of the system that describes the impulse response. The introduced oscillations render the estimated residue function, which is needed to extract perfusion, not physiologically interpretable. This fact is responsible of underestimation in perfusion estimates and of the introduction of negative values in the estimated function.

In Chapter 5 of this work a novel non parametric deconvolution technique is presented, based on Stable Spline (SS) kernel (Pillonetto and De Nicolao, 2010). It has been adapted to reduce the sensitivity on perfusion estimates due to the delay between input and output of the system. SS permits the introduction of constraints of non negativity and stability of

the system and can overcome the problems introduced by standard SVD based techniques. The novel approach will be tested in both simulation and real clinical data contexts. Moreover, it will be compared to already existing deconvolution techniques previously applied to QUASAR.

The same ASL sequence can be analyzed using a more restricted framework. A model to take into account the major peculiarities of this sequence was already presented by Chappell et al. (2013b). It uses a Bayesian estimator to extract numerous parameters related to perfusion and complementary for clinical evaluation, e.g. the arrival time of blood in the microvasculature. This pre-existent model has been improved in this thesis introducing a more complete relation between the sequence design and its effects on the acquisition. These modifications allow to estimate a new parameter, the mean blood velocity in the major arteries. A comparison of the novel model will be carried out also with SS to verify how the two approaches perform on the same dataset.

A number of other sequences have been proposed in literature to study perfusion with ASL. One of the most applied, because of its appealing properties of stability and elevated signal-to-noise ratio, is pseudo - continuous ASL (pCASL). In Chapter 6, a novel framework, based on a Maximum a Posteriori Bayesian estimator, has been built to take into account a-priori information from the literature and to include supplementary measurements into the estimation process. This new estimator will be applied both to Buxton model and in the same context also to a new two component model used to estimate both the macro and the micro vasculature components.

In the quantification process of ASL data it is necessary to fix some parameters to literature values. One of the most important is the labeling efficiency. Aslan et al. (2010) proposed a method to estimate it in-vivo using a measure of the velocity of blood in the brain feeding arteries. This approach needs a manual segmentation from a separate acquisition. In Chapter 7 a new totally automatic method for the estimation of labeling efficiency is presented, based on the use of a laminar flow model to estimate the velocity in a circular profile.

Neuroimmagini quantitative di perfusione con arterial spin labeling: deconvoluzione e modelli basati sulla fisiologia

SOMMARIO

Lo studio della perfusione con tecniche di Risonanza Magnetica per Immagini (dall'inglese Magnetic Resonance Imaging, MRI) è stato condotto prevalentemente con l'ausilio dell'iniezione di liquidi di contrasto esogeni. La tecnica Arterial Spin Labeling (ASL) permette di utilizzare l'acqua contenuta nel sangue come tracciante endogeno, riducendo quindi l'invasività dell'esame con aumento del comfort del paziente e diminuendo l'impatto del tracciante a livello di costo-beneficio per il sistema sanitario. Ne rende inoltre possibile l'utilizzo anche in casi in cui il contrasto non può essere utilizzato, come nel caso di bambini oppure per il monitoraggio ravvicinato dei livelli di perfusione. Inoltre, un altro vantaggio è la possibilità di quantificare la perfusione in unità assolute, permettendo così di confrontare più agevolmente soggetti in studi di gruppo oppure di poter confrontare più acquisizioni in un contesto di studio longitudinale.

La presente tesi si articola in una parte introduttiva che descrive i principi dell'ASL (Capitolo 1) e in generale della Risonanza magnetica (Capitolo 2). Per poter poi introdurre le tecniche utilizzate per la creazione del tracciante e le modalità di lettura dello stesso (Capitolo 3).

Il Capitolo 4 descrive lo stato dell'arte per la procedura di quantificazione, che avviene utilizzando opportuni modelli, utilizzati per descrivere accuratamente il metodo impiegato per la creazione del tracciante e

come esso interagisce con i tessuti che attraversa. Il modello più utilizzato è stato proposto da Buxton et al. (1998). Tuttavia il suddetto modello semplifica notevolmente la cinetica del tracciante, riducendo di fatto il fenomeno a un modello mono-compartimentale. Altri approcci sono stati utilizzati, che tengano conto della complessità del sistema capillare (Parkes and Tofts, 2002) o che tengano conto della componente macro vascolare dei vasi maggiori (Chappell et al., 2010). Gli stimatori utilizzati per la quantificazione con il modello di Buxton sono i minimi quadrati non lineari. Negli ultimi anni sono stati proposti anche approcci di tipo Bayesiano, ad esempio basati sul metodo delle variazioni (Chappell et al., 2009).

La creazione di opportune sequenze ASL come la Quantitative Star Labeling of Arterial Region (QUASAR) (Petersen et al., 2006) ha permesso di utilizzare anche tecniche più flessibili come la deconvoluzione, impiegata per stimare la risposta impulsiva del sistema sollecitata da un ingresso ricavato direttamente dai dati. Le tecniche utilizzate per la risoluzione di questo problema sono basate su Singular Value Decomposition con troncamento (Wu et al., 2003). Purtroppo, queste tecniche soffrono il fatto di non poter introdurre nessun vincolo di stabilità nel sistema che vanno a descrivere e quindi introducono delle oscillazioni non fisiologiche all'interno della funzione che permette di ricavare la stima della perfusione. Questo produce una sottostima nel livello di perfusione e anche valori negativi nella funzione stimata, che sono non interpretabili da un punto di vista fisiologico.

Nel Capitolo 5 di questo lavoro viene presentata una tecnica di decon-

voluzione non parametrica basata sul kernel Stable Spline (SS) (Pillonetto and De Nicolao, 2010) e adattata per risolvere il problema di sensitività al ritardo che può intercorrere tra ingresso e uscita del sistema. SS permette di introdurre vincoli di non negatività e di stabilità nel sistema descritto e può superare i problemi delle tecniche tradizionali. La nuova tecnica verrà testata sia in un ambito di simulazione il più prossimo possibile al caso reale, che in un insieme di soggetti reali sani. Verranno anche condotte delle analisi di confronto con altri metodi di deconvoluzione usati in letteratura.

La stessa sequenza può essere studiata con metodologie modellistiche. In particolare, recentemente è stato presentato un modello che con l'ausilio di uno stimatore Bayesiano può ricavare un notevole numero di parametri relativi alla perfusione (Chappell et al., 2013b), come il tempo di arrivo nella microvasculatura. Questo modello è stato migliorato in questa tesi introducendo una nuova relazione che permette di stimare un ulteriore parametro, la velocità media del sangue nei vasi. Verrà proposto un confronto tra i metodi con approccio basato sul modello e SS per verificarne le prestazioni.

Altre sequenze sono state proposte per stimare la perfusione con metodi non invasivi. Una delle più utilizzate prevede un labeling differente da QUASAR e che permette di ottenere un notevole aumento del rapporto segnale disturbo (SNR). Questa tecnica è chiamata pseudo-Continuous ASL (pCASL). Nel Capitolo 6 verrà presentato uno stimatore Bayesiano massimo a posteriori per tenere conto di ulteriori misure e di informazioni a priori note da letteratura. Lo stimatore verrà prima applicato al modello

di Buxton e successivamente, sempre in questo contesto verrà presentato e validato un modello a due componenti per la stima della componente macro-vascolare e micro-vascolare.

Nella procedura di quantificazione della tecnica ASL è necessario fissare alcuni parametri a valori noti da letteratura. Tra questi uno dei più importanti è rappresentato dall'efficienza di magnetizzazione. Aslan et al. (2010) hanno proposto un metodo per poterla stimare in vivo tramite una misura della velocità del sangue nei vasi dove avviene la creazione del contrasto endogeno. Tale approccio necessita della segmentazione manuale dei vasi in una immagine acquisita ad hoc. Nel Capitolo 7 viene presentato un nuovo metodo totalmente automatico per la stima dell'efficienza di magnetizzazione basato su metodi di segmentazione dei vasi e di stima della velocità attraverso l'uso di un modello laminare del flusso all'interno di un condotto.

Contents

Imagination is more important than knowledge...

Albert Einstein

1

Introduction to quantitative ASL

1.1 Basic principles of Arterial Spin Labeling

Arterial Spin Labeling (or Arterial Spin Tagging) is a completely noninvasive technique that provides a quantitative measure of perfusion (f). The general principle of ASL is to use protons of water molecules in the inflowing blood as an endogenous tracer to probe the blood supply to tissues. The tracer employed is constituted by a magnetic labeling of water molecules. This labeling is accomplished by manipulating blood water magnetization, which is inverted at the location of the larger brain-feeding arteries (such as the internal carotid arteries). The magnetization of those protons can serve as tracer for perfusion process since water transport across the blood brain barrier is relatively unrestricted, and water protons diffuse (although not as a freely diffusible tracer) from capillaries to tissue with their labeling, allowing perfusion to be measured.

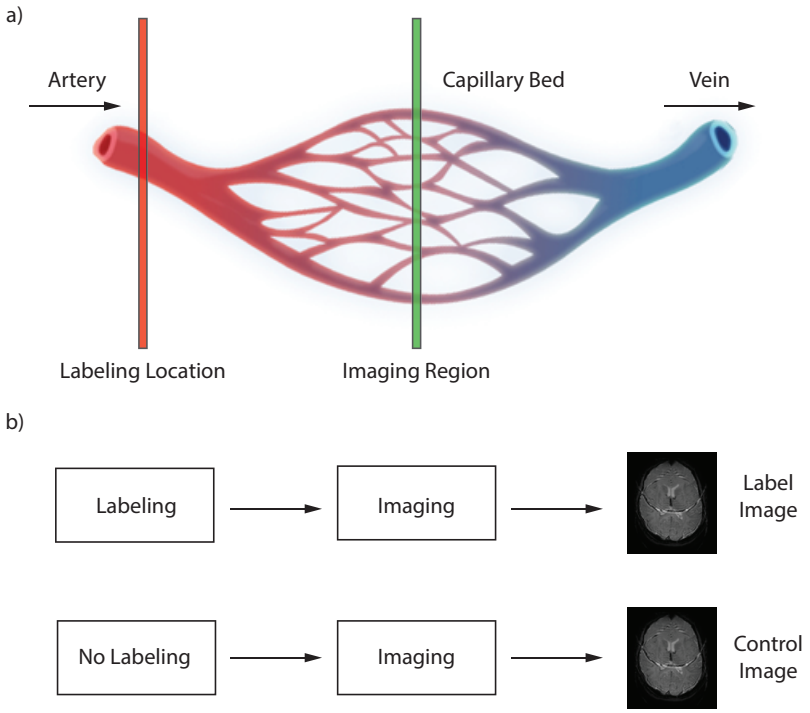

Figure 1.1.1: A schematic representation of the phenomenon that ASL measures is shown. Water in arterial blood is delivered to tissue capillary bed by arterial flow Here it is exchanged with tissue water and then drained by venous flow. This process is magnetically detected by labeling arterial water at a location proximal to the tissue to image, and isolated by a proper image subtraction. The ASL protocol, based on tag and control subtraction, is conceptually shown in panel b).

In a typical ASL experiment, a radiofrequency (RF) inversion pulse is applied to flip the magnetization of arterial blood water, before imaging region (a single slice or a volume) is reached. The water molecules, carrying the labeled magnetization, flow into each tissue element proportionally to the local perfusion. After a sufficient delay (typically denominated inversion time, TI) to allow the tagged blood to reach the region of interest, acquisition is performed, creating the so-called label (or tag) image. Then the experiment is repeated without labeling of the arterial blood to create the control image, in which no information about inflowing blood is observable. If the tag and control images are carefully adjusted, so that the signal from the static spins is the same in both images, then the difference of the two of them (control and label) gives rise to a signal (a magnetization difference signal ΔM) proportional to the amount of blood delivered to each voxel, nothing else than perfusion.

In each image (label and control) the voxel signal is proportional to the longitudinal magnetization of the voxel at image acquisition. If no arterial blood is delivered, the signal measured in tag and control images should be the same, and so the difference image would be zero. But if arterial blood is delivered to a voxel, it will carry an inverted magnetization in the tag image and a fully relaxed magnetization in the control image, and thus blood signal will not be canceled in the subtraction.

The major advantage of ASL comparing to other techniques used to measure perfusion resides in its complete non invasive nature. It uses magnetically labeled water as tracer instead of requiring injection into blood stream of exogenous contrast agents or inhalation of radioactive tracers (i.e. radioactive xenon studies). This confers to the technique a great versatility, making ASL applicable to human studies without any restriction regarding age (even pediatric population) or pathological conditions (patient with kidney failure cannot undergo typical bolus tracking perfusion studies) and also to measure perfusion in other tissues than brain. Moreover ASL opens the possibility of repeated perfusion measurements, that were not possible with older techniques based on the

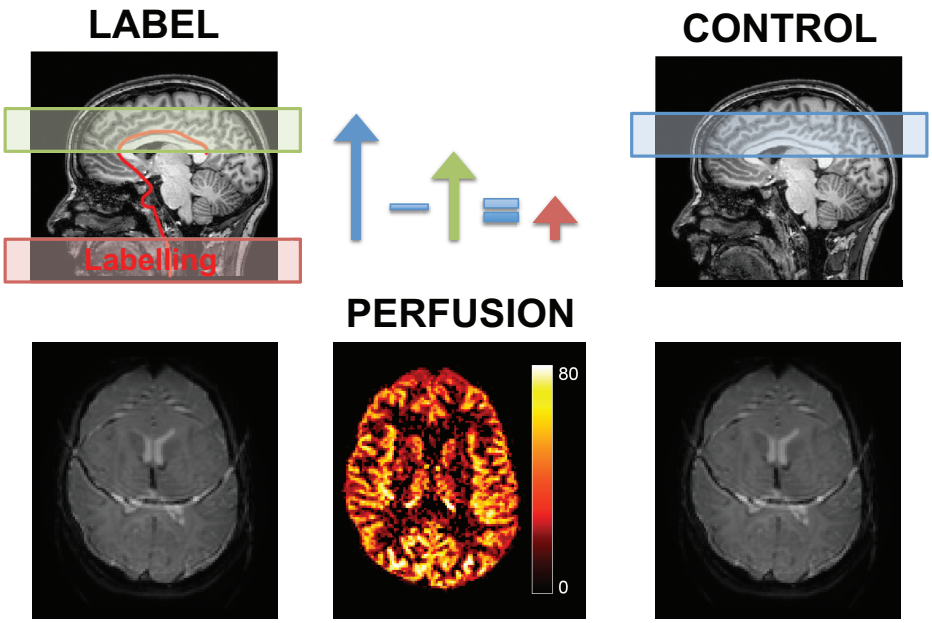

Figure 1.1.2: Basic principle of Arterial Spin Labeling: difference signal formation. The typical ASL experiment consists in the acquisition of the same image in two different conditions. One si called *label* and contains the contribution of both static tissue and blood. The contribution of the blood is obtained inverting water's spins of the blood in the feeding arteries of the brain. The second image called *control* is acquired with no blood contribution and contains only static tissue contribution. The different magnetic state, that has the blood that reaching the tissue gives rise to a coherent signal difference proportional to perfusion. Ideally, it works if the main assumption, that magnetization of tissue (often named static spins magnetization) remains the same in the two states of ASL experiment, is valid.

use of potential harmful and costly tracers, including the widespread Dynamic Susceptibility Contrast (DSC) MRI. These serial measurements could be useful in a number of applications, for example following perfusion changes after stroke or drug treatment, and for perfusion-based functional MRI (fMRI).

Furthermore, ASL technique traces a phenomenon directly related to perfusion. Especially, it provides a set of raw data, already showing a clear perfusion-weighting, from which a quantitative measure of perfusion, in absolute unit of $[{}^{\mathrm{mL}}/_{100\mathrm{g\,min}}]$, can be obtained.

Cerebral Blood Flow (CBF) represents the most common measure of the perfusion state of the brain. Adopting a general notation, it is given by:

$$P = \frac{F}{W} = CBF$$

where F is the blood flow rate in milliliters of blood per minute $[{}^{\mathrm{mL}}/_{\mathrm{min}}]$, W is the tissue mass in $[100\,\mathrm{g}]$, and P is the perfusion, called CBF in brain context.

Thus, CBF is the volume of arterial blood delivered to 100g of tissue per minute, with $[{}^{\mathrm{mL}}/_{100\mathrm{g\,min}}]$ as nominal unit. A typical value is $CBF = 60\frac{mL}{100g\,min}$ for gray matter, and $CBF = 20\frac{mL}{100g\,min}$ for white matter.

In imaging applications, it is convenient to express CBF as flow delivered to a unit volume of tissue rather than a unit mass of tissue. With these techniques, indeed, a signal is measured for a particular volume, the imaging voxel, and the actual mass of tissue within that volume is unknown, hence it easier define CBF in terms of a volume of tissue. Always using a general notation, we have:

$$f = \rho P = \rho\frac{F}{W}$$

where ρ is the tissue density in $[{}^{100\,\mathrm{g}}/_{\mathrm{mL}}]$, and f (called sometimes *perfusion rate*) is expressed in milliliters of blood per milliliter of tissue per minute (or second) $[{}^{\mathrm{mL}}/_{\mathrm{mL\,min}}]$ (or $[{}^{\mathrm{mL}}/_{\mathrm{mL\,s}}]$). This voxel-based definition of CBF is the natural choice for image-based perfusion measurements and has the

inverse time dimension as a rate constant. This dimensionality shows the primary role that CBF plays in determining the delivery of metabolic substrates and the clearance of metabolic products: the rate of delivery to the tissue of any substrate is simply fC_b, where C_b is the arterial blood concentration of the substrate Buxton (2005). To express f in common CBF definition terms, it must be scaled by the local density of the voxel, knowing that the density of brain is close to $1\frac{g}{mL}$:

$$\frac{mL}{mL\,s} = 1\frac{g}{mL}\frac{mL}{100g\,min} = 1\frac{g}{mL}\frac{mL}{100g\,60s} = \frac{1}{6000}\frac{mL}{mL\,s} \Longrightarrow f = \frac{1}{6000}CBF \tag{1.1}$$

where the correcting factor to move from $[\mathrm{mL}/_{100\mathrm{g\,min}}]$ to $[\mathrm{mL}/_{\mathrm{mL\,s}}]$ is made explicit. Accepting a density value of $1\frac{g}{mL}$ as a good approximation in brain tissue, a typical value for human is $f = 0.6\frac{mL}{mL\,min}$, or equivalently $f = 0.01\frac{mL}{mL\,s}$. In this thesis f refers to perfusion quantity, and is used to indicate also CBF, keeping in mind the difference in unit and the consequent conversion equation (1.1).

The big issue of ASL is intrinsically connected to the process that it aims to measure, and in the way it is intended to be measured. The signal change associated with the tagged blood is small. It can be roughly estimated by considering how much tagged arterial blood water can enter the brain during the experiment. If f denoted local perfusion in units of $[\mathrm{s}^{-1}]$, and the volume of voxel is V (in $[\mathrm{mL}]$), then the total rate of arterial flow into the voxel is fV (measured in $[\mathrm{mL}/_{\mathrm{s}}]$), and the volume of arterial blood delivered during TI is $fVTI$. Therefore the fraction of voxel volume that is replaced with the incoming arterial blood during the interval TI is $\frac{fVTI}{V} = fTI$. Since typical values for f and TI are respectively $0.01s^{-1}$ and $1s$, it results that the delivered volume of arterial water is only about 1-2% of the voxel volume (Buxton, 2002). Moreover, the magnetic label decays (with proper rate constant) in time, making the measurements feasible only in a limited temporal window. At 3T the decay of blood in healthy adult has been estimated to be $1.65s^{-1}$ (Lu et al., 2004), thus the remaining signal after only $3s$ of decay is only 16% of the

theoretically full magnetization achieved in the arterial side.

Due to the relative small magnitude of ASL signal, every other factor potentially liable to cause even a restrained signal variation must be avoided or compensated for. A common source of error is the magnetization transfer (MT) effect (figure 1.1.3), which can cause a signal loss substantially larger than the perfusion induced signal change, making fundamental an adequate equalization of these effects between tagged and control images.

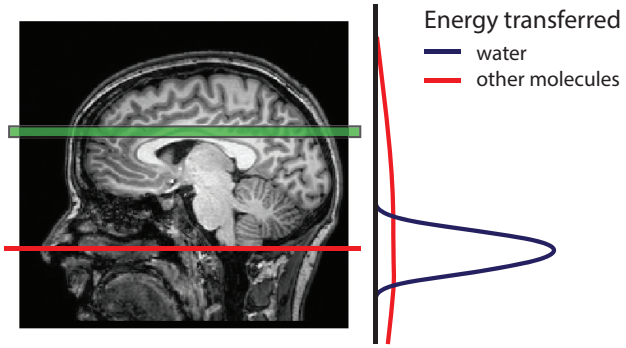

Figure 1.1.3: Water protons in blood have a narrow frequency spectrum (plotted in blue). Frequency spectrum of macromolecules in brain tissue is much broader (red). Thus labeling pulses affect macromolecular spins even when they are located at different positions, and this magnetization can be transferred to the free water signal. If the total power of RF pulses in label image differs from the one in control image, a net difference in magnetization is created, and subtraction errors are introduced in ASL images.

The small signal changes due to labeled blood make perfusion also very sensitive to random noise. As a consequence signal averaging to increase signal-to-noise ratio (SNR) becomes necessary (Fig. 1.1.4). Typically 20 to 40 pairs of subtracted control and label images are required in the averaging procedure to get the desired SNR in the perfusion weighted maps. This inevitably lengthens the acquisition time, to allow multiple experiment repetitions.

ASL technique is based on a quite simple idea, but in practice its execution requires to consider several sources of systematic errors. Dealing

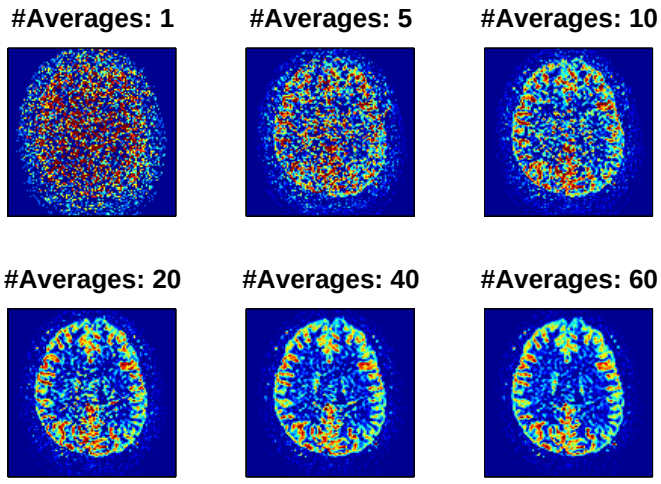

Figure 1.1.4: SNR improvement following a different number of averaged images is clearly shown in figure. To reach an adequate SNR level ASL experiment have to be repeated more times, lengthening the total scan duration.

with these technical difficulties is a critical aspect of ASL technique, because any uncontrolled confounding effect may contribute to loose the perfusion weighting of the small signal that is aimed to be measured.

1.2 ASL AS A BLOCK DESIGN EXPERIMENT

ASL implementation can be seen as a block design experiment. Indeed, each experiment contains in a unique pulse sequence the tracer generation, and the capability of effectively detecting it, despite the intrinsically small amplitude of its signal. The whole acquisition has to be implemented avoiding any contamination of the labeling step onto the following ones, and ensuring the right timing between them. Indeed, the magnetic label, progressively vanishes with time (the time scale is set by the longitudinal relaxation time of blood and tissues, see Tab. 1.2.1), but also needs a time delay before imaging to reach the tissue of interest.

As a consequence of these ASL principles, ASL is challenging to implement, and it requires advanced technical solutions to face a large set of

Table 1.2.1: T_1 relaxation of healthy brain tissues at 3T. T_1 of arterial and venous blood has been also reported. (Lu et al., 2004; Norris, 2003)

Tissue	$\mathbf{T_1}$ [ms]
White Matter	832
Grey Matter	1331
Cerebrospinal Fluid	4123
Arterial Blood	1700
Venous Blood	1650

potential degrading factors.

A generic ASL experiment can be thought as composed of three phases:

1. **labeling**: in which bolus of labeled blood to be deliver to the tissue is created by inverting magnetization of spins in protons water
2. **post-labeling**: in which a sequence of pulses is applied to improve SNR or to facilitate the subsequent data quantification step. It is an optional phase in a general ASL sequence
3. **readout**: in which the actual image (control or label) is acquired

There are a variety of methods both for spin preparation (labeling phase) and imaging acquisition (readout phase). One important feature of the ASL sequence is that the three components are almost independent from each others. This fact allows them to be combined as desired in relation to the specific application.

Perfect courage means doing unwitnessed what he would be capable of with the world looking on.

Francois de La Rochefoucauld

2

Nuclear Magnetic Resonance principles

In this chapter the principles of Nuclear Magnetic Resonance (NMR) are reviewed. All the following material has been adapted from an extensive introduction on NMR physics that can be found in Haacke et al. (1999). Magnetic Resonance Imaging (MRI) takes its name from NMR and its application to radiological imaging. MRI was born in the late forty's from the work of Block and Purcell, sharing the Nobel prize in 1952. The basic idea of MRI reflects the interaction of nuclear spin and magnetic field (B_0). The main proton used in MRI is the one of the hydrogen atom and its interaction with an external magnetic field results in a precession movement along the magnetic field direction. The precession motion can be described as angular frequency (ω_0) (See Haacke et al. (1999), chap. 2):

$$\omega_0 = \gamma B_0 \tag{2.1}$$

where γ is a constant called gyromagnetic ratio. The typical value for hydrogen γ (γ_H) is $2.68 \times 10^8 rad/s/Tesla$. This angular frequency of the precession motion is called *Larmor* frequency. Following this consideration, it is possible to describe the representative situation of a small volume of hydrogen proton spins immersed in a external magnetic field B_0. Comparing the field interaction with the thermal energy (that prevents the spins to fully align with the external magnetic field) and from the Botzmann's probability distribution of the spins precessing the external magnetic field, it is possible to describe only two energetic levels in which spins can be located, one parallel and one antiparallel to B_0. The difference between the number of spins in the two energy levels is only a very small portion of the total, i.e. for a magnetic field of 0.3 T is only one part per million. The net magnetization vector seen in a small volume of interest (*voxel*) can be described as $\mathbf{M} = (M_x, M_y, M_z)$. With the presence of only one external magnetic field the magnetization vector will have only a parallel component. When more magnetic fields are present, it will have also a traversal component. $\mathbf{M}$ can be decomposed in parallel and transverse magnetization following:

$$\begin{aligned} M_{\parallel} &= M_z \\ M_{\perp} &= M_x + i \cdot M_y \end{aligned} \tag{2.2}$$

The longitudinal equilibrium magnetization (M_0) is the component of the moment vector along the external field direction and can be computed as the proton magnetic moment component multiplied by the difference between the number of spins in the parallel and anti-parallel orientations:

$$M_0 = \frac{\rho_0 \gamma^2 \hbar^2}{4kT} B_0 \tag{2.3}$$

where ρ is the spin density, $\hbar$ is the Planck's constant, k is the Botzmann's constant, T is the temperature. This value, even if limited by the number of spins in surplus let to measure the NMR signal.

2.1 RADIO FREQUENCY PULSES

The net magnetization, in presence of an arbitrary time dependent magnetic field, $\mathbf{B}(t)$ neglecting relaxation effects, can be described as:

$$\frac{d\mathbf{M}}{dt} = \gamma \mathbf{M}(\mathbf{t}) \times \mathbf{B}(\mathbf{t}) \tag{2.4}$$

If the external magnetic field is constant $\mathbf{B}(t) = \mathbf{B_0}$ and parallel to the z axis, the transverse and parallel vector components of M from 2.4 can be separated into:

$$\begin{array}{ll} \frac{dM_x}{dt} & = \gamma \cdot B_0 \cdot M_y \\ \frac{dM_y}{dt} & = -\gamma \cdot B_0 \cdot M_x \\ \frac{dM_z}{dt} & = 0 \end{array} \tag{2.5}$$

This representation describes a transversal component $M_\perp$ precessing the z direction with angular frequency $\omega_0 = \gamma \cdot B_0$ and a constant longitudinal component $M_\parallel$. The magnetization can be manipulated directly by interaction with radio frequency pulses (RF pulses). If a particular RF pulse is considered, i.e. perpendicular to the z axis, induced by electromagnetic waves with angular frequency ω_{HF} and amplitude B_1 :

$$\mathbf{B}_1(t) = B_1 \cdot (cos(\omega_{HF} \cdot t), cos(\omega_{HF} \cdot t), 0) \tag{2.6}$$

When this RF field interacts with the static B_0 the resultant magnetization can be described using 2.4

$$\frac{d\mathbf{M}}{dt} = \gamma \mathbf{M}(\mathbf{t}) \times B_1 \cdot (cos(\omega_{HF} \cdot t), cos(\omega_{HF} \cdot t), B_0) \tag{2.7}$$

This relationship allows to manipulate the magnetization tailoring the RF pulse or adding more than one RF pulse. Correctly choosing the frequency and amplitude of the RF pulse, the magnetization can be redirected as perpendicular or antiparallel to B_0. A more general situation can be achieved by using the larmor frequency as the RF pulse frequency. It is possible to demonstrate that after a finite pulse length t_p, M is un-

aligned by a custom angle α, called *flip angle*:

$$\alpha = \gamma \cdot \int_0^{t_p} B_1(\tau) d\tau = \gamma \cdot B_1 \cdot t_p \tag{2.8}$$

For inversion preparation (antiparallel magnetization) is used $\alpha = 180°$ and for saturation (transverse magnetization) $\alpha = 90°$ is used. However several shapes of RF pulses exist and their principal properties are influenced by the spatial localization, the efficiency of the magnetization achieved and on the total energy transferred using them. The net magnetization of a single voxel can be read by using coils located around the probe since the magnetized voxel will emit radio frequent electromagnetic waves.

2.2 RELAXATION TIMES

In Eq. 2.4 relaxation effects are neglected. In real applications, however, there is a transitory effect after the RF pulse that can disturb the equilibrium magnetization of spins when only B_0 is imposed. This effect can be described by the Bloch equation, in the z direction:

$$\frac{dM_{\parallel}}{dt} = \frac{M_0 - M_{\parallel}}{T_1} + \gamma \cdot (\mathbf{M} \times \mathbf{B}) = \frac{M_0 - M_{\parallel}}{T_1} + \gamma \cdot (M_x B_y - MyBx) \tag{2.9}$$

where T_1 is the longitudinal relaxation and depends on probe material and magnetic field strength. The relaxation process is due to spin-lattice interaction and consists of exchange between spins and chemical bindings of the lattice that surrounds them. As explained in section 2 after a longitudinal magnetization is prepared a transverse component $M_{\perp}$ precesses B_0. This component can be also described by a transitory effect known as transverse relaxation. The transverse relaxation time is called T_2 and is associated to spin-spin interactions: this leads to a relative spins dephasing effect. From Eq. 2.2 the $B \perp$ component and the Bloch equa-

tion associated to it can be written as:

$$\frac{dM_{\perp}}{dt} = -i\gamma \cdot (M_{\perp}B_z - M_z B\perp) - \frac{M_{\perp}}{T_2} \tag{2.10}$$

Thus in an MRI observable experiment the system describing the magnetization phenomena will have a perpendicular and a parallel component. Each of them will have a characteristic time constant associated to them. It is useful to introduce also the concept of relaxation rates (i.e. the inverse of the relaxation time):

$$\begin{aligned} R_1 &= \tfrac{1}{T_1} \\ R_2 &= \tfrac{1}{T_2} \end{aligned} \tag{2.11}$$

2.2.1 Inversion Recovery experiment and T_1

If the RF pulse B_1 is tailored to obtain an antiparallel net magnetization, the relaxation phenomenon after it, is called Inversion Recovery (IR). The main application of IR is to measure T_1. In absence of the transversal component only Eq. 2.9 should be considered in the calculations. The solution for this type of RF can be written as:

$$M_{\parallel} = M_0 \cdot \left(1 - 2 \cdot e^{-\frac{t}{T_1}}\right) \tag{2.12}$$

To estimate T_1 multiple acquisitions at different t should be used. However it is very popular to acquire a single image at a single t value, this is called the Inversion Time (TI). Considering the decay, it is easy to understand that changing this time will lead to different contrasts (Fig. 2.2.1). Moreover, if TI is chosen appropriately (e.g. $TI = TI_0$) it is possible to null the signal of a specific tissue. The signal acquisition can be achieved using another RF pulse of 90° flipping the magnetization of the transverse axis.

2.2.2 Free Induction Decay and T_2

A Free Induction Decay (FID) experiment can be described when a $90°$ RF pulse is applied in the presence of only B_0. After the pulse, the longitudinal magnetization will be zero and the transversal one will be equal to M_0. From this experiment it is possible to estimate the transversal relaxation time T_2. Indeed, the solution of Bloch Equation (Eq. 2.9) can be written as:

$$M_\perp = M_0 \cdot e^{-\frac{t}{T_2} - i\gamma B_0 t} \tag{2.13}$$

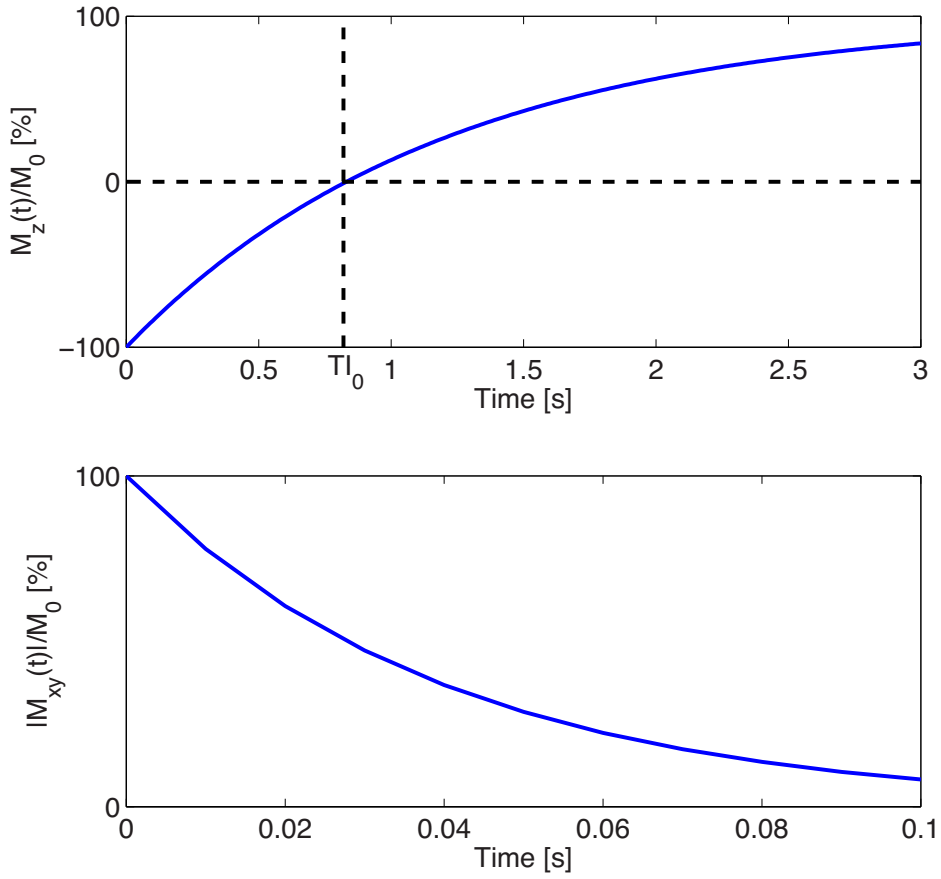

Figure 2.2.1: In the top row T_1 relaxation during an Inversion recovery experiment (T_1 simulated of 1.2s) while in the bottom row T_2 relaxation during a Free Induction Decay experiment (T_2 of 100ms).

The resulting complex magnetization has two parts: a magnitude one describing an exponential decay and an imaginary one describing an oscillatory phenomenon of the phase. This curve should be sampled at different values to estimate T_2, as for the IR experiment. In the same way as TI for T_1, the chosen time for the readout in FID experiment is called echo time (TE). The spin-spin interactions (Eq. 2.10) describe a relative dephasing of near spins. If only the magnitude component of $M_\perp$ is considered:

$$||M_\perp(t)|| = ||M_\perp(t)|| \cdot e^{-\frac{t}{T_2}} \tag{2.14}$$

However, local B_0 inhomogeneities (ΔB_0) amplify this effect. Neighboring spins will experience slightly different magnetic fields leading to relative phase differences over time. This degrading can be expressed by an extra relation due to local mean field inhomogeneities:

$$T_2' = \frac{1}{\gamma \cdot \Delta B_0} \tag{2.15}$$

This leads to a perceived faster decay of spins, governed by a new relaxation time, called T_2^*:

$$\frac{1}{T_2^*} = \frac{1}{T_2} + \frac{1}{T_2'} \tag{2.16}$$

2.2.3 Spin Echo

T_2^* relaxation seems to rule every experiment in MRI where transverse magnetization is investigated. Using an empirical approach, Hahn (1950) discovered the so called Spin Echo. This particular echo can be used to prepare pure T_2 images without any dephasing resulting in T_2^* weighting. This sequence is made up of four steps. Firstly a $90°$ RF pulse is applied to start a FID experiment; secondly a short time is inserted as delay; thirdly a $180°$ RF pulse is applied and finally, after another delay time, the readout can start. The reason why this image is a true T_2 weighted comes from field inhomogeneities that result in different larmor frequencies for

spins disturbed by slightly different external fields. The results of this are that there will be both faster and slower spins in the neighborhood that precess the external field. After a 180° pulse the spins behind will be flipped along the transverse axis, passing the faster ones, but keeping precessing in the same direction with the same dephasing because the inhomogeneities have not changed. During the second delay time the faster spins are now behind the others but since they are faster, after the same time all the spins will be again phased together. The spin-spin interaction is not recoverable with this process and the magnetization seen is only due to T_2. The sum of the two delays is again the Echo time (TE).

If there is anything in the world that can really be called a man's property, it is surely that which is the result of his mental activity.

Arthur Schopenhauer

3 ASL Sequences

This chapter describes the three fundamental blocks of a typical ASL experiment. Since many configurations and implementations of ASL has been proposed, this overview will cover the most used methods according to literature and the sequences used in the modeling task. The chapter is divided into three sections, one for each of the three blocks.

3.1 Labeling

The first block needed in an ASL experiment is called *labeling*. Several types of labeling techniques have been presented in the last decades with the aim of inverting spins in arterial blood water. Two are the main approaches: Continuous ASL (**CASL**) (Detre et al., 1992; Williams et al., 1992) and Pulsed ASL (**PASL**). In CASL arterial blood spins are inverted in the meanwhile when pass through a plane fixed to a design location. The typical inversion technique employed with CASL is a flow driven

adiabatic inversion RF pulse and its duration is about $2-4$ s. Instead, in PASL, a spatially defined labeling inversion pulse is applied to a larger region. This technique avails of the use of adiabatic inversion, because of its robustness to B_1 inhomogeneity and as a result a large portion of water spins is inverted simultaneously. The duration of a typical PASL inversion pulse is about $10-50$ ms. The main advantage of CASL respect to PASL is its higher signal to noise ratio and the possibility to set the end of the bolus duration. Vice versa the main advantage of PASL compared to CASL is its reduced specific absorption rate (SAR) due to the short RF-pulses employed and a higher labeling efficiency (i.e. the fraction of equilibrium magnetization that is actually inverted by labeling scheme, denoted by the dimensionless number α). Moreover CASL suffers MT effects more than PASL. Hence, an hybrid approach that improves CASL has been presented. This technique is called Pseudo Continuous ASL (pCASL (Dai et al., 2008)). This technique simulates a CASL protocol by using a train of RF pulses and a gradient waveform adequately shaped in order to overcome the limitations connected to practical realization of the typical CASL scheme. The use of a train of RF pulses is more compatible to the hardware used in modern scanner. Since its presentation, pCASL has been considered to be the best approach for labeling water of blood in ASL studies.

3.1.1 PULSED ASL

Pulsed labeling consists of a RF inversion pulse applied to produce a bolus of labeled magnetization in a defined location. The spins of the water protons in the blood are the target. The blood acts as a endogenous tracer and permits the estimation of perfusion. The created bolus can travel through the arteries down to the arterioles and reaches the capillary bed, exchanges the labeled magnetization with the unlabeled magnetization of the tissue water. Pulsed ASL techniques shares the same basic principles, but differs in strategy used to acquire control and label images. The inversion is usually performed using a hyperbolic secant adiabatic inver-

sion pulse. The characteristic of adiabatic pulses is to not be dependent on how B_1 varies across the magnetization field, i.e. the typical relationship between flip angle and B_1 is no longer valid for adiabatic pulses:

$$\theta = \gamma \int_0^T B_1(t)dt \tag{3.1}$$

where $B_1(t)$ is the RF modulation, which is 0 before $t = 0$. The integration in performed over the duration of the RF pulse. In PASL the inversion should be as uniform as possible in the labeling region. This is the reason why the use of adiabatic pulses is preferable. Indeed using an opportune modulation shape of the RF pulse, is possible to uniformly invert the magnetization of large areas even if B_1 field is not homogeneous. Like all adiabatic pulses, adiabatic inversion pulses do not obey to Eq. 3.1. Instead, the flip angle θ of an adiabatic pulse depends on how the B_1 field varies its amplitude and modulation during the pulse.

3.1.1.1 Signal Targeting with Alternating Radiofrequency (STAR)

Signal Targeting with Alternating Radiofrequency (STAR) (Edelman et al., 1994) labeling scheme is shown in Fig. 3.1.1. As usual the sequence alternates acquire both label (Fig. 3.1.1a) and control (Fig. 3.1.1b). Afterwards the difference between the two images is performed offline on a separate workstation to obtain a perfusion weighted image. The labeling sequence starts with a slice selective $90°$ pulse located in the imaging region (green band in Fig. 3.1.1c). This pulse saturates the imaging region protecting it from any perturbation caused by the following inversion. The spatially inversion pulse inverts the spins contained in a very thick slab (10 -15 cm in yellow band in Fig. 3.1.1c) positioned near to the imaging site. Usually a gap of 1 cm between labeling and imaging region is needed to avoid indesiderate effects due to non ideal profile of the labeling pulse. The net magnetization produced by the inversion pulse has to reach the imaging region before the acquisition is performed. The timing between this phase and the acquisition is fundamental to avoid errors in perfusion

quantification and it is discussed in Section 3.4. The control image could be theoretically acquired simply repeating the labeling sequence without the inversion pulse as presented in the original STAR implementation. However, the tagging pulse is off-resonance respect to the imaging region and could result in MT effects as discussed previously in Section 1.1. If the same inversion pulses are applied with the same modulation function but with an opposite carrier frequency respect to the imaging slice (blue band in Fig. 3.1.1d) it can produce an identical MT effect also on the control image. As long as the MT effects are symmetric when the difference is performed the MT effect will be cancelled out. This technique can be applied only to single slice acquisitions.

To permit a multi slice acquisition a new version of STAR has been proposed (Edelman and Chen, 1998). In this new version, according to the scheme described in Fig. 3.1.1e the RF power of the labeling inversion pulse is counterbalanced by the two consecutive adiabatic pulses of half RF power. The induced magnetization transfer effects are identical in both cases, and these allow multi-slice acquisition with good MT effects equalization (Edelman and Chen, 1998). Anyhow, MT effects are less prominent in PASL techniques, and care must be taken to reduce the effects of non the ideal profile of the tagging pulse on the imaging region, making necessary the introduction ofa sufficient spatial gap from labeling to imaging region. Having tagged the arterial blood that flows into imaging region with an inverted magnetization, in STAR experiments, the signal from a voxel in label image, M_l, is less than the one in control image, M_c, (if a consistent amount of blood perfuses it). Therefore to obtain a positive subtraction image, the difference signal ΔM has to be defined as:

$$\Delta M = M_c - M_l \tag{3.2}$$

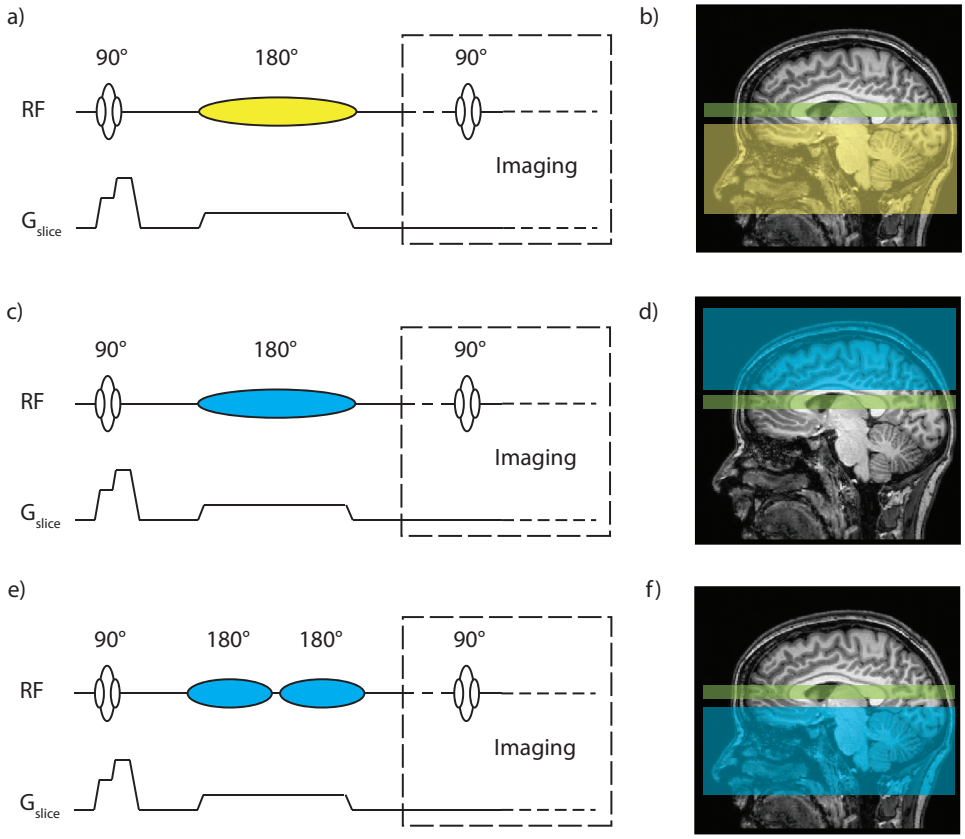

Figure 3.1.1: STAR labeling scheme adapted from (Bernstein et al., 2004). Panel a) shows the pulse sequence for the label step. A 90° saturation pulse is applied before the inversion in the proximal yellow band respect to the imaging region (been slab). This scheme was introduced for single slice but can be adapted to multi slice acquisitions. Panel b) shows the original version of STAR for the control sequence. The pulse sequence is different in the location where the inversion pulse is applied, to avoid MT effects. To allow the cancellation of MT effects the carrier frequency of the two pulses is inverted respect to the frequency of the pulse applied to select the slice and results in an inversion region distal to the imaging region (blue band in panel d)) (Edelman et al., 1994). This version can be applied only to single slice acquisition. In the last two panels e) and f) the last presented version of STAR scheme that permits multi slice acquisition (Edelman and Chen, 1998) is reported. The inversion pulse is applied twice but with half power to produce no inversion in the control image but apply the same MT effect. MT effect will be canceled in the subtraction operation and hence it is not present in the final perfusion weighted image.

3.1.1.2 VARIATIONS OF STAR TECHNIQUE

Proximal inversion with a control for off-resonance effects (PICORE) (Fig. 3.1.2) is a variation of the STAR labeling scheme (Wong et al., 1997). The labeling acquisition is equivalent as in STAR but an off-resonance inversion pulse in the control acquisition is employed without the coupling with a slab selective gradient. In this way the carrier frequency of the inversion pulse is the same as the labeling sequence and it can be canceled out. This strategy can compensate for asymmetric MT effects and is not sensitive to the flow from the distal side of the imaging region. However, PICORE is more sensitive to eddy currents respect to STAR since the waveform of the pulses in the two acquisitions is different.

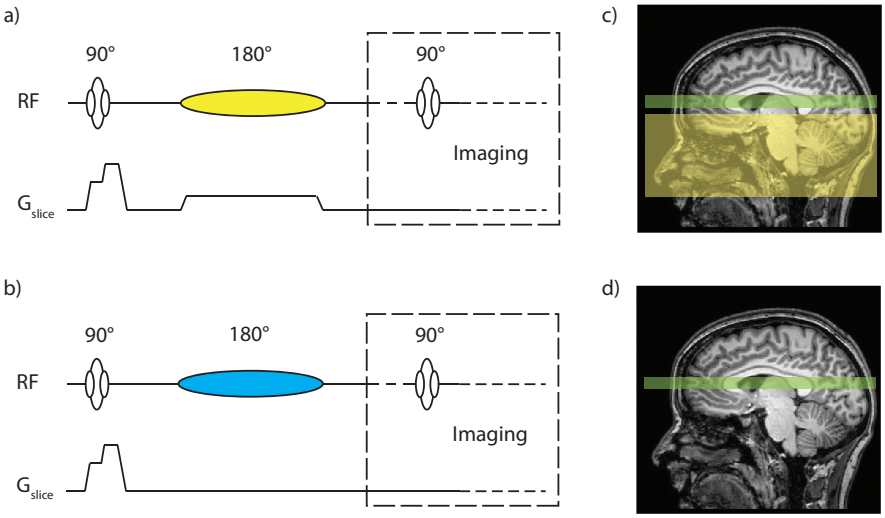

Figure 3.1.2: Proximal inversion with a control for off-resonance effects (PICORE) labeling scheme adapted from (Bernstein et al., 2004). PICORE is an alternative to STAR. Panel a) shows the label sequence, identical to STAR (Fig. 3.1.1a). For the control image the inversion pulse is applied without the coupling of a slice selection gradient. In this way the control image do not experience any inversion but the MT effects are identical and therefore can be canceled in the subtraction.

Another variation of STAR has been proposed and it is known as Transfer Insensitive labeling technique (TILT) (Golay et al., 1999). In this implementation the initial inversion is replaced by two $90°$ pulses. To produce a net magnetization of $180°$ the two pulses should have the same phase.

On the contrary, in the control acquisition the second pulse is opposite in phase and no net magnetization is produced. This produces the same MT effects on both control and label allowing thus their cancellation.

3.1.1.3 Flow-Insensitive alternating inversion recovery

The labeling scheme proposed by Kim (1995); Kwong et al. (1995), called Flow-Insensitive alternating inversion recover y(FAIR), uses a frequency selective inversion pulse coupled or not with a gradient for slice selection to produce respectively labeled and control images. Similar to STAR the inversion is achieved using an adiabatic inversion pulse. Differently from STAR the frequency carrier of FAIR is the same for both label and control. When a slice gradient is applied it inverts the magnetization only in the selected portion (green slab in Fig. 3.1.3a) leaving unaffected the rest of the field. When the inversion pulse is applied alone it has a non selective behavior and it will affect indistinctly the whole field inverting its magnetization (blue slab in Fig. 3.1.3a). By using the same waveform for both the conditions, this scheme allows to better compensate for eddy currents effects. Since both blood and tissue experience the same T_1 recovery there is a very low sensitivity to inflow of arterial blood in the control image (Nishimura et al., 1987). Since the label has no net magnetization component from the blood, it has a higher magnetization than the control that instead experienced the inversion of the blood. To maintain the positive sign of the labeled magnetization, the difference signal ΔM has to be defined as:

$$\Delta M = M_l - M_c \tag{3.3}$$

FAIR is more robust to MT effects respect to STAR and moreover the contribution to perfusion signal is made of arterial blood feeding the region from both proximal and distal areas respect to the imaging slice. If the feeding artery in the region is unknown or is not in the distal region because of pathologies, FAIR might be less sensitive to perfusion under-

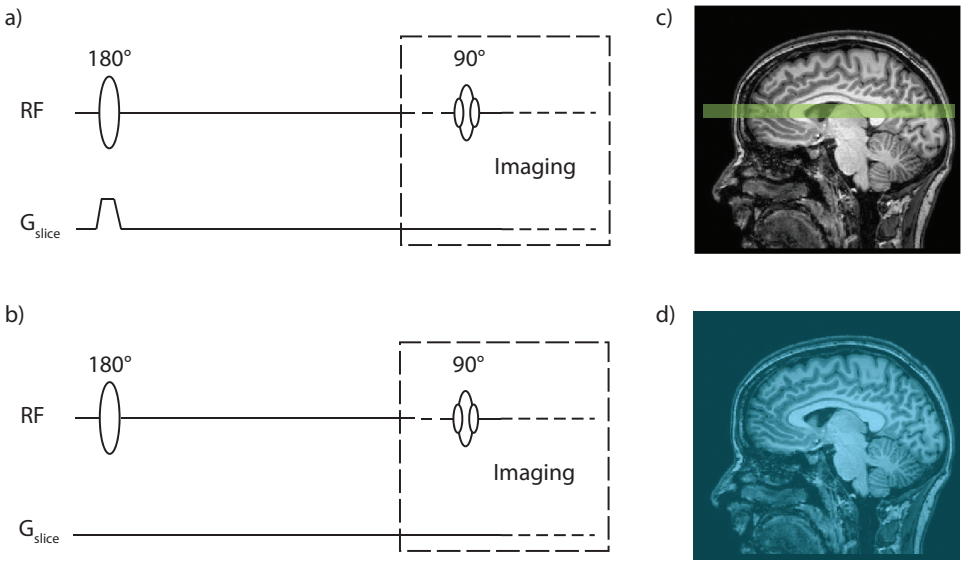

Figure 3.1.3: Flow-Insensitive alternating inversion recovery (FAIR) labeling scheme adapted from (Bernstein et al., 2004). FAIR sequence do not employ any saturation pulse before inversion. The label sequence (Panel a)) consists of a combined slice selection gradient and an inversion pulse. The control image is obtained applying the same inversion pulse to allow MT effects to be canceled but without the use of any slice gradient selection. The latter permits the inversion of the magnetization in the blue band. Thus the net magnetization obtained is negative in sign. To retrieve a positive sign for the perfusion weighted image the subtraction should be done following Eq. 3.3 .

estimation.

Two FAIR variants have been proposed: one of them is the uninverted flow-insensitive alternating inversion recovery (UNFAIR) (Helpern et al., 1997), where the number of inversion pulses in both control and label image are doubled maintaining the same scheme of coupled slice gradient selection and inversion for label and control. This introduces a $360°$ pulse that allows to obtain a net positive magnetization as for STAR (Eq. 3.2). Another pulse sequence based on FAIR is flow-insensitive alternating inversion recovery with an extra radio frequency pulse (FAIRER) (Mai et al., 1999). The key modification to FAIR is the addition of a slice selective saturation pulse immediately before the inversion of the FAIR sequence. This allows to reduce the sensitivity of FAIRER to the TI chosen when it corresponds to a nulling time for specific tissues.

3.1.2 Continuous ASL

Continuous ASL was developed historically before PASL. The first method employed multiple saturation pulses (Detre et al., 1992) and was then replaced by inversion pulses (Williams et al., 1992). Contrary to PASL the principle used for the inversion is the flow-driven adiabatic inversion (Dixon et al., 1986). Taking an arbitrary RF pulse, it cannot be an adiabatic pulse for static spin. For moving spin, this is not completely true and indue, applying a field gradient G in the motion direction concurrent to the RF pulse it can produce an adiabatic inversion. The motion of spins along the gradient changes the frequency of the spins from over resonance under the resonant frequency of the applied RF pulse. Setting a reference frame as the blood water spin, when they are far from the labeling plane they are off resonance. As the blood flows through the plane the conditions of the spins switch to on resonance. Leaving the labeling plane the spins start to became off resonance again. The frequency of the spins sweeps during this process and becomes inverted. The result of the application of this pulse to a moving flow of spin is a flow driven adiabatic inversion. Hence, it is possible to drive the magnetization from parallel

to B_0 to anti-parallel respect to a specific location. In case of CASL, the location is a plane positioned orthogonally to the carotid and vertebral arteries in the neck. In the rotating frame set as reference, the effective field B_{eff} can be described as the vector sum of the fields of the applied RF pulse (B_1) and an additional field proportional to $\Delta\omega/\gamma$ where $\Delta\omega$ is the frequency offset between the resonant frequency of the spins and that of the labeling pulse. Spins that move towards the plane will have an inverted magnetization. This is true only when the adiabatic condition is satisfied. Under this assumption the magnetization of the moving spins is inverted irrespective to their velocity:

$$\frac{1}{T_{2b}}, \frac{1}{T_{1b}} \ll \frac{Gv}{|B_{eff}|} \ll \frac{\gamma}{2\pi}|B_{eff}| \tag{3.4}$$

where T_{2b} is the T_2 relaxation of the blood, v is the velocity of the water molecules of the blood and B_{eff} is the effective component of the induced magnetic field lying in the flow direction and G is the gradient field applied along this direction. If the velocity of the blood is too fast, the adiabatic condition is not satisfied and the relationship is no longer valid. On the contrary, if the flow velocity is lower, then the T_2 effect dominate the relation (left side of the equation) rendering the inversion not efficient. It is worth noting that the right side condition in Eq. 3.4 on T_2 is more restrictive than on T_1 since usually T_2 is always shorter than T_1. CASL approaches need, as well as PASL, the acquisition of at least two conditions. Hence, CASL labeling sequence starts with a inversion couple with a gradient parallel to the flow direction, usually the z axis.

3.1.3 Pseudo Continuous ASL

Theoretically, the continuous labeling produces a greater SNR than pulsed labeling. Nevertheless, this theoretical advantage is reduced by a number of challenges that practical implementation of CASL have to face. Among these, are inefficiency of labeling, magnetization transfer effects and limited support for continuous-mode operation on clinical scanners. The last one is surely the most difficult to bypass: the majority of the imagers

are optimized for pulsed operations and cannot support CASL because of constraints on the RF duty cycle. It means that flow-driven adiabatic inversion cannot be achieved applying constant RF and gradient fields. Intuitively, the solution could be found by breaking up the continuous rectangular RF into a train of RF pulses separated by a gap. This is exactly the basic idea of pCASL (Dai et al., 2008). The approximation of the continuous RF pulse (Fig 3.1.4a) can be made by a train of rect functions as in Fig 3.1.4b. This solution has the drawback to produce aliased labeling planes. This can be demonstrated taking the rect representation of the RF pulses with Δt as the spacing between two consecutive pulses with width δ and convolving it with a train of Dirac delta functions:

$$RF_b = \frac{1}{\Delta t} train\left(\frac{t}{\Delta t}\right) \otimes rect\left(\frac{t}{\delta}\right) \tag{3.5}$$

where $train(t) = \sum_{n=-\infty}^{+\infty} \delta(t-n)$. The Fourier transform of RF_b is:

$$\mathcal{F}\{RF_b\} = train(f\delta t) \cdot \delta sinc(\pi \delta f) \tag{3.6}$$

Eq. 3.6 reveals the presence of multiple planes at frequency $f = \Delta t/n$ modulated by a sinc function. If a gradient G in the z direction is applied, the planes are located at $z = n/(\gamma G \Delta t)$ in the space domain. Using a *Hanning* function instead of a rect it is possible to reduce the number of aliased planes because its Fourier transform drops faster than the $sinc$ function (Fig. 3.1.4c). However, the aliased planes are still present and a strategy to suppress them could be to apply strong slice selective gradient during each Hanning pulse. The amplitude of such gradient, G_{max} should be balanced respect to the average gradient amplitude in each cycle (G_{ave}). This means that there still will be aliased planes at $z = n/(\gamma G_{ave} \Delta t)$. Opportunely tuning the Hanning response can lead to a narrower pulse in which the first zero will be at $z = 1/(\gamma G_{max} \Delta)$. Thus respecting the following condition permits to overcome the problem of

aliased planes:

$$\frac{G_{max}}{G_ave} \gg \frac{\Delta t}{\delta} \tag{3.7}$$

Under this condition it is possible to use flow-driven adiabatic inversion with such RF shape. Moreover, to match CASL requirements, the labeling sequence should be able to cause a position-dependent phase shift. This can be achieved introducing an imbalance in the gradients (Fig. 3.1.4d) but maintaining an average value G_{ave} between pulses comparable to that used for continuous inversion. For the control, a $180°$ phase shift for all positions has to be introduced. This can be seen in Fig. 3.1.4e where G_{ave} between pulses is zero. In this case, the average B_{eff} of RF pulses is zero (no magnetization inversion is achieved) but its power is equal to the label sequence and thus the MT effects are canceled out in the subtraction between the two conditions.

3.1.4 Last developments

In the last years a new labeling scheme has been proposed. A problematic issue with the classical CASL/PASL/pCASL approach is the sensitivity to the Bolus Arrival Time (BAT). This aspect will be covered in section 3.2 and in chapter 4. BAT sensitivity can affect the quantification of perfusion and hence it has been severely taken into account developing new BAT insensitive sequences. This is the case of Velocity selective ASL (VSASL) (Wong et al., 2006). VSASL is a variant of pulsed ASL that eliminates the bolus arrival time sensitivity by labeling the blood much closer to the capillary bed. VSASL consists of an additional module that uses non-selective RF pulses and magnetic field gradients to modulate the longitudinal magnetization of the spins as a function of their velocity. The key point is that speed will collapse down from artery level to tissue level and VSASL saturates spins above a certain cut-off velocity (V_c), which are then imaged after they have merged with tissue water molecules. If V_c is optimized for a value corresponding to the blood velocity at the

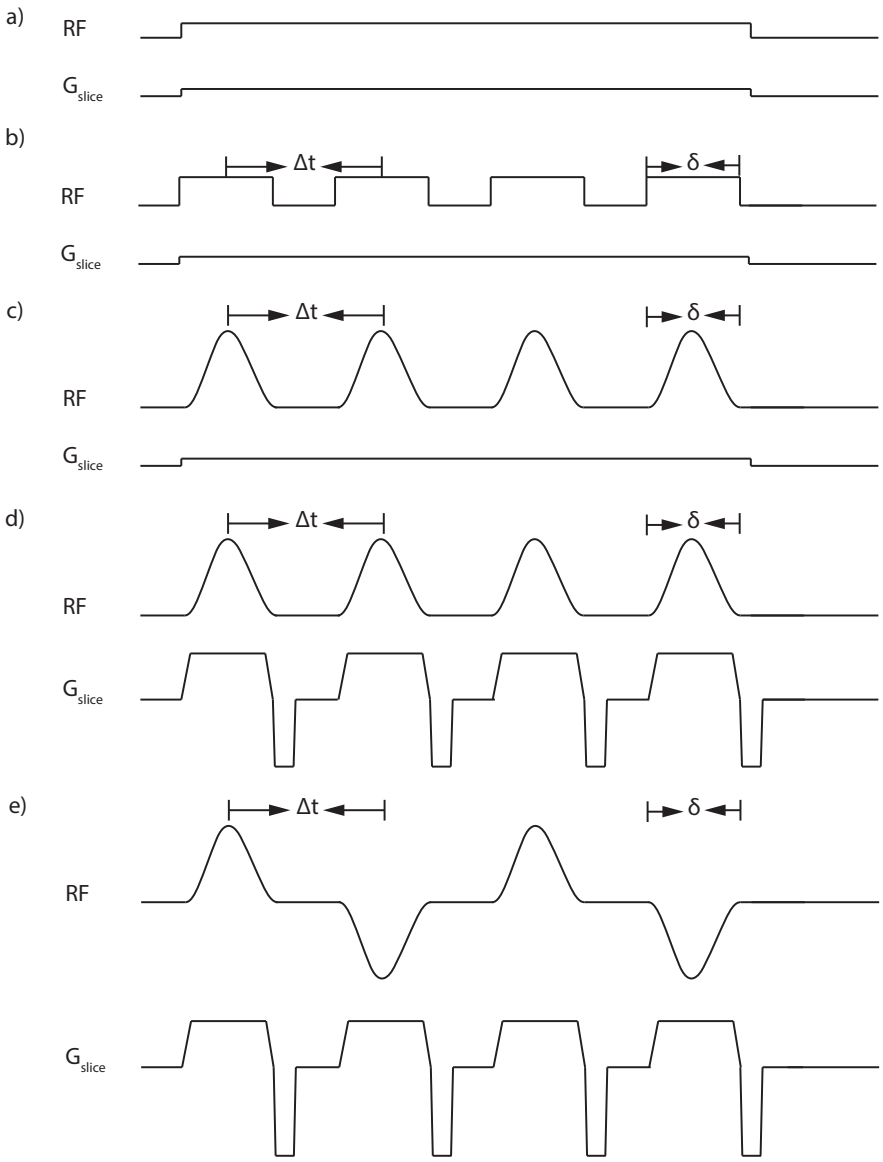

Figure 3.1.4: Labeling scheme for Continuous and pseudo Continuous ASL. Adapted from (Dai et al., 2008). In panel a) the theoretically continuous RF pulse of CASL is shown. It can be virtually substituted by a train of shorter RF pulses. In panel b) an example using a rect function is shown. This approach is susceptible to aliasing of inversion planes. Using a Hanning shape RF pulse and a slice selection gradient (panel c) is possible to exclude the aliased planes narrowing the window of effectiveness of inversion pulses. The last panel (e) shows a control sequence for pCASL that includes an imbalance in gradient and a phase shift of 180° in the RF to not achieve any magnetization effect but still produce the same MT effect.

capillary level, the label process is made within the voxel of interest and hence it is insensible to BAT (Wu and Wong, 2006). The main appealing application of this technique is in presence of very slow flow, such as in pathologies like stroke or stenosis, since it is capable to provide semi-quantitative map of perfusion where the conventional methods are not (Wong et al., 2006). However several artifacts related to Cerebro Spinal Fluid (CSF) have been documented and RF imperfection leads to systematic subtraction errors. Furthermore, B_1 and B_0 inhomogeneities lead to an underestimation of perfusion due to spatial variations in tagging efficiency (Duhamel et al., 2003). Additionally, the VSASL sequence is not eddy current balanced and recently an additional preparation module has been introduced to improve this aspect (Meakin and Jezzard, 2013). However, from the clinical point of view, this technique should be considered as a work in progress tool.

Another pitfall not yet listed for VSASL is the fact that both arterial and venous blood are tagged indistinctly. A new approach named Acceleration-Selective ASL (AccASL) has been recently proposed (Schmid et al., 2014) to solve this issue. The main difference between this two approaches is that AccASL is able to distinguish between accelerating and decelerating spins. If an acceleration cut-off A_c is set appropriately it is possible to saturate spins that are accelerating, i.e. keeping inverted only spins that are arriving in the tissue from the arterial side.

pCASL and CASL approaches suffer because RF coils are used also in the labeling process and therefore in the meanwhile the read out cannot be performed. In this way, the initial portion of the signal cannot be acquired. Recently a new encoding scheme that can potentially overcome this problem has been presented (Dai et al., 2012; Wells et al., 2010a). Moreover a refined timing in the encoding of pCASL labeling has been presented, called Time Encoded ASL (Teeuwisse et al., 2014). The key idea is that with opportune different encoding schemes repeated over time and a series of additions and differences operations is possible to retrieve the full kinetic curve of the blood also during the labeling. All these approaches are very promising and will be further validated and tuned

also in clinical environment. At present, the most used labeling scheme for pCASL in clinical studies is the simple approximation of CASL prolonged labeling.

3.1.5 Labeling efficiency

In general terms, labeling efficiency can be defined as the fraction of initial blood longitudinal magnetization inverted by the tagging scheme. It is usually denoted as α:

$$\alpha = \frac{M_0 - M_0^L}{2M_0} \tag{3.8}$$

For a PASL sequence it means that all the water spins in the labeling region could be potentially inverted. For CASL and pCASL, α is calculated as the fraction of the spins of water molecules in blood correctly inverted over the whole number of spins that passed towards the labeling plane during the inversion pulse. Labeling efficiency is a critical factor in every ASL implementation. It affects the quality of acquired ASL images since it directly controls the SNR of the measured data. Roughly, the SNR of ASL experiment depends on the amount of inverted magnetization carried into a unit volume during the examination time. Hence, the amount of blood delivered to local tissue by flow and the quality of the inversion step are the main factors determining the SNR. Thus, when designing a tagging scheme, great attention should be paid to avoid any reduction in theoretical labeling efficiency, since ASL is already a low SNR technique.

In PASL, labeling efficiency is not a big issue and it has been demonstrated to reach value over 90% (Petersen et al., 2006). Since in CASL and pCASL it is function of several factors, such as velocity of flow, gradient amplitudes and coupling of RF train characteristic parameters, it should be carefully evaluated. In Maccotta et al. (1997) an exhaustive simulation was carried out over a wide range of parameters to estimate α for CASL. With an appropriate selection of RF amplitude and gradient strength, the inversion efficiency was found to be 0.9, a value substantially stable in a wide range of velocities ($10 - 60\ cm/s$). Labeling efficiency of pCASL

tagging scheme has been investigated using numerical simulations and the theoretical labeling efficiency value has been set around 0.85 (Dai et al., 2008). However, the implementation of pCASL tagging scheme is more technical demanding and its efficiency is more sensitive to different sources of variation respect to the simple flow-driven adiabatic inversion used in CASL. Indeed, to achieve optimal inversion of blood magnetization, another condition has to be precisely met: the phase of consecutive RF pulses has to match the phase accrual of flowing spins between pulses. Whenever a mismatch in phase concordance $(\Delta\phi)$ arises, the inversion efficiency of pCASL tagging scheme degrades (Wu et al., 2011). The phase error $(\Delta\phi)$ is mainly due to off-resonance fields at the tagging plane, and to imperfections in the applied gradient. Unfortunately, the amplitude of these effects depends on several factors, such as B_0 and B_1 field inhomogeneities and scanner hardware performance, which might show a non-negligible heterogeneity across different subjects and experiments. Moreover, a component of $\Delta\phi$ is dependent on flow velocity. This fact enhances the variability of labeling efficiency among subjects, experiments and different physiological states, too. Therefore, labeling efficiency plays a critical role in perfusion quantification from pCASL data. It depends on factors whose entity shows both inter and intra-subject variability, making numerical simulations an inappropriate tool to assess its value. For these reasons, the most appropriate way to take inversion efficiency into account is to directly estimate it from data. A recent proposed method (Shin et al., 2012) to obtain optimal labeling efficiency consists in the addition of a separate calibration scan to minimize $\Delta\phi$, introducing a series of short scans interleaved by automatic routines to calibrate the scanner on a subject by subject base. In (Aslan et al., 2010) instead, a method for in vivo determination of inversion efficiency in pCASL experiments is proposed. The idea underlying this method is to obtain two measures of total perfusion (or whole-brain perfusion) of the same subject in the same physiological state: one measure does not require any inversion mechanism, and the other is consequence of inversion pulses application. Namely, the two measurements are performed

respectively with phase-contrast (PC) MRI, and pCASL techniques. A more thorough description of how this method can be implemented will be discussed in Chapter 7.

3.2 Tissue Preparation

As already said in section 1.2 a typical ASL experiment can be divided into three mostly independent blocks. The second block is the period between the end of the labeling procedure and the start of the image formation, called *readout* (discussed in section 3.4). This time is often not exploit but is needed to permit the labelled bolus to reach the tissues. It is extremely important that the imaging process starts when the bolus has already exchanged with tissues. This aspect has been largely debated since the first applications of ASL. A logical approach to solve this issue is to introduce a delay between the labeling and the readout block (Alsop and Detre, 1996). In case of PASL this interval is named inversion time or inversion delay (TI), whereas in CASL and pCASL is named post labeling delay (PLD). While CASL and pCASL have a well-defined bolus length because the labeling site is unique this is not the case for PASL. In the next section the approach to render insensitive PASL to bolus width will be introduced. Afterwards a review of the methods to null tissue contribution in order to eliminate signal fluctuation errors and improve SNR in ASL implementation is presented.

3.3 QUIPSS and Q2TIPS

In PASL the bolus width (τ) depends on the geometry of the vessels and on the velocity profile of blood flowing through them. Differently from CASL it is not well-defined and since the labeling domain is broader in PASL than pCASL the distribution of the bolus width is unknown and should be estimated from the data. A technique to eliminate this dependence has been proposed (Wong et al., 1998). In Quantitative Imaging Of Perfusion Using a Single Subtraction (QUIPSS and QUIPSS II) , a satura-

tion pulse is applied to the imaging slice at time TI_1 after the application of the tag 3.3.1. Because this pulse is applied for both the label and control images, it effectively removes any contribution to the difference signal of blood that arrives before TI_1. The image is acquired at time TI_2, after a delay of $\Delta TI = TI_2 - TI_1$, from the time of the saturation pulse. Thus, only tagged blood that enters the imaging slice between TI_1 and TI_2 contributes to the difference signal. If the following conditions are met,

$$\begin{aligned} TI_1 &> \delta t \\ TI_2 &< \delta t + \tau \end{aligned} \tag{3.9}$$

then tagged blood is entering the slice for the entire time ΔTI, and the estimation of perfusion is no longer dependent on τ.

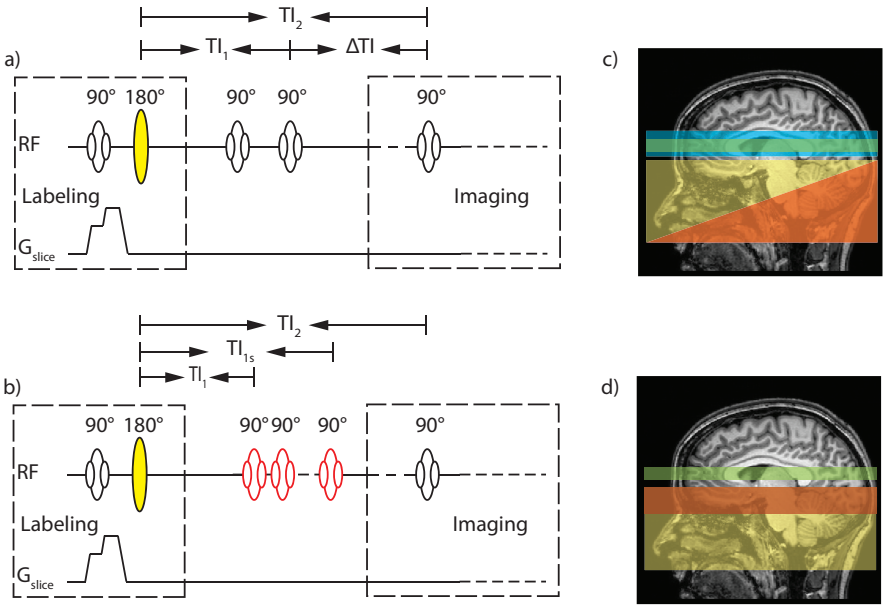

Figure 3.3.1: QUIPSS, QUIPSSII and Q2TIPS . In panel a) QUIPSS saturation scheme is reported. Blue band and red band in panel c) represent saturation location respectively for QUIPSS (within the imaging slice) and QUIPSSII (within the imaging region). The scheme for Q2TIPS is also reported in panel b and d). To be noted that in Q2TIPS the saturation pulses are replaced by a train of periodic saturation pulses.

A second version of QUIPSS, named QUIPSS II has been proposed. In

this modification, the saturation pulse is applied to the labeling region rather than the imaging slice. In this case the bolus is well defined by the saturation pulse and if the following conditions are met it is possible to eliminate the dependency from τ in the perfusion estimates:

$$\begin{aligned} TI_1 &< \tau \\ TI_2 &> TI_1 + \delta t \end{aligned} \tag{3.10}$$

Comparing the two techniques, QUIPSS II allows more time for the distribution of labeled blood water into the imaging region, generating a more homogeneous and hence more robust perfusion signal. However, residual errors remain due to incomplete saturation of spins over the slab saturated from QUIPSS II pulses. Furthermore, because of the imperfection of slice profile, a spatial mismatch of the edges of the saturation and inversion slab causes a not perfect cut of the bolus width. By replacing the original QUIPSS II saturation pulse with a train of thin-slice periodic saturation pulses applied at the end of the labeling slab, the accuracy of perfusion quantitation can be improved. This approach is named QUIPSS II With Thin-Slice TI_1 Periodic Saturation (Q2TIPS) (Luh et al., 1999).

3.3.1 Background Suppression

ASL is based on the subtraction between two images acquired in different conditions. The amount of available signal depends on the perfusion level but it might be completely disturbed by physiological fluctuations. In fact the mean cerebral blood volume in tissue is almost 5% and the difference signal. Perfusion is 20 time lower than the contribution of the static tissues. However, considering the measurement error, physiological fluctuations (cardiac and respiratory cycles) and motions, these are in the same order of magnitude as the ASL signal. The basic idea of background suppression is to attempt to null any contribution from the static tissues without modifying the ASL signal. In principle, this might be achieved using multiple inversion pulses. Specific tissues can be nulled according to to the number of IR pulses introduced. These pulses should

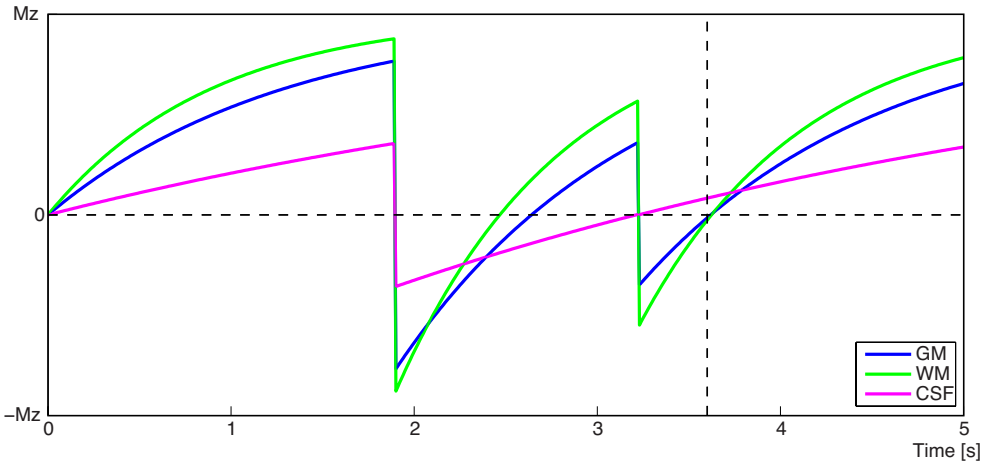

Figure 3.3.2: Example of Background Suppression technique. A saturation pulse is applied at the start of labeling and two inversion pulses are introduced to null Grey Matter (GM) (blue curve) and White Matter (WM) (green curve) signal at the time of readout (vertical dashed line). The signal of CSF (violet curve) is not completely suppressed with this pulse timing.

be inserted after the end of the labeling and before the start of the read-out.

This method has been firstly applied to angiography (Mani et al., 1997) and it has been quickly adapted to ASL (Ye et al., 2000). Taking as example an ASL sequence where a pre saturation pulse is introduced at the labeling time, the natural evolution of each tissue will follow a T_1 recovery and at time of readout the magnetization will have a slightly T_1 weight but in general will be almost full recovered. If some inversion pulses are introduced to null for example two specific tissues (both grey (GM) and white matter (WM)) the evolution of the recovery will be changed in sign at the time each inversion pulse is played (Fig. 3.3.2). In this case, at the time of read-out the contribution of GM and WM will be very low, proximal to be nulled and CSF signal will have a not completely suppressed signal but lower contribution compared to the case where no background suppression pulses have been introduced. Theoretically, the ASL signal should have not been changed by the inversion pulses since the magnetization of blood spins was inverted in the labeling process. However, since background suppression pulses are not perfect, a residual attenu-

ation of 17% of ASL signal has been found with the introduction of two suppression pulses (Ye et al., 2000), corresponding to an inversion efficiency of just 91% per pulse. In the light of this consideration the inversion pulse should be carefully optimized and in a published work (Garcia et al., 2005) four inversion pulses have been introduced to null the signal of almost the whole brain. Nevertheless, a 25% of signal loss has been documented. Background suppression is without doubt beneficial and it is advisable to use it when it is possible.

A consideration should be done on the type of readout used. With 2D readout, since the acquisition of each slice is made separately, the magnetization will experience a recovery during the readout producing not optimal signal suppression and a gradient of magnetization on the z direction. Hence, the use of 3D readout is advisable because the background suppression will be more effective. Indeed the slices will be acquired all at the same time and no recovery will be present in the z axis direction. This aspect of coupling readout with suppression pulses will be discussed in section 3.4. Even if optimal background suppression is desirable and a null magnetization limits the physiological noise increasing the reliability of ASL, it might also not be optimal for post-processing. A zero or proximal to zero magnetization results in impossibility to correct for motion and thus is advisable to regulate the background suppression pulses to keep 10% of magnetization to still have the possibility to perform motion correction or for co-registration purposes.

3.3.2 Vascular crushing gradient

A further module can be applied to ASL before starting the readout. It is actually possible to eliminate the residual contribution of macro-vascular contamination in the ASL signal. It is crucial to wait for the right time before starting the acquisition, since it is possible, especially in elder or pathological populations, to experience very low blood velocity and hence a very late arrival time in the micro-vasculature. This can lead to an overestimation of perfusion since the labeled blood is still in the ar-

teries and it has not been exchanged in the capillaries yet. If the actual arrival time is unknown, it is possible to crush the signal of the blood responsible of these artifacts. Indeed the vascular crushing gradients act as a filter, not passing spins that are traveling at velocity higher than a particular threshold, namely cut-off velocity (V_c). This module is similar to Velocity selective ASL module previous described in section 3.1.4.

It has been shown that is possible to use a couple of bipolar gradients in the slice selection direction to crush vascular signal (Schepers et al., 2003; Wong et al., 1998; Ye et al., 1997). The two lobes of the gradient couple, with equal area and opposite sign, can introduce a phase shift for moving spins only. For spins with a constant velocity the phase shift is linearly dependent on velocity. Ahn et al. (1987) described the effect of a gradient couple on the phase evolution for a parabolic flow profile in a circular tube. If the laminar flow condition is satisfied, the average signal in a circular tube can be described by:

$$M_z = sinc\left(cG_{cr}v_{max}\right) \tag{3.11}$$

If a rectangular form of the gradient is employed, M_z is the total longitudinal magnetization, c is a constant equal to $2\gamma\delta\Delta$, where δ is the gradient lobe duration, Δ gradient moment (distance between the centers of the two gradient lobes), G_{cr} represents the crusher gradient strength at maximum and v_{max} is the maximum flow velocity in the center of the tube. In Fig. 3.3.3 the behavior of M_z in function of both the gradient strength and the velocity in the tube is shown.

The cut-off velocity is represented by the first zero crossing of the sinc function and it is referred as the velocity of crushing, i.e. spins flowing at velocity above this threshold will experience a magnetization attenuation (Schepers et al., 2003). Usually the crusher gradients are expressed in form of b-value (b)(Bernstein et al. (2004), chap. 9.1):

$$b = \gamma^2 \int_0^{TE} \left[\int_0^t G(t')dt'\right]^2 dt \tag{3.12}$$

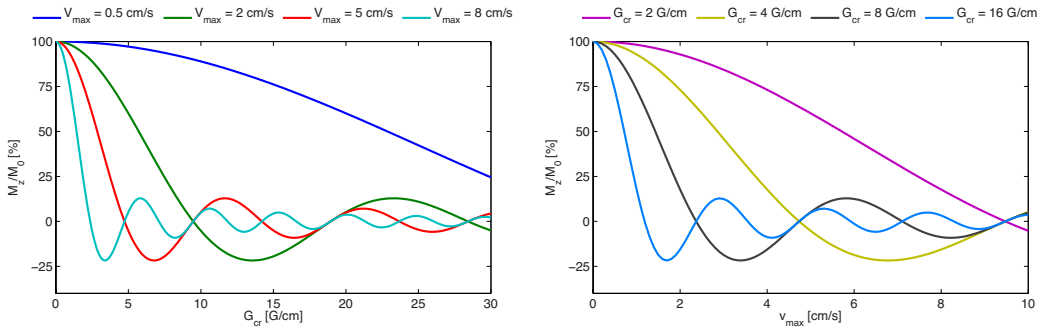

Figure 3.3.3: Simulation of vascular crushing gradient effect on longitudinal magnetization. On the left is reported the attenuation experienced by moving spins at different gradient amplitudes in correspondence at fixed velocity. Vice versa, on the right is reported the effect of fixed gradient amplitude on a range of possible spins velocities.

The b-value can be calculated in function of the shape of the gradient couple employed. In Fig. 3.3.4 are reported the form of b-value for a rect function used to simulate the magnetization evolution of Fig. 3.3.3 and another shape proposed in (Schepers et al., 2003).

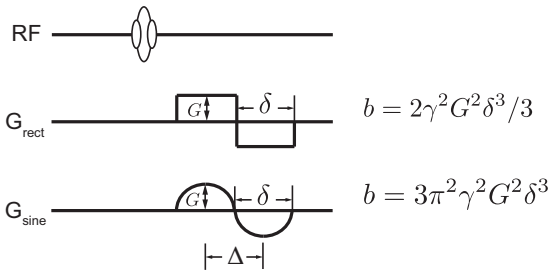

Figure 3.3.4: Commonly used vascular crushing gradient waveforms in gradient echo sequences and their corresponding b-values.

The use of vascular crushing gradients in ASL has been largely investigated but its employment is not straightforward. Indeed, it is not advisable to turn it always on, because it might interfere with pathological status such as tumors or other pathologies. Its use has to be considered as a manual implementation and the user should decide whether to apply them or not, conscious of their effects. For example in tumors it might be useful to apply them, since they could crush the bright signal in zone of

angiogenesis and reveal subtle tissue phenomena.

Repeating the acquisitions both with and without turning on vascular crushing allows to extract both macro and microvascular signals. They can be coupled in sophisticated models as the one that will be presented in chapter 6. Usually the application of the crushing gradients is limited only to the z-axis direction but it might be applied also to multiple directions as in (Petersen et al., 2006; Schepers et al., 2003).

3.4 READOUT

The third block in a typical ASL experiment is the *readout* block. All the precedent operations made on the signal are a sort of preparation of the magnetization that in this block will be transformed into images. To better understand the different readouts it is useful to review some concepts of how images are formed and reconstructed from RF pulse excitations. RF pulse itself does not contain any spatial information. A method to include spatial information is to employ gradient fields. These are magnetic fields aligned with the principal magnetic field B_0, but several orders of magnitude smaller ($m - \mu T$). The magnitude of the gradients varies spatially. A method to visualize these gradients is to take the field of view (FOV) and describe each dimension (x,y,z) using a gradient, i.e. each dimension is characterized by spatial variation of a gradient field. The total magnetization experienced by a position r in the FOV becomes:

$$\mathbf{B}(r) = B_0 + G_x x + G_y y + G_z z = \mathbf{B}_0 + < \mathbf{G}, \mathbf{r} > \tag{3.13}$$

If gradient fields are applied, the pulsation at which each spin of the sample r precesses around B_0 will depend on its position within the FOV:

$$\omega(r) = \omega_0 + \gamma < \mathbf{G}, \mathbf{r} > \tag{3.14}$$

The phase, $\phi(r, t)$, of a spin will also be spatially dependent and can be

written as:

$$\phi(r,t) = \gamma \int_0^t (G_x x + G_y y + G_z z)\, d\tau = \gamma \int_0^t < \mathbf{G}, \mathbf{r} > d\tau \tag{3.15}$$

In this way making a demodulation of the acquired signal, a code/decode operation can be made, retrieving the spatial information encoded with the gradient fields.The signal acquired in a MR experiment can be written as:

$$S(t) = \int_{-\infty}^{+\infty} \int_{-\infty}^{+\infty} \int_{-\infty}^{+\infty} \rho(r) e^{i\phi(r,t)} dx dy dz \tag{3.16}$$

where $\rho(r)$ is the effective proton density (PD), a quantity proportional to the number of water spins in the imaged sample and to the transverse magnetization of r (Haacke et al., 1999).

Introducing a new vector, $k(t)$, defined as:

$$k(t) = \frac{\gamma}{2\pi} \int_0^t G(r,\tau) d\tau \tag{3.17}$$

Eq. 3.15 can be rewritten simply as $\phi(r,t) = 2\pi < \mathbf{k}(r,t), \mathbf{r} >$. By substitution, the signal in Eq. 3.16 becomes:

$$S(t) = \int_{-\infty}^{+\infty} \int_{-\infty}^{+\infty} \int_{-\infty}^{+\infty} \rho(r) e^{i2\pi < \mathbf{k}(r,t), \mathbf{r} >} dx dy dz \tag{3.18}$$

It is easy to note that Eq. 3.18 represents the 3D Fourier transform of the proton density, $\rho(r)$. Since $\rho(r)$ is defined in a coordinate system $\mathbf{r}(x,y,z)$, the new vector $\mathbf{k} = (k_x, k_y, k_z)$., named *k-space* can represent the coordinate system describing the domain of the acquired signal.

This framework can be used to represent the acquisition of magnetic resonance images. Indeed once the magnetization is prepared, it is possible, with a series of gradients and pulses, to walk through the k-space, obtaining the actual Fourier transform of the signal and applying its inverse to form the images (Fig. 3.4.1).

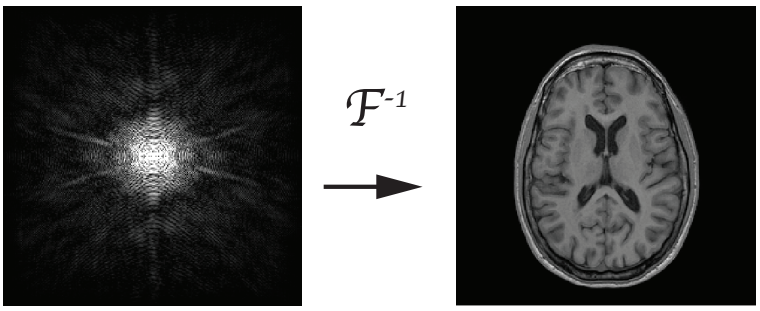

Figure 3.4.1: An axial slice of a T_1 weighted anatomical image (right) and its Fourier transform represented in *k-space*.

A useful way to describe readout approaches is to report the sequence diagram. Each sequence diagram has a line for each gradient (G_x, G_y, G_z) and RF excitation pulse applied. Usually G_x refers to frequency encoding (FE) gradient or read gradient, while G_y refers to phase encoding (PE) gradient and G_z to slice selection gradient (SE). An application of slice selection gradient has been shown previously when labeling approaches have been presented. Indeed applying SE gradients is a simple way to restrict the action of RF pulses to a selective region of the FOV. This type of pulses are called selective, while they are called non selective when no slice selection gradient is applied. A very easy way to understand sequence diagrams is to link them to k-space readout. Restricting the image formation to a 2D approach (3D approach is a natural extension) in order to acquire an image we have to read the whole k-space. Fig. 3.4.2 shows a simple diagram that describes the acquisition of one line of the k-space. Extending it to a discrete number of lines it is possible to read all the k-space. Indeed to acquire a 2D image, the sequence represented in Fig. 3.4.2 must be repeated allowing the PE gradient to change in amplitude.

The time between the acquisition of consecutive k-space lines is called repetition time, TR. Moreover, it is possible to acquire more than one line during a TR, hence the actual definition of TR is the time between two different RF excitation pulses. The way to read to k-space it is defined with

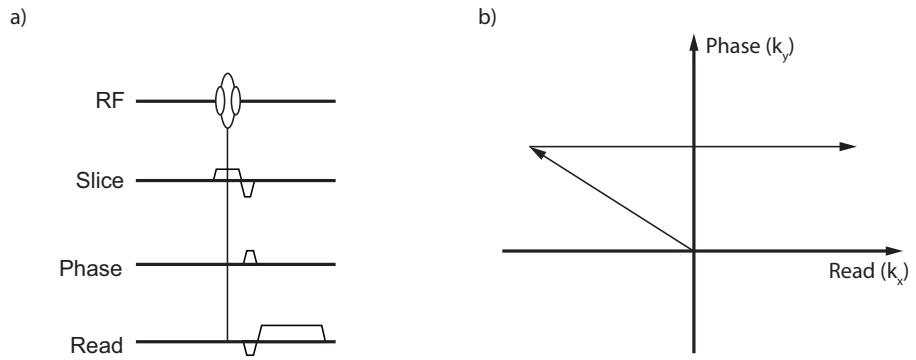

Figure 3.4.2: A simple sequence diagram describing how it is possible to read a single line in a 2D k-space. The phase gradient and the first negative lobe of the read gradient move from the center of k-space to the upper corner on the left. Then the prolonged lobes of the read gradient are used to read a single line. Repeating this process with different phase encoding gradients leads to read the whole k-space.

a number of functions called trajectories. Several trajectories have been proposed to form images. Each of them requires characteristic problems to face off and different weights can be obtained tailoring accordingly pulses and gradients. The time needed to acquire a 2D MR image, the scan time, is defined as the number of RF pulses multiplied by TR. Depending on the TR used, scan time can be in the order of several minutes. This is unsuitable if the aim of the study is to describe quick phenomena like cardiac function, brain activation in functional imaging (fMRI), the diffusion of water in biological tissues (diffusion MRI) or obviously as we saw before, perfusion MRI and ASL in particular. The primary requirements for a readout approach in ASL is that it should be as fast as possible to catch the moment and take a snapshot of the exchanges of the blood into the capillaries or even faster to record the entire description of the kinetic as a movie of its evolution.

3.4.1 SINGLE TI

The description of possible readout approaches for ASL will be divided into two categories, called single-TI and multi-TI acquisition (see section 3.4.2). The idea on which the former is based is that, it is possible, under

some hypothesis, to reduce the acquisition of perfusion weighted images only to a single time point. Indeed if we ensure that the tracer is arrived in the micro-vasculature to exchange with tissues it is possible to acquire only a couple of control and label images to achieve a perfusion estimation. The total acquisition time for a single-TI ASL experiment can be calculated as the multiplication of the time needed to acquire a couple of control and label collections of slices (called volume) and the number of volume to be averaged to increase the SNR. Thus, a very fast readout module is desirable.

3.4.1.1 2D ECHO PLANAR IMAGING

In Echo Planar Imaging (EPI) technique a rapid series of gradient echoes is generated to cover the k-space in a back and forth scanning pattern, after a single excitation pulse. In Fig. 3.4.3 an EPI k-space sampling trajectory and simplified pulse sequence diagram (for a single-shot EPI, i.e. a single volume is acquired in one TR) are shown. To link the k-space trajectory with the gradient it is possible to use this easy rule: the integral of the gradients tell us where we are in the k-space. For example, to move from the k-space center to the initial point of the EPI trajectory a negative gradient on FE direction and a positive one on PE direction should be applied: this initialization is shown both in the sequence diagram (green gradients) and in the k-space (green dashed line) in Fig. 3.4.3.

The initial pulses move the location of k-space sampling to $(-k_{max}, k_{max})$ along FE and PE axis, and then the repetition of the gradient echo module produces a back and forth scanning of k-space. To change the line in k-space (moving down in the example in Fig. 3.4.3) small gradients called blips are applied in PE direction. Since the whole k-space must be filled following a single excitation pulse, the data must be acquired before significant T_2^* decay can occur (typically the acquisition window is limited by this effect to about $100\ ms$). To confine data acquisition in a temporal window shorter than T_2^* and maintaining at the same time a reasonable spatial resolution (i.e. sampling a large number of line in k-space), strong

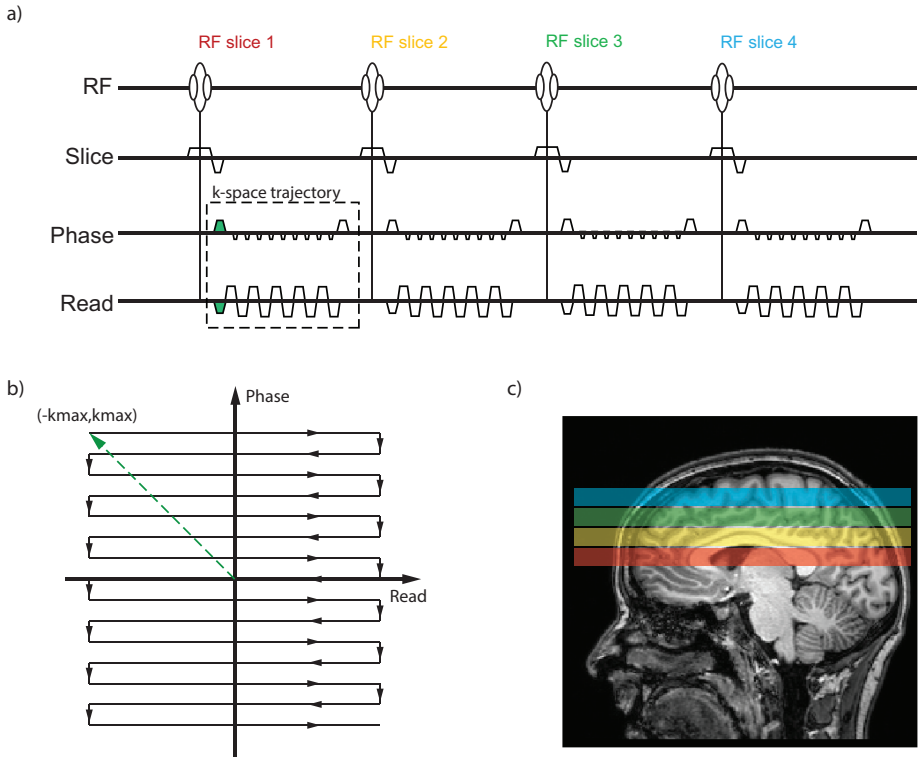

Figure 3.4.3: Initial negative Read and positive Phase gradients moving the sampling point to the upper-left of the k-space. Then the boxed pulses are repeated $\frac{N}{2}$ times to acquire N lines of k-space in alternate direction. The sign of FE gradient indicates whether the trajectory of the straight line along Read (k_x) moves from left to right (positive value) or in the opposite direction (negative value). The small y gradients pulses, called blips, shift the k-space sampling to a new line in an upper Phase (k_y) level.

gradients and rapid switching capabilities are required. The total imaging time, indeed, depends on how quickly the sampling of the k-space grid occurs. Indeed, the scan time per slice is usually in the order of tens of milliseconds. The most common EPI artifacts derive from inhomogeneities in the magnetic fields (both static and gradient field) that result in signal losses and geometrical distortions. As it has been presented above, EPI gives a extreme advantage in term of speed in the acquisition. Thus, 2D single-shot EPI is a candidate for readout in ASL applications. However, artifacts due to susceptibility and inhomogeneity of B_0 and B_1 should be taken into account as drawbacks of this technique.

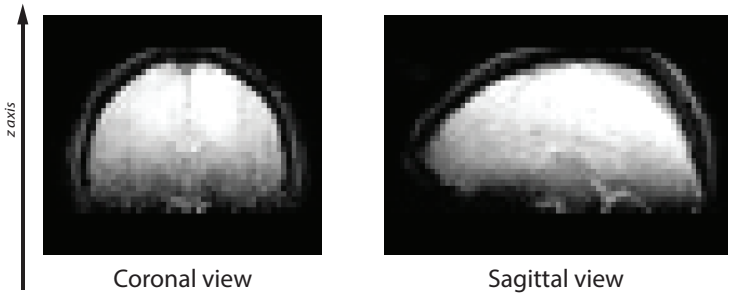

Figure 3.4.4: A 2D single-shot EPI volume acquired with the application of two background suppression pulses. It is possible to see a gradient due to the recovery of the tissue during the acquisition of separate slices. An optimal and uniform background suppression has been obtained only for the first slice.

The coupling of 2D single-shot EPI with background suppression in ASL application is not optimal. As we saw in section 3.3.1 the magnetization preparation ability to null the signal of the tissues is true for the starting point of the readout module. Since each slice is acquired within a different RF pulse, different slices will experience different magnetization status. In this context the T_1 relaxation of tissue will start from the first slice (null level) and will decay with T_1 producing a gradient in the z direction as is possible to see in Fig. 3.4.4. As an alternative of EPI it is possible to employ other fast imaging strategy like 2D Spiral. Spiral allows to reduce T_2^* weighting using a shorter TE. However it suffers of blurring in the in plane resolution in presence of resonance offsets.

3.4.1.2 3D Gradient and Spin Echo

The first Gradient and Spin Echo (GRASE) sequence was presented in 1991 (Oshio and Feinberg, 1991). 3D-GRASE is a variant which was presented later and it is a very fast 3D imaging technique in a single shot (Günther et al., 2005). After the magnetization preparation, a spin echo is prepared by applying a refocusing pulse ($180°$ pulse in Fig. 3.4.5).

The basic idea of 3D-GRASE is to acquire one 2D-EPI readout module on each spin echo, while preparing another k-space partition in z direction (in 3D readouts partition represents generally a slice but often an overlap between partitions is used and a slice will be the result of multiple partitions excitation). The center of k-space in frequency and phase direction of each partition is sampled on the occurrence of a spin echo, thus acquiring maximal signal at frequencies containing the maximum contrast (in k-space low frequencies are responsible of the contrast while high frequencies of the edges and signal variations in the images). Between two refocusing pulses, another partition is encoded. With a centric reordering scheme, the first acquired partition is the central k-space partition. Afterwards, the next upper and lower partitions are encoded, in alternating order. The center of k-space is therefore acquired on the first spin echo, at TE.

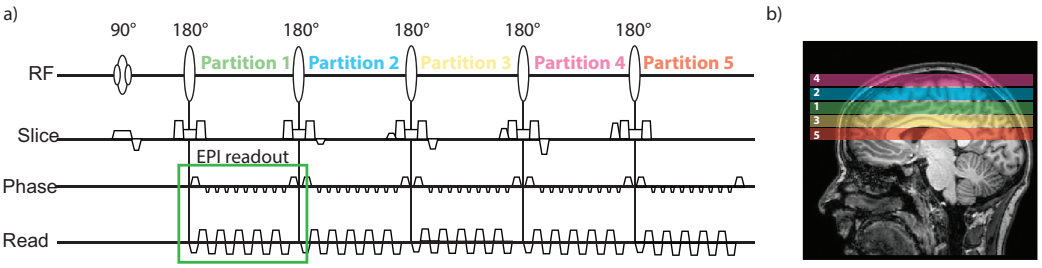

Figure 3.4.5: Sequence scheme for a single-shot 3D-GRASE readout, adapted from Günther et al. (2005). Each partition is acquired after a refocussing spin echo RF pulse. The single partition is acquired using an EPI readout (green square). The partitions are acquired on a interleaved based fashion.

The main advantage of 3D readouts is the perfect coupling with back-

ground suppression techniques. Since each volume is acquired in the same RF excitation and the read trajectory of k-space is obtained refocussing the signal producing spin echoes, the whole volume is sharing the same magnetization preparation. The major drawback of 3D-GRASE readout is the blurring effect occurring in *z-axis*. The through-plane blurring is due to T_2 decay during the long spin echo train applied. In Fig. 3.4.6 it is possible to appreciate the blurring artifact. To correct for this several methods have been proposed. Some of them try to solve the problem from the physical point of view segmenting the readout reducing the T_2 decay and increasing the scanning time (Balteau et al., 2013) while others from the post processing point of view (Boscolo Galazzo et al., 2013). The best solution would be to combine these two categories of approaches to obtain the best tradeoff. A thorough comparison of 2D and 3D readouts has been carried out by Vidorreta et al. (2012). The results of this comparison suggest to use 3D approaches and Background suppression technique to enhance the investigation power of ASL in both perfusion and functional activity measurements.

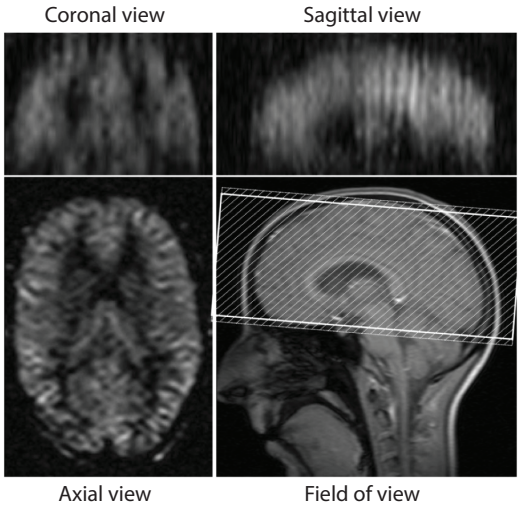

Figure 3.4.6: Example of single-shot 3D-GRASE readout, taken from Günther et al. (2005). It is worth to note the blurring artifact along the z axis. This artifact can be attenuated using segmented 3D-GRASE or in post-processing applying de-blurring procedure.

3.4.2 MULTI TI

Single TI ASL acquisitions have been widely used in both research and clinical environments. The major limit of this kind of acquisition is that the only parameter that can be estimated is the perfusion level of tissues. A second drawback is the strong sensitivity of single-TI ASL signal to bolus arrival time. Multi-TI approaches consist in sampling the tracer describing its travel towards the vessels, monitoring the exchange with tissues and finally seeing its disappearance after the decay of the magnetized blood. In order to obtain the whole kinetic curve of the tracer, it is required to repeat the measurement changing TI (or PLD). Thus, this method allows to estimate both perfusion and the bolus arrival time and other physiological parameters (see chapter 4). The major drawback of this approach is that it is more time consuming. In principle a multi TI experiment is just the repetition of a single TI one. Thus each supplementary TI used will add time to the acquisition. Theoretically to estimate two parameters it is sufficient to have two measurements but it is desirable to have many acquisitions to use more complicated models to extrapolate additional information from the investigation.

3.4.2.1 LOOK AND LOCKER READOUT

An elegant method to speed up the acquisition is to use a Look-Locker readout (LL). This approach takes its name from the two investigators that proposed it (Look and Locker, 1970). It has been consequently employed in fast T_1 measurements (Gowland and Leach, 1992) and modified to be combined with EPI readouts (Gowland and Mansfield, 1993). In these works the Look-Locker readout is used to map the T_1 value of the whole brain using an inversion recovery and driving the relaxation to a steady state. The readout is composed by a single inversion pulse and several pulses with a low flip angle followed for example by an EPI readout to sample the whole brain. Usually the signal evolves like an inversion recovery (Eq. 2.12) but after the first pulse the effective magnetization is driven by the flip angle following $M_z(TI_+) = M_z(TI_-) \cdot cos(FA)$.

In this time being the magnetization can be read with the scanner on the transversal magnetization $M_{xy}(TI_+) = M_z(TI_-) \cdot sin(FA)$. The magnetization will not recover from the original magnetization because it has been subjected to a RF pulse. Repeating this process produces a sawtooth signal that oscillates near a lower M_0 called $M_{0,eff}$. It is possible to calculate the limit of the theoretical evolution of a inversion or a saturation recovery from the Block equation (Gowland and Mansfield, 1993). Indeed, the longitudinal magnetization in function of the n-th pulse can be written as:

$$M_z[n] = M_0 \cdot \left[\left(1 + \left(\frac{M_{z+}}{M_0} - 1\right) e^{-\frac{TI_1}{T_1}}\right) \cdot \left(cos(\alpha) \cdot e^{-\frac{\Delta TI}{T_1}}\right)^{n-1} + \left(1 - e^{-\frac{-\Delta TI}{T_1}}\right) \cdot \frac{1-\left(cos(\alpha) \cdot e^{-\frac{\Delta TI}{T_1}}\right)^{n-1}}{1-\left(cos(\alpha) \cdot e^{-\frac{\Delta TI}{T_1}}\right)} \right] \tag{3.19}$$

If $M_{z+} = 0$ then this equation can describe a saturation recovery experiment while if $M_{z+} = M_0$ it can model an inversion recovery experiment. The signal read after the n-th excitation pulse can be written as:

$$M_{xy}[n] = M_z[n] \cdot sin(\alpha) \cdot e^{-\frac{TE}{T_2^*}} \tag{3.20}$$

and considering the limit for $n \to \infty$ it is possible to calculate the effective steady magnetization $M_{0,eff}$ driven from the Look-Locker pulses:

$$M_{0,eff} = \lim_{n \to +\infty} M_z[n] = M_0 \cdot \frac{1 - e^{-\frac{\Delta TI}{T_{1t}}}}{1 - cos(\alpha) \cdot e^{-\frac{\Delta TI}{T_1}}} \tag{3.21}$$

The perceived magnetization (dashed blue line in Fig. 3.4.7), i.e. the effective magnetization read by the scanner, will follow a new exponential law whose decay constant is:

$$T_{1,eff} = \frac{1}{\frac{1}{T_1} - \frac{log(cos\alpha)}{\Delta TI}} \tag{3.22}$$

Thus, both $M_{0,eff}$ and $T_{1,eff}$ can be estimated from an inversion or satu-

ration recovery experiment using a Look-Locker readout module. In Fig. 3.4.7 a simulated inversion recovery acquisition is reported.

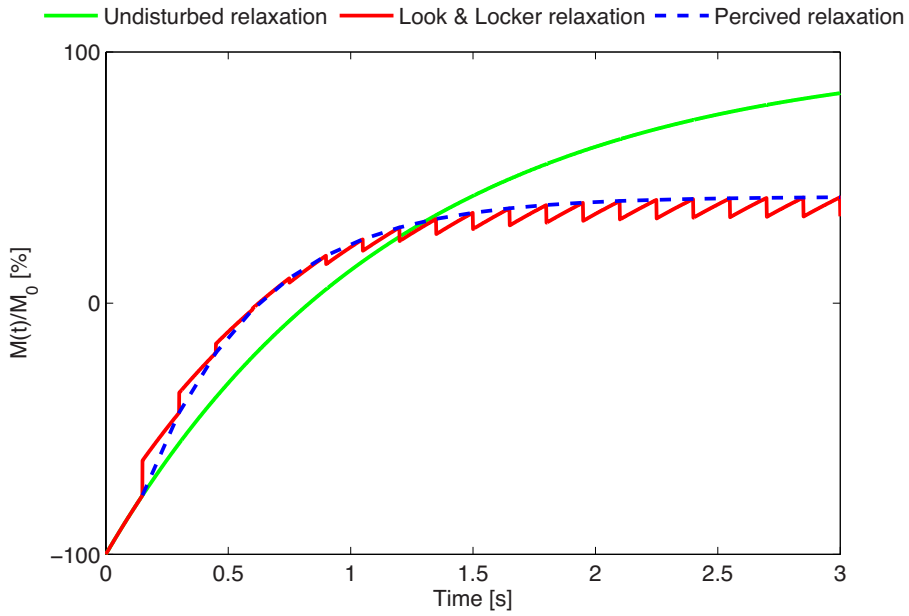

Figure 3.4.7: Inversion recovery with a Look-Locker readout module. The undisturbed T_1 relaxation is plotted as reference with a green solid line. The dashed blue line represents the perceived relaxation while the red solid line the true Look-Locker relaxation. It is possible to note that the Look-Locker readout drives the magnetization to a steady state lower in magnitude than the true one. This example have been simulated for $T_1 = 1.2s$, $TI_1 = 150ms$ and $\Delta TI = 150ms$.

The application of this particular readout to ASL has been employed and adapted to many sequences. The first application proposed was combining a FAIR labeling scheme (Günther et al., 2001). Then also a STAR labeling has been used (Petersen et al., 2006) (see section 3.5). In the last years Look & Locker readout allowed the use of more complex models adding several features to the ASL quantification process (Brookes et al., 2007; Francis et al., 2008). A pCASL labeling has been also applied (Chen et al., 2011). A viable alternative to perfusion studies has been presented also combining pCASL, Vessel selective ASL and Look-Locker single slice readout to produce angiography images (Okell et al., 2010). Lastly it has been applied to ASL to estimate partial volume effect (Petr et al., 2013).

3.5 QUANTITATIVE STAR LABELING OF ARTERIAL REGION

Among ASL techniques a very elegant approach developed in 2006 is the QUAntitative Star labeling of Arterial Region (QUASAR) (Petersen et al., 2006). This section will introduce the sequence and its principles. A more detailed description of the methods used for analysis of QUASAR data will be discussed in chapter 4. QUASAR is a modified version of a STAR sequence. The first modification was introduced with Pulsed Star Labeling of Arterial Regions (PULSAR) (Golay et al., 2005) and it naturally evolved in QUASAR afterwards. PULSAR was substantially a regional perfusion imaging technique (RPI) or territory mapping technique, born to overcame limitations of traditional RPI techniques very sensitive to RF inhomogeneities at high fields. PULSAR is a STAR labeling technique coupled with a 2D multi-slice EPI readout (Edelman and Chen, 1998) with built-in a water suppression enhanced through T_1 effects (WET) pre-saturation module used to proper pre-saturate the imaging volume (Ogg et al., 1994). The major innovation of QUASAR is the combination of PULSAR with QUIPSS II to achieve a good bolus timing and definition (Petersen et al., 2010a) and the introduction of a Look-Locker Readout to sample the entire kinetic evolution of the ASL signal. The entire experiment is then repeated with the use of a bipolar crushing gradient scheme to retrieve information of tissue exchange. In Fig. 3.5.1 is reported the sequence scheme of QUASAR, taken from Petersen et al. (2006).

The QUASAR sequence has introduced another important concept already suggested by Barbier et al. (2001) to extract information about the macro-vascular component of the ASL signal. The basic idea is to consider the signal acquired without the use of vascular crushing gradients as the sum of both the micro-vascular (or tissue) component and the macro-vascular (or arterial) component. Vice versa, subtracting from the uncrushed signal the crushed signal it is possible to obtain the macro vascular component. This idea has introduced a new framework of analysis for ASL data: the use of a deconvolution approach to estimate the flow.

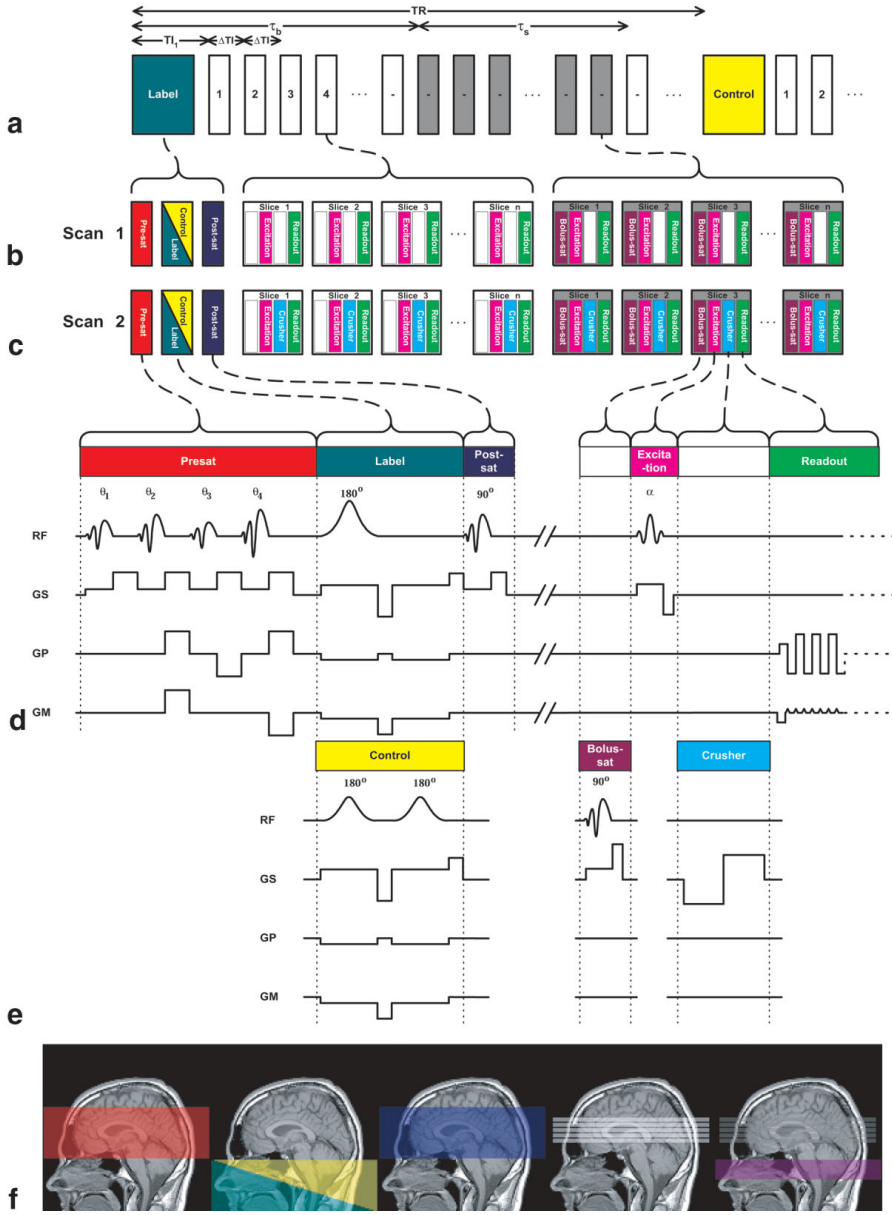

Figure 3.5.1: Taken from Petersen et al. (2006). QUASAR sequence. a) The overall structure, showing the spin preparation (labeling/control) followed by the multi-time-point, multislice readout that is interleaved with a bolus saturation sequence for the duration τ_s (shown in gray). τ_b is the temporal length of the labeled bolus obtained with a bolus saturation technique similar to QUIPSS (Wong et al., 1998). b) and c) The sequence components of the noncrushed and crushed experiments, respectively. d) and e) The actual RF and gradient scheme for presaturation, label/control, postsaturation, bolus saturation, and excitation followed by readout with or without crusher. f) (left to right) Presaturation slab, label/control region, postsaturation slab, image acquisition without bolus saturation, and image acquisition with bolus saturation.

Indeed it is possible to use the macro vascular component as the input function of a linear system and the tissue as the output. The characteristic function (or impulse response) of the system is related to the behavior of the system itself and hence to perfusion. In chapter 4 an extensive review of this method and the framework used will be introduced.

Nothing is as simple as we hope it will be.

Jim Horning

4

State of the art: ASL models for quantification

This chapter gives a review of the existing models used to estimate perfusion and other important parameters from Arterial Spin Labeling dataset. Buxton model (Buxton et al., 1998) it is the most applied model for this purpose. It is also called ASL kinetic model. More complicated have also been presented, based on multi compartmental modeling approaches (Parkes, 2005; St Lawrence et al., 2000). Moreover, these models can be enriched taking into account pitfalls and other non-desiderate artifacts that can hamper the quantification process of ASL data, such as modeling the effect of macrovascular component (Chappell et al., 2010) or noise reduction filtering (Wells et al., 2010b). ASL and its natural flexibility has also been used to study the vascular tree within an angiographic framework (Okell et al., 2012). To estimate parameters from physiological models many techniques could be applied. A brief review of the most used meth-

ods for ASL parameters estimation will be discussed to introduce how it is possible to include a priori knowledge in the quantification process (Carson and Cobelli, 2001; Chappell et al., 2009; Cobelli et al., 2002).

As already introduced in chapter 3, ASL produces a series of label and control images, which subtracted ones from the others (respecting the labeling scheme used, see section 3.1.1.1) provide a series of perfusion weighted images (PWI). The value present in each voxel represents the contribute of blood flow at the time in which the acquisition has been made. If ΔM is the value of a difference image voxel, we can distinguish two types of contribution in it:

- $\Delta M^{(phy)}$: the effect due to the physiological exchange of blood in the tissues (labeled arterial blood) that is represented in PWI.
- $\Delta M^{(non-phy)}$: all the other effects that are not desirable and are not related to the physiological functioning of the brain. Typical examples of these contributions are off-resonance and magnetization transfer effects (MT), which are caused by imperfections and technical limitations in ASL implementation. They are typically called *subtraction errors* since their presence reflects unexpected discrepancies between label and control images.

Thus, the ASL signal could be thought as the sum of these two groups of magnetization difference contributions:

$$y = \Delta M^{(phy)} + \Delta M^{(non-phy)}$$

The main assumption that is made when parametric models are used to estimate perfusion is that the second contribution, $\Delta M^{(non-phy)}$, can be generally ignored. This is because quantification methods assume that the control and label subtraction is ideally perfect, and so no subtraction errors contribute to the measured signal. Every potential issue that can contribute to $\Delta M^{(non-phy)}$ contributions should be previously accounted by appropriate preprocessing steps (e.g. motion related errors) or using

technical solutions which could prevent or reduce them (MT transfer effects or off-resonance). Under this hypothesis the measured ASL signal is simply proportional to the difference in longitudinal magnetization in the tissue due to blood that entered the voxel and is still present at the measurement time.

To make it more clear, it is helpful to think as there were two groups of spins, defined by their location just after the labeling inversion pulse: (a) static untagged tissue spins in the image voxel, and (b) tagged arterial blood spins that travel to the voxel. Then the essential assumption is that the longitudinal magnetization of the first group is identical during the two parts of the experiment. It means that the signal difference ΔM only depends on the difference of the longitudinal magnetization of the labeled blood, and gives a direct measure of how much of the original arterial magnetization, created by the inversion pulse, has been delivered to the voxel and survives at the time of measurement. Every model proposed to quantify ASL data assumes that the static tissue is subtracted accurately, and focuses on the interpretation of the difference signal as a measure of magnetization delivered by arterial flow (Buxton et al., 1998).

The perfusion-weighted signal, that ASL technique produces, reflects perfusion of the tissue f, but also depends on a number of factors that are not directly related to perfusion itself. Transit of labeled blood in large vessels not perfusing the tissue through which they pass, distance between labeling region and imaging voxel which varies on voxel location, magnetization relaxation time function of tissue type (and of readout) are some examples. All these confounding effects must be taken into account along with other calibration factors and parameters which define the absolute scale of the signal. Inversion efficiency and the equilibrium magnetization of arterial blood have to be measured or supposed to be known, if an absolute quantification of perfusion is required. Acquired data y are thus dependent on a set of factors, that have to be described by ASL models:

$$y = \Delta M(t, f, T_{1t}, T_{1b}, \alpha, M_{0b}, \Delta t, \tau, \ldots)$$

In table 4.0.1 a list of parameters considered in ASL-MRI data quantification, with their definitions and units, is reported. Usually not all of them are estimated directly from data but are instead fixed to literature values. The number of the parameters fixed will influence the flexibility of the model and hence its complexity. Here only a subset of all the possible parameters has been listed, since other parameters can be included to perform more complicated analysis (see section 4.3). Another possible approach is to enhance the acquisition protocol to collect data from parallel experiments and include them in a hierarchical model.

Parameter	Description	Unit
f	perfusion	$\frac{mL}{g\,s}$ or $\frac{mL}{100g\,min}$
Δt	transit delay	s
τ	bolus duration	s
T_{1t}	tissue longitudinal relaxation time	s
T_{1b}	blood longitudinal relaxation time	s
α	inversion efficiency of labeling pulse	a.u.
M_{0t}	equilibrium magnetization of tissue	a.u.
M_{0b}	equilibrium magnetization of arterial blood	a.u.
λ	brain-blood partition coefficient	$\frac{mL}{g}$

Table 4.0.1: Parameters needed to perform an absolute quantification of perfusion, on a subject-based relation. Usually not all of them are estimated directly from data but are fixed to literature values. The number of the parameters fixed will influence the flexibility of the model and hence its complexity.

As has already discussed in sections 3.4.1 and 3.4.2, the main drawback of single TI acquisition is its sensitivity to the transit delay (Δt). Transit delay (also termed as arterial arrival time AAT, bolus arrival time BAT, or arterial transit time ATT) is the time that tagged blood takes to move from the tagging location to the considered voxel. This transit delay is needed by the tagged blood to travel towards the vascular tree between tagging and imaging regions. Δt is known to vary markedly across the brain; for example, longer transit delay are typically observed to the occipital lobe compared to the frontal-parietal-temporal lobe. These differences in Δt are completely independent from acquisition parameters

because they reflect the different pathways that labeled bolus follows to reach imaging voxels. Probably the posteriors cerebral arteries travel a longer distance parallel to the imaging plane to reach the occipital lobe, whereas the middle cerebral arteries travel directly upward to the parietal lobes (Figueiredo et al., 2005; MacIntosh et al., 2010b). In general, the network of cerebral arteries and arterioles exhibits a complex geometry, with blood supplying different parts of the brain following different trajectories at varying velocities, making Δt a variable parameter over the whole brain. Thus, Δt is somewhat governed by the vasculature, and provides useful information about its state: many pathological conditions are known to results in a very slow blood flow and consequently in very long transit time. Δt measurements also help to understand whether the hypo perfusion, typically found in cerebrovascular disorders cases, is due to actual flow deficit or an artifact due to the delayed arrival of labeled blood (MacIntosh et al., 2010a). Transit delay evaluation is thus a useful complement to perfusion measurement.

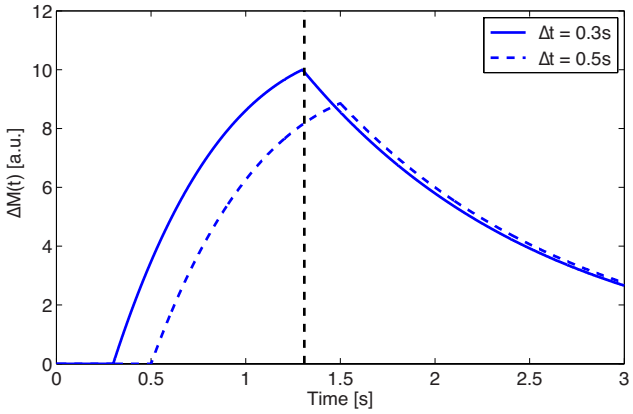

Figure 4.0.1: Example of two voxels having the same perfusion level but different Δt. Measuring signal at a single inversion time would result in a lower perfusion estimate at the voxel with longer Δt as compared with the voxel with shorter Δt.

The variability of Δt in the brain might lead to both underestimation and overestimation in perfusion estimates. Moreover, the regional differences in single TI experiments are detrimental. The method proposed to

overcome this limitation is to wait a sufficient long delay time, i.e. choosing a TI (or PLD) to sample the kinetic curve when the sensitivity to Δt is lower (Alsop and Detre, 1996). Nevertheless, the reduced sensitivity to Δt might be compromised whenever transit times are unexpectedly long (for instance in many pathological conditions) making this artifice ineffective. In addition, there is another consideration that potentially limits the advantages introduced by these techniques, especially for PASL data. The TI required to face prolonged Δt could be so long that it will degrade the SNR of the magnetization difference images, being higher the signal reduction that occurs due to magnetization relaxation. Since SNR is already a critical issue in ASL techniques, the use of a very long delay before imaging should be ideally avoided. This limitation can be overcome repeating the acquisition process at different TI.

4.1 ASL PERFUSION QUANTIFICATION

To extract quantitative perfusion measurements from ASL dynamic data, a detailed model of the process combining kinetics and relaxation is needed. There are two main approaches to model ASL experiments. They differ on how signal in difference image is interpreted when a model ΔM is built:

- **Modified Bloch Equation**: ΔM is thought to be a measure of concentration of labeled spins in difference images. It represents the measured signal of a system of compartments describing the distribution and the exchange of labeled water spins within the voxel. The equations of each compartment, which quantify the rate of change of longitudinal magnetization in each pool, are versions of Bloch equation modified by the inclusion of the exchange terms. That is, labeled blood water molecules act as the tracer of the system, and usual compartmental modeling is applied to it. A set of differential equations is written, each one describing the rate of change of this tracer concentration inside the compartment. Since the mea-

sured signal y is modeled as the magnetization due to labeled spin concentration within the voxel rather than an actual tracer concentration, a modification to this set of equations has to be introduced to take into account the magnetic properties of the ASL tracer. The final result is a set of reviewed Bloch equations describing the rate of change of the longitudinal magnetization of the labeled water molecules inside the compartment due to both relaxation and exchange processes. Single and multi-compartment models (accounting for finite capillary water permeability) have been proposed in literature (Parkes and Tofts, 2002; Williams et al., 1992).

- **Tracer kinetics model**: ΔM is considered to be the fraction of the original concentration of a tracer bolus that is still in the voxel at the time of measurement. The labeling procedure produces a bolus of inverted water spins which is treated like a general bolus of tracer delivered to the tissue by arterial flow, and cleared by venous flow. The experiment is described by a linear system whose input and output functions are respectively the arterial tracer concentration and the measured signal y, and whose impulse response lumps together all the underlying phenomenona involved in transport and uptake. In section 4.1.1 the tracer kinetic model in the context of an ASL experiment is reviewed, and a common version of this model, the Buxton model, is exposed in 4.2.

4.1.1 Tracer kinetic model for Arterial Spin Labeling

The tracer kinetic model directly derives from tracer kinetics theory which provides a mathematical description of the dynamic tissue concentration of any tracer delivered to the tissue by blood flow.

Dealing with ASL data, some adaptions to the general theory have to be inserted. The tracer considered here is labeled blood water, which is measured in term of quantity of magnetization instead of concentrations. The measured signal $y(t)$ is thus considered as a quantity of magnetization that is carried into the voxel by arterial blood. The amount of

this magnetization at a time t will depend on the history of delivery of magnetization by arterial flow and clearance by venous flow, and longitudinal relaxation (Buxton, 2002). These various physical processes can be described by defining three functions of time, that are called kinetic model functions:

- **delivery function** $c(t)$: is the normalized arterial concentration of magnetization arriving at the voxel at time t
- **residue function** $r(t, t')$: is the fraction of tagged water molecules arrived at time t' and still in the voxel at time t. This function contains most of the details of the distribution and the kinetic of the agent
- **magnetization relaxation function** $m(t, t')$: is the fraction of the original longitudinal magnetization tag carried by the water molecules that arrived at time t' and remains at time t. This function justifies the supplementary way in which the agent can outflow from the voxel in addition to venous flow.

If the physiological state of the tissue is not changing, then $r(t, t')$ and $m(t, t')$ are functions of just the interval $t - t'$, and could be written as $m(t)$ and $r(t)$, with t having that time difference meaning.

With these definitions the amount of magnetization delivered to a particular voxel between t' and $t' + dt'$ is $2\alpha M_{0b} f c(t')dt'$, where f is the perfusion, M_{0b} is the equilibrium magnetization of a fully arterial blood filled voxel, and α is the inversion efficiency. $2\alpha M_{0b}$ is the arterial magnetization difference after the labeling phase. The fraction of magnetization that remains at time t is $r(t-t') \cdot m(t-t')$. $\Delta M(t)$, the amount of magnetization in the voxel at time t, is simply given by adding up all the magnetization contributions that had arrived weighted by the probability that they are

still in the voxel:

$$\begin{aligned} \Delta M(t) &= 2\alpha M_{0b} f \int_0^t c(t')r(t-t')m(t-t')dt' \\ &= 2\alpha M_{0b} f \left\{c(t) * [r(t)m(t)]\right\} \\ &= fQ(t) \end{aligned} \tag{4.1}$$

Eq. 4.1 emphasizes the central role of the perfusion in determining the ASL signal, making explicit its perfusion-weighted nature. The measured magnetization difference is modeled as the product of f and $Q(t)$, that can be thought as a calibration factor that converts the local cerebral flow into a measured magnetization difference. This factor controls the SNR of the experiment: for a larger $Q(t)$ the same local f will produce a larger ASL signal difference $\Delta M(t)$.

Summarizing, the general ASL model needs to consider transit delays from the tagging region to the voxel, magnetization decay, exchange of water between blood and tissue, clearance by venous flow and different forms of arterial tagging. All of these processes can be taken into account with appropriate forms of the delivery function $c(t)$, the residue function $r(t)$ and the magnetization decay function $m(t)$.

4.2 The Buxton model

The Buxton model for ASL data is based on three key assumptions that, in the frame of the kinetic model, correspond to three particular forms for the functions $c(t)$, $r(t)$ and $m(t)$ (Buxton et al., 1998).

1. The arrival of labeled blood at a particular voxel is assumed to be via uniform plug flow. This leads to a piecewise definition of the delivery function which allows the labeled blood to enter the voxel only in a precise temporal window defined by two parameters: transit delay Δt, and bolus duration τ. The transit delay Δt is the time required to labeled blood to begin to appear in the tis-

sue voxel after the start of labeling, and its role has been previously investigated. The bolus duration τ is the temporal extent of the delivery of labeled blood to the voxel. These two parameters define when the perfusion process becomes detectable by the ASL experiment, therefore they are directly related to the physiological state of the tissue and how the labeling is accomplished. The meaning of uniform plug flow assumption is that $c(t)$ is nonzero only in the interval $\Delta t < t < \Delta t + \tau$. For continuous or pseudo-continuous labeling $c(t) = e^{-\frac{\Delta t}{T_{1b}}}$, while for pulsed labeling $c(t) = e^{-\frac{t}{T_{1b}}}$.

2. The kinetics of water exchange between tissue and blood are assumed to be described by a single compartment kinetics: independently from the number of compartments that may exist within the tissue, compartment are undergoing such rapid exchange of water that their concentration ratios remain constant even though the total tissue concentration is function of time. This means that the tissue concentration $\Delta M(t)$ and the venous concentration $\Delta m_v(t)$ are equal once they are corrected for the different water content between blood and tissue. It has been shown that this assumption is equivalent to take the exponential form for the residue function $r(t) = e^{-\frac{f}{\lambda}t}$.

3. As soon as the labeled water molecules have reached the tissue voxel, the magnetization is assumed to decrease with the relaxation time of the tissue T_{1t}. This essentially means that water is completely extracted form the vascular space immediately after its arrival in the voxel. Thus magnetization relaxation function is given by $m(t) = e^{-\frac{t}{T_{1t}}}$.

The standard model can be summarized, in terms of delivery, kinetics and relaxation functions, as:

$$
\begin{aligned}
c(t) &= \begin{cases} 0 & t \leq \Delta t \\ \hline \mathrm{e}^{-\frac{t}{T_{1b}}} \quad (\text{pulsed}) & \\ \mathrm{e}^{-\frac{\Delta t}{T_{1b}}} \quad (\text{continuous}) & \Delta t < t \leq \Delta t + \tau \\ \hline 0 & \Delta t + \tau \leq t \end{cases} \\
r(t) &= \mathrm{e}^{-\frac{f}{\lambda} t} \\
m(t) &= \mathrm{e}^{-\frac{t}{T_{1t}}}
\end{aligned}
\tag{4.2}
$$

It can be shown that these definitions for the kinetic model functions lead to the same model provided by single compartmental theory, in which modified Bloch equations approach is used (Parkes, 2005).

4.2.1 Buxton Model Equations

Using formulations (4.2), explicit expression for the magnetization difference model $\Delta M(t)$ can be obtained by inserting them into Eq. 4.1 and analytically solving the convolution integral (Buxton et al., 1998). The extremely flexible nature of the general kinetic approach allows standard assumptions to be relaxed modifying the expressions of the kinetics functions without altering the structure of the model. Ideally, many physiological effects of the system such as bolus dispersion (Chappell et al., 2013a; Harbe and Lewis, 2004) can be modeled by appropriate definitions of those three functions, although analytical solution is possible only in simple cases. Elsewhere, they must be handled numerically (Okell et al., 2012).

The following notation is used to compress the formulation:

$$\begin{aligned} R_{1t} &= \frac{1}{T_{1t}} \\ R_{1b} &= \frac{1}{T_{1b}} \\ R_{1,app} &= \frac{1}{T_{1t,app}} = R_{1t} + \frac{f}{\lambda} \\ \delta R &= R_{1b} - R_{1,app} \end{aligned} \tag{4.3}$$

PULSED ARTERIAL SPIN LABELING

Recalling Eq. 4.2, kinetic functions expressions for standard model are:

$$c(t) = \begin{cases} 0 & t \leq \Delta t \\ e^{-\frac{t}{T_{1b}}} & \Delta t < t \leq \Delta t + \tau \\ 0 & \Delta t + \tau < t \end{cases} \qquad r(t) = e^{-\frac{f}{\lambda}t} \qquad m(t) = e^{-\frac{t}{T_{1t}}}$$

It is possible to show that the Buxton model for Pulsed ASL data can be written as a unique stepwise function:

$$\Delta M(t) = \begin{cases} 0 & t \leq \Delta t \\ -\frac{2\alpha M_{0b}}{\delta R} f e^{-R_{1b}t} \left(1 - e^{-\delta R(t-\Delta t)}\right) & \Delta t < t \leq \Delta t + \tau \\ -\frac{2\alpha M_{0b}}{\delta R} f e^{-R_{1b}t} e^{\delta R(t-\Delta t)} \left(e^{-\delta R\tau} - 1\right) & \Delta t + \tau \leq t \end{cases} \tag{4.4}$$

Illustration in Fig. 4.2.1 reports a simulation performed with Buxton model adapted to PASL for a typical set of parameters. It is possible to note the effect of each single parameter to the shape of the signal. Moreover, the dependency on perfusion is reflecting more on the amplitude of the signal, which can also be effected by T_1 decay of tissue and of arrival time Δt even if in a minor way. The dependency on Δt is less when the signal is acquired after a while from the labeling phase. The effect of the labeling duration is strongly affecting the signal and hence should be

fixed with appropriate techniques in the acquisition process (see section 3.3).

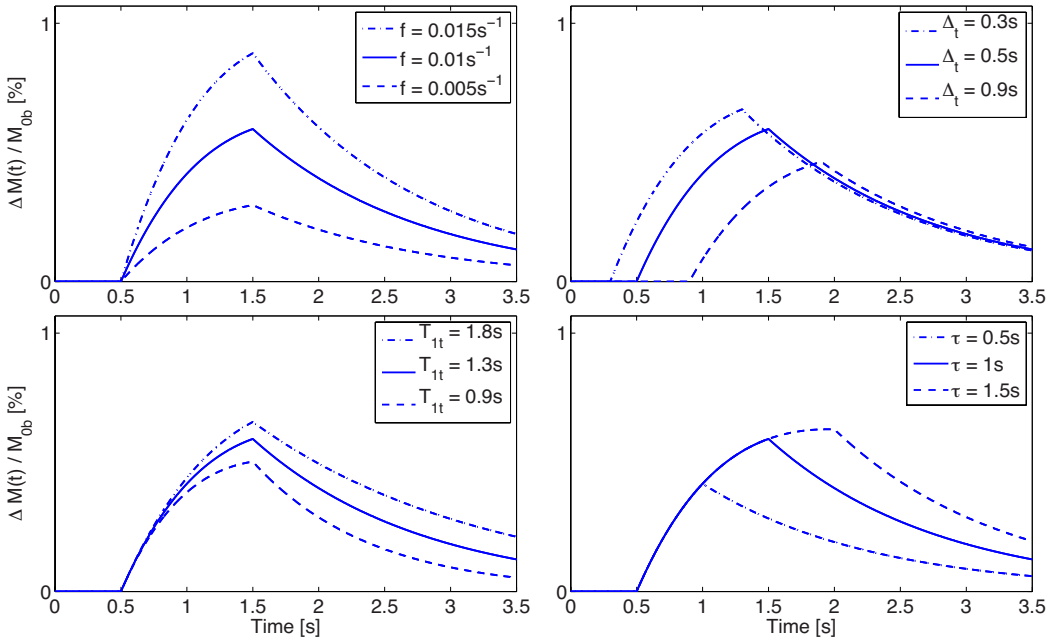

Figure 4.2.1: PASL Buxton model with the following parameters settings: $f = 0.01\frac{mL}{mL\,s}$, $T_{1t} = 1.3s$, $\Delta t = 0.5s$ and $\tau = 1$. In each box, a single parameter is allowed to vary on a grid of values defined in the relative legend. Adapted from Buxton et al. (1998).

Continuous or Pseudo-Continuous Arterial Spin Labeling

To achieve standard model expression with continuous or pseudo continuous labeling scheme, the same strategy shown for pulsed ASL can be used. The unique difference resides in the different description of the delivery function $c(t)$. Using the kinetic model functions (Eq. 4.2), with proper version of arterial magnetization $c(t)$:

$$c(t) = \begin{cases} 0 & t \leq \Delta t \\ e^{-\frac{\Delta t}{T_{1b}}} & \Delta t < t \leq \Delta t + \tau \\ 0 & \Delta t + \tau < t \end{cases} \qquad r(t) = e^{-\frac{f}{\lambda}t} \qquad m(t) = e^{-\frac{t}{T_{1t}}}$$

The Buxton model for Continuous or Pseudo-Continuous ASL data can be written as:

$$\Delta M(t) = \begin{cases} 0 & t \leq \Delta t \\ \frac{2\alpha M_{0b}}{R_{1,app}} f e^{-R_{1b}\Delta t}\left(1 - e^{-R_{1,app}(t-\Delta t)}\right) & \Delta t < t \leq \Delta t + \tau \\ \frac{2\alpha M_{0b}}{R_{1,app}} f e^{-R_{1b}\Delta t} e^{-R_{1,app}(t-\Delta t)}\left(e^{R_{1,app}\tau} - 1\right) & \Delta t + \tau \leq t \end{cases} \tag{4.5}$$

Illustration in Fig. 4.2.2 reports a simulation performed with Buxton model adapted to pseudo-continuous and continuous ASL for a typical set of parameters. As well as for the pulsed case, it is possible to note the effect of each single parameter on the shape of the signal. The same effects of parameters on the signal found in PASL can be observed. However the general signal amplitude is almost doubled, thanks to the prolonged labeling duration and the possibility to fix it in the acquisition process.

4.3 BUXTON MODEL RESTRICTIONS

Buxton model is the result of a series of assumptions condensate in the kinetic functions definition Eq. 4.2. They provide an oversimplified description of blood exchanges within brain tissue, with the severe hypothesis of tissue voxel considered as a single well mixed compartment. A more realistic description of perfusion process should take into account the limited permeability to water of capillary blood (implying that water is not completely extracted during capillary transit), or the fact that tissue\blood exchange of water is not instantaneous but requires to begin at least a time lag after entering the voxel, to allow blood to travel down the vascular tree of the voxel to the capillary bed. Although these improvements, in principle, can be implemented in the frame of general kinetic model by an adequate reshape of kinetics function $r(t)$ and $m(t)$, they have been mostly investigated through the adoption of multi com-

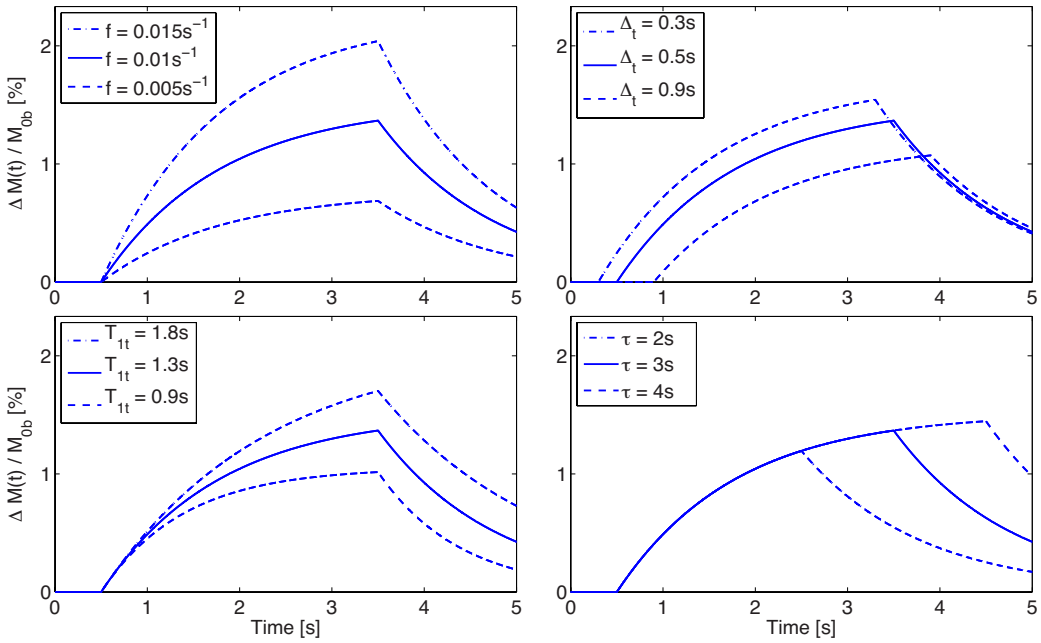

Figure 4.2.2: pCASL/CASL Buxton model with the following parameters settings: $f = 0.01\frac{mL}{mL\,s}$, $T_{1t} = 1.3s$, $\Delta t = 0.5s$ and $\tau = 2$. In each box, a single parameter is allowed to vary on a grid of values defined in the relative legend. Note the higher amplitude of the curve compared to Fig. 4.2.1. Adapted from Buxton et al. (1998).

partmental models (Parkes and Tofts, 2002).

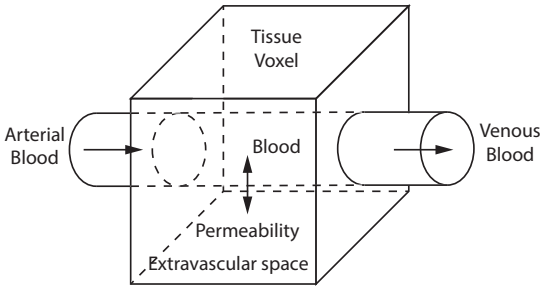

Figure 4.3.1: Schematic diagram of two compartmental model proposed by (Parkes and Tofts, 2002). Water exchanges between blood and extravascular space are described in terms of PS, the permeability (P) surface area (S) product of brain capillaries to water, per volume of tissue. PS published values in whole brain vary from $0.9 - 1.7\ min^{-1}$. In single compartmental (i.e. Buxton model) capillary wall permeability to water is assumed to be infinite.

Assumption regarding the shape of input function $c(t)$, however, can be relaxed without modifying the basic single compartment structure underlying Buxton model, and furthermore without losing the possibility of dealing with analytical expression. In the Buxton model described above, the arrival of tagged blood into the imaged region is assumed sudden and simultaneous (uniform plug flow assumption). This assumption makes leading and trailing wavefront of tagged blood bolus to form sharp-edge step functions, noticeable in the *'rect'* like shape of delivery function $c(t)$. A more realistic approach aims at replacing $c(t)$ with a smoother input function that accounts for the statistical nature of the arrival time. Indeed, tagged blood water molecules proceed to the imaging slice along pathways of varying lengths and at different speeds. This randomness has a consequence of smoothing the edges of $c(t)$. Remembering the definition of delivery function for PASL and pCASL/CASL:

$$c(t) = \mathrm{e}^{-\frac{\Delta t}{T_{1b}}} w(t) \qquad \text{pCASL/CASL}$$
$$c(t) = \mathrm{e}^{-\frac{t}{T_{1b}}} w(t) \qquad \text{PASL}$$

with $w(t)$ defining a typical boxcar shape (function is non null only for

times $\Delta t \leq t \leq \Delta t + \tau$), dispersion effects can be described by taking the convolution of $w(t)$ with the a dispersion kernel $k(t)$, which describing how dissipation occurs (Harbe and Lewis, 2004):

$$c(t) = \mathrm{e}^{-\frac{\Delta t}{T_{1b}}} \left[w(t) \otimes k(t)\right] \qquad \text{pCASL/CASL}$$
$$c(t) = \mathrm{e}^{-\frac{t}{T_{1b}}} \left[w(t) \otimes k(t)\right] \qquad \text{PASL}$$

Analytical solutions were obtained with uniform dissipation kernel and gaussian dissipation kernel (see figure (4.3.2)).

Recently, a gamma kernel shape has been proposed and suggested as the more realistic solution to model dispersion in the quantification process of ASL data (Chappell et al., 2013a). Analytical solution for convolution with gamma kernel is given by:

$$w(t) \otimes k(t) = \begin{cases} 0 & t \leq \Delta t \\ Q\left(s(t-\Delta t), 1+sp\right) & \Delta t \leq t \leq \Delta t + \tau \\ Q\left(s(t-\Delta t), 1+sp\right) - Q\left(s(t-\Delta t-\tau), 1+sp\right) & t \geq \Delta t + \tau \end{cases} \tag{4.6}$$

where $Q(x, y)$ is the incomplete gamma integral defined as $Q(x, y) = \frac{1}{\Gamma(y)} \int_0^x \mathrm{e}^{-u} u^{y-1} du$, and s and p are the parameters of gamma dispersion kernel. However, the corresponding final model prediction $\Delta M(t)$ can not be given in an analytical form.

4.4 Model free and deconvolution technique

In the previous section a review of the most used models and their limitations has been reported. The flexibility of the model is given by the number of assumptions that we have to make to use it. An alternative more flexible framework is to consider a model free approach, which formally does not require any model. It is based on deconvolution. The

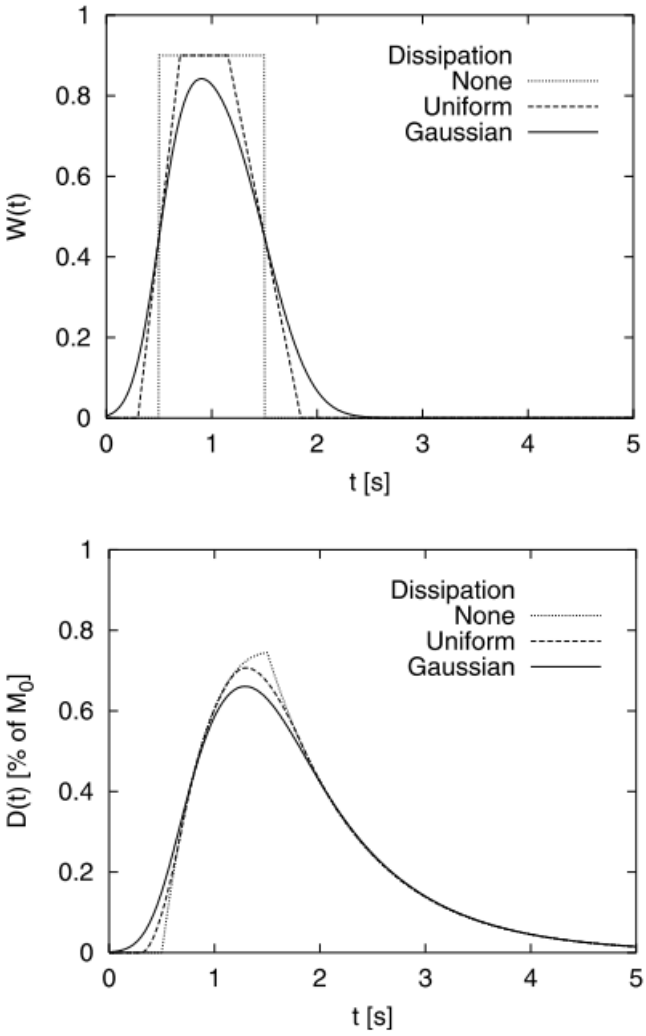

Figure 4.3.2: Effects of the inclusion of input dispersion on $c(t)$ (top panel) and its effect on the PASL model prediction (bottom panel). Smoothing of the input function is shown to affect not only the initial slope but also the maximum obtainable perfusion signal (Taken from Harbe and Lewis (2004)).

deconvolution problem has been largely investigated and applied to another perfusion technique, called Dynamic Susceptibility Contrast (DSC-MRI). The same framework has been adapted to ASL by Petersen et al. (2006). To calculate perfusion with this method the Arterial Input Function (AIF) is required. AIF can be considered the delivery function in Buxton model. The tissue kinetic should be sampled at a high temporal resolution. To cope with these constraints an ad hoc sequence has been developed: Quantitative Star labeling of Arterial Region (QUASAR, see 3.5 where the technical details of the sequence has been reported). The key point is how to retrieve the AIF, it can be done from the combination of two acquisitions. One part of the experiment is carried out using vascular crushing gradients and the other without. If this information can be estimated somehow it is possible to apply a deconvolution operation to the integral in Eq. 4.1 without any information about the bolus width, the spatial variability of the brain partition coefficient and on the number of compartments needed to explain the exchange of the blood in the tissues.

4.4.1 Arterial Input Function

If it would be possible to locate a voxel of full arterial blood, the AIF, considered the longitudinal magnetization of blood and the inversion operation needed to create the bolus, can be written as:

$$AIF(t) = 2 \cdot M_{0b} \cdot c(t) \tag{4.7}$$

A deconvolution operation between the AIF and the tissue will provide information about the response of the system, that can be described by the residue function $r(t)$ multiplied with the relaxation function $m(t)$ and the perfusion:

$$f \cdot R(t) = f \cdot r(t) \cdot m(t) \tag{4.8}$$

$R(t)$ has been defined as the residue function of the system by Petersen et al. (2006) leading to a misunderstanding. The residue function is in-

deed $r(t)$. Hence, it will be referred as the *true residue function* while its combination with the magnetization relaxation function will be referred as the *residue function*. By definition $R(t)$ is positive and decreasing with $R(0) = 1$, therefore the perfusion can be estimated from its maximum without any further assumptions. As already reported in section 3.3.2 and 3.5 in ASL images acquired at early TI it is possible to note bright spots due to voxel containing blood coming not only from tissue contribution but also from the macro vascular component. It is possible also to note that the arrival time in the tissue is quite higher compared to the macro vascular one and this is expected due to the time needed by the blood to reach the micro-vasculature and there exchange with tissues. Theoretically possible to extract the AIF from the difference of the two signals. However the extracted AIF should be scaled accordingly to the volume fraction of the arterial blood volume (aBV). To normalize the AIF accounting for aBV it is necessary to know the bolus width (τ) and M_{0b}. The duration of the bolus has been fixed in the sequence using a Q2TIPS like method. To extract the magnetization of blood it is possible to use the sagittal sinus. To avoid partial volume effect the theoretically calculated AIF should be scaled on a voxel by voxel basis. This can be obtained comparing the area under the curve of the macro vascular component with the one of the theoretical AIF ($2 \cdot M_{0b} \cdot \tau$) and finally taking into account both the labeling efficiency (α) and the Look & Locker readout for the pulses that the blood experienced from its arrival in the artery (Δta) to the effective arrival in the tissue (Δtm)

$$AIF(t) = 2M_{0b}\alpha cos(\alpha_{LL})^{floor\left(\frac{\Delta t_m - \Delta t_a}{\Delta TI}\right)} c(t) \tag{4.9}$$

where

$$c(t) = \tau \cdot \left(\frac{(\Delta M_{uncr}(t) - \Delta M_{cr}(t))\, e^{\frac{1}{T_{1b}}}}{\int_{-\infty}^{+\infty} (\Delta M_{uncr}(t) - \Delta M_{cr}(t))\, e^{\frac{t}{T_{1b}}} dt} \right) e^{-\frac{1+(\Delta t_m - \Delta t_a)}{T_{1b}}} \tag{4.10}$$

Here $\Delta M_{uncr}(t)$ represents the tissue curve obtained without applying

the vascular crushing gradients while $\Delta M_{cr}(t)$ applying them. The difference between the arrival time in the microvascolature and in the arterial side is a direct scaling factor for the perfusion estimates. This has been defined as delay and it will be discussed in section 5.1.1.2. The technique proposed by Petersen et al. (2006) to estimate this delay term is to use an edge detection algorithm (Canny, 1986) to compute the rising edge of both the curves. The aBV can then be extracted as

$$aBV = \frac{\int_{-\infty}^{+\infty} (\Delta M_{uncr}(t) - \Delta M_{cr}(t))\, e^{\frac{t}{T_{1b}}} dt}{2M_{0b}\tau\alpha} \tag{4.11}$$

To be noted that the area of the macro vascular component has been corrected for T_1 decay of blood and the aBV is that area divided by a theoretical AIF extracted in a pure arterial blood voxel. Moreover, the cosine factor has been neglected assuming the hypothesis that the arterial blood is completely renew between two consecutive excitation pulses.

The deconvolution problem in presence of noisy data can be considered as an inverse problem, both ill-posed and malconditioned. This means that, respectively, not only one solution can exist but that also small errors in the measurement data will cause a larger impact on the estimated residue function. Historically the first proposed approach used a singular value decomposition technique (SVD) (Østergaard et al., 1996). later on two evolutions of it were presented: the circular SVD (cSVD) and the block-circulant SVD (oSVD) (Wu et al., 2003). The principal difference between SVD and c/oSVD is that the latter are insensitive to delay between AIF and tissue. This is obviously true for DSC where the magnetization relaxation function could be neglected for the tracer. In case of QUASAR the delay should be evaluated as a scaling factor as Eq. 4.10 suggests. The very appealing characteristic of SVD-based method is that they are very quick and hence they can easily be transported to the clinical environment. However, the regularization introduced in the estimated residue function appears in form of both negative values and oscillations not physiologically interpretable. This leads to a systematic underestimation of perfusion due to the instability of the system described

by SVD methods. Another limitation that has been already addressed regarding perfusion measurement with deconvolution technique regards the dispersion of the bolus that occurs between large arteries down to the capillary bed. Thus, another more powerful method that can overcome this limitation has been proposed. It is called Nonlinear Stochastic Regularization (NSR) and has been previously developed for DSC (Peruzzo et al., 2011; Zanderigo et al., 2009) and then applied to QUASAR data (Ahlgren et al., 2013). The main advantage of NSR is that it could potentially solve the problem of dispersion between AIF and tissues and moreover it can also estimate its level. The major drawback of NSR is due to its heavy computational burden. Indeed, to elaborate a single subject of QUASAR data almost 4 hours are necessary.

4.4.2 SVD-BASED METHODS

SVD approach can be summarized considering the discretized form of the deconvolution problem that can be written as:

$$\Delta M(t_j) = \Delta TI \cdot f \cdot \sum_{i=0}^{j} AIF(t_i) \cdot R(t_j - ti) \quad , i = 0, 2, ..., N-1 \tag{4.12}$$

where N is the number of samples of the ASL kinetic curve. This relation can be written in matrix form:

$$\mathbf{\Delta M} = \Delta TI \cdot f \cdot \mathbf{AIF} \times \mathbf{R} \tag{4.13}$$

where **AIF** is a Toeplitz matrix with first column equal to the AIF(t) and the first row equal to the element $AIF(t_0)$ in the first position and zeros in the others. The vector R is the unknown entity and the inversion of the system can be solved using a raw deconvolution approach or more robustly, using SVD:

$$f \cdot \mathbf{R} \cdot \Delta TI = \mathbf{AIF}^{-1} \times \mathbf{\Delta M} \tag{4.14}$$

$$\mathbf{AIF^{-1}} = \mathbf{V} \cdot \mathbf{W} \cdot \mathbf{U^T} \tag{4.15}$$

where the columns of $\mathbf{U}$ represent the eigenvectors of $\mathbf{AIF}^T\mathbf{AIF}$ and the columns of $\mathbf{V}$ represent the eigenvectors of $\mathbf{AIF}\mathbf{AIF}^T$. The matrix $\mathbf{W}$ is a diagonal matrix where the diagonal values are the eigenvalues of $\mathbf{AIF}^T\mathbf{AIF}$, hence it is possible to retrieve $\mathbf{R}$ and f using SVD:

$$f \cdot \mathbf{R} = \frac{\mathbf{U} \cdot \mathbf{W}^{-1} \cdot \mathbf{\Delta M}}{\Delta TI} \tag{4.16}$$

A threshold is usually set on the eigenvalues located in the diagonal of $\mathbf{W}$; these values can be discarded lowering the rank of the system. Circulant SVD (cSVD) is a version of SVD that can accommodate for delay between AIF and tissue, changing the shape of the AIF. After a padding, a circulant AIF is made augmenting the system dimension in a doubled time grid (Wu et al., 2003).

A third version of SVD-based method (oSVD) has been proposed that attempt to eliminate the unwanted oscillations in the $\mathbf{R}$. P_{SVD} is the threshold value used in the truncation of $\mathbf{W}$ and increasing it will lead to less oscillations. It is possible to start from a minimum acceptable value for the threshold (usually set to 10% of the maximum eigenvalue) and then increasing it until a specific oscillation index is reached:

$$O = \frac{1}{2N}\frac{1}{R_{max}}\left(\sum_{k=2}^{2N-1} |\hat{R}(k) - 2\hat{R}(k-1) + \hat{R}(k-2)|\right) \tag{4.17}$$

where $\hat{R}$ is the estimated residue function and R_{max} is its maximum amplitude. Usually an oscillation index of 0.95 is advisable.

4.4.3 Local Arterial Input Function

The standard pipeline in QUASAR requires the mapping of the AIF calculated as in section 4.4.1. Each tissue curve should be coupled with the best suitable AIF. The standard approach proposed by Petersen et al. (2006) its made up of three steps. The first step consists in a fitting proce-

dure of the local AIF with a gamma variate function:

$$c(t, \Delta t_a, s, p) = \begin{cases} 0 & t < \Delta t_a \\ \tau \frac{s^{1+sp}}{\Gamma(1+sp)} (t - \Delta t_a)^{sp} e^{-s(t-\Delta t_a)} & t \geqslant \Delta t_a \end{cases} \tag{4.18}$$

A goodness of fit criteria is used combined with a threshold of 1.2% of aBV to exclude possible ill-defined AIFs. The euclidean distance is then calculated as a metric of similarity and each tissue voxel is mapped to the nearest AIF voxel. If multiple candidates of AIF are found for the same voxel, the mean of those is retained as a local AIF. The nearer the AIF is to the tissue, the more the dispersion effect can be theoretically avoided.

4.5 Model fit techniques and Bayesian approaches

Among the possible fit techniques the simplest strategy to fit a model to a set of measured data, is to use least squares (LS). In the case of ASL, the magnetization difference model (such as Buxton model), $\Delta M(p)$ will be fit to ASL data (y). Briefly, the optimal set of parameters values when LS approach is used, $\hat{p}^{LS}$, is the one who minimizes a cost function given by the sum of the residuals squares (RSS), where residuals $r(t_k)$ with $k = 1, \ldots, N$, are defined as the differences between data and model predictions. In the context of ASL model, it can be formalized as follows:

$$\hat{p}^{LS} = \underset{p}{argmin} \left[\| \, r(p) \, \|^2 \right] = \underset{p}{argmin} \left[\| \, y - \Delta M(p) \, \|^2 \right] \tag{4.19}$$

where $\hat{p}$ is a vector of unknown parameters. The nonlinear nature of ASL standard model $\Delta M(t, \hat{p})$ precludes the existence of a close-form solution for the minimization problem using LS. In practice, to find $\hat{p}^{LS}$ non linear versions of LS estimator have to be used. Several algorithms can be used for nonlinear optimization, however all of them consist in an iterative scheme in which substantially a linear solution approximation is made at each step. A possible solution to nonlinear least squares (NLLS) optimal parameters can be calculated using MATLAB, and the trust region

reflective optimization algorithm (Coleman and Li, 1996).

A refined version of NLLS estimation could be obtained associating a weight to each data point y_k, so that when computing the RSS each of them will contribute to the total amount in proportion to the amplitude of its weight. This approach is named weighted NLLS approach (WNLLS). The meaning of data weights is to define how reliable is each sample to better address parameters identification. A natural choice for weights is to use the inverse of the measurement noise standard deviation, when it is known. Elsewhere, they must be evaluated somehow, for example using data or knowledge of empirical experiment (Cobelli et al., 2002).

In ASL, data weights to include in a WNLLS estimator can be derived directly from data, taking advantage from the multiple experiment repetitions performed to face with low SNR of the perfusion signal. There are several ways to statistically describe the noise in the data and how this can affect the signal kinetic samples. A common procedure consists in calculating for each voxel the variance over the number of repeated acquisitions for both control and label and summing the two quantities. Another approach could be to infer a statistical description of the noise from the background area of the image. In principle taking a square of sufficient size from the background and calculating the variance in that square can provide a quite good approximation of the noise present in the acquired signal. These two approaches are defined as voxel-wise or region-wise approaches and are both used in literature. If the noise could not be inferred from the data it is possible to estimate it in the fitting procedure. This approach is called relative WNLLS. On the contrary, if the weights are defined and not estimated during the fitting process, the estimator is called absolute WNLLS.

The method chosen gives a definition of the vector $[w_1, w_2, \ldots, w_{N_{LL}}]$ that will be used in the estimation following:

$$\begin{aligned}\hat{p}^{WNNLS} &= \underset{p}{argmin}\left[\sum_{k=1}^{N}\left(w_k r_k(p)\right)^2\right] \\ &= \underset{p}{argmin}\left[\left(y-\Delta M(p)\right)^T W\left(y-\Delta M(p)\right)\right]\end{aligned} \tag{4.20}$$

where W is a diagonal $[N \times N]$ matrix, whose elements are the data weights w_k.

4.5.1 Bayesian inference with ASL data

The traditional model fitting approach, that makes use of WNLLS estimation, experiences some problems when it is applied to ASL data. Model non linearity coupled with low SNR data points could easily lead to local optimum solutions, or to the lack of convergence of non linear estimator. This unwanted behavior, at a fixed SNR level, occurs more likely increasing the number of parameters to be estimated. This implies that with WNLLS estimation particular care must be paid to the number of unknown parameters included in the model. With dynamic data no more than two parameters (f and Δt) are usually estimated. Extracting useful information from data is thus limited by these numerical issues, and as a consequence local parameters, such as T_{1t} (and τ for PASL data), are fixed to a whole brain unique value. When there is no valid reason to fix them (for example with Q2TIPS, τ can be experimentally determined with good robustness), their estimation it inevitably introduces bias in f (and Δt) estimates. In the context of ASL data fitting, a more powerful approach to model inference, such as bayesian approach, can lead to a stronger improvements as concern the capability to obtain more reliable estimates and adds an important information on the precision of each estimate (Chappell et al., 2009).

In the basic bayesian inference problem there is a series of measurements y that are to be used to determine the parameters p of a chosen model $\mathcal{M}$. The gain, beside least squares estimation, is that information

on parameters (or some of them), ideally independent from experimental measurements, is available somehow, and can be exploited to improve parameters estimation. The method is based on Bayes theorem:

$$P(p \mid y, \mathcal{M}) = \frac{P(y, p \mid \mathcal{M})}{P(y \mid \mathcal{M})} = \frac{P(y \mid p, \mathcal{M})P(p \mid \mathcal{M})}{P(y \mid \mathcal{M})}$$

which gives the posterior probability of the parameters given data and model, $P(p \mid y, \mathcal{M})$, in terms of: the likelihood of the data given the model and its parameters p, $P(y \mid p, \mathcal{M})$, the prior probability of the parameters for the model, $P(p \mid \mathcal{M})$, and the evidence for the measurements given the chosen model, $P(y \mid \mathcal{M})$:

$$P(p \mid y) = \frac{P(y \mid p)P(p)}{P(y)} \tag{4.21}$$

where measured data y are formed by signal difference ΔM, and where the dependance upon the model used is implicitly assumed.

As previously noted, the key advantage of the bayesian approach is that a priori information about the parameters based on physiological or physics knowledge can be incorporated in the estimation procedure.

Parameters estimation in a bayesian framework can be obtained also without the need to evaluate the entire posterior probability distribution, which is a high computationally demanding step. Numerical methods as variational Bayes (see section 4.5.2) and Markov Chain Monte Carlo, have to be employed since analytical forms for the posterior are admitted only in few simple cases. Bayesian inference can be accomplished simply extracting from $P(p \mid \Delta)$ punctual estimates and their (approximated) variance. When this kind of approach is performed, the terms that do not depend on the parameters in Eq.4.21 can be discarded, that is, the normalization factor provided by the evidence term $P(\Delta)$ can be ignored, yielding:

$$P(p \mid y) \propto P(y \mid p)P(p) \tag{4.22}$$

$P(y \mid p)$ is calculated from the model; in particular it depends on the sta-

tistical description of noise vector v, and $P(p)$ incorporates prior knowledge of the parameter values and their variability.

A number of punctual estimators can be obtained from Eq. 4.22, such as minimum variance (MV) estimator, and maximum a posteriori (MAP) estimator. Adopting MAP estimator, the primary interest is on the location of the maximum of the posterior probability, i.e. parameters estimated values are those which maximize the posterior probability distribution $P(p \mid y)$. Maximum a posteriori estimator is mathematically expressed by:

$$\hat{p}^{MAP} = \underset{p}{argmax}\,[P(p \mid y)] = \underset{p}{argmax}\,[P(y \mid p)P(p)] \tag{4.23}$$

A straightforward interpretation of Eq. 4.23 is to view p^{MAP} rendered by MAP estimator as maximum likelihood estimates balanced by the a priori information, condensed in the prior probability term $P(p)$.

4.5.2 Variational Bayes Approach

The use of a Bayesian framework to introduce a priori information helping in reducing the variability of the estimates of physiological parameters has been already introduced and applied to ASL. This brief section will describe the key assumptions of the Variational Bayes (VB) approach and it is based on the work by Chappell et al. (2009), where a fast method to estimate the posterior distribution in case of nonlinear forward model is introduced. Using VB it is possible to numerically evaluate the posterior distribution, since for many cases it is not possible to assess a close analytical form for it. A simple idea is to parametrize the posterior with a set of *hyper parameters*. The measure of the posterior goodness is achieved with the calculation of the Free Energy (FE):

$$FE = \int q(p) log \left[\frac{P(y \mid p)P(p)}{P(y)}\right] \tag{4.24}$$

The integral is tractable only if a good choice on the shape of q is per-

formed. Hence, VB uses mean fuel approximation of $q(p)$:

$$q(w) = \prod_i q_{p_i}(p_i) \tag{4.25}$$

here the parameters are separated into groups, each of them with a posterior distribution $q(w_i)$. The important note here is that VB considers each of these groups independent from the others. Maximizing $q(w_i)$ over FE and applying the calculus of variation:

$$log q_{p_i}(p_i) \propto \int q_{p_{\not i}} log P(p \mid w_{\not i}) P(p) dp_{\not i} \tag{4.26}$$

where $p_{\not i}$ represents a parameter not included in the *i-th* group. The next step is to restrict the priors to only the ones that are conjugated with the complete likelihood of the data:

$$q_{p_i}(p_i) \propto P(y \mid p_i) P(p_i) \tag{4.27}$$

This means that the posterior should be parametrized in the same form as the prior. This restriction is not limiting, since the family of available prior is quite broad, whit uninformative prior as a limit case. Moreover, the calculation of the hyper parameters can be done in an iterative process that follow an Expectation Maximization (EM) scheme. Indeed, it has been proved that VB is a general formulation for the EM algorithm. Thus, the algorithm is iterative, but its convergence is guaranteed.

Just because something doesn't do what you planned it to do doesn't mean it's useless.

Thomas A. Edison

5

Novel quantification methods for QUASAR data

The quantification of perfusion with QUASAR data has been proposed by Petersen et al. (2006). This sequence has been reviewed from the physical point of view in section 3.5. Moreover, the methodology used in the standard pipeline of analysis has been introduced in section 4.4. In particular, the deconvolution algorithm class, based on SVD, has been reviewed. These methods are known to introduce both underestimation in perfusion estimates and physiologically not interpretable oscillations in the residue function. Thus a new algorithm based on a kernel based approach, Stable Spline (SS), built in a Bayesian framework, has been developed and tested in this thesis. Its evaluation has been performed on both simulated and real data. The assessment of its performances has been addressed computing the bias in perfusion estimates and evaluating its reliability to estimate a smooth and physiological residue function. Re-

cently a model-based approach, based on a Variational Bayes (VB) framework has been introduced as a further method to analyze QUASAR data (Chappell et al., 2013b). The performances of SS will be also compared to this framework. Moreover, an improved version of model originally implemented in the VB framework will be proposed and added to the comparison. The quantification methods are compared not only on the basis of giving a plausible range of perfusion estimates in GM and WM but also in the spatial variability of those estimates. Eventually, other parameters, such as the arrival time, will be evaluated. For the sake of the comprehension, a brief theory section on the SS method and on the improved model are presented at the beginning.

5.1 Deconvolution approach: Stable Spline

5.1.1 Theory

SS is a kernel method that allows the estimation within a Bayesian framework of smooth and physiologically interpretable residue functions ($R(t)$) without the necessity to constrain its behavior to have a fixed model. SS allows the estimation of the $R(t)$ function, i.e. the multiplication of $r(t)$ and the magnetization relaxation term $m(t)$ (see section 4.4). $R(t)$ is modeled by the sum of two components (a deterministic term ($r_d(t)$) and a stochastic one ($r_s(t)$).

$$R(t) = r(t) \cdot m(t) = r_d(t) + r_s(t) \tag{5.1}$$

$r_s(t)$, is modeled as a zero-mean Gaussian random process with auto-covariance $cov(r_s(t_1), r_s(t_2)) = \phi^2 K(t1, t2)$where ϕ is a parameter to be estimated in the optimization. K is the kernel of the Reproducing Kernel Hilbert Space. The auto-covariance function can include prior information on the smoothness of the tissue impulse response and was modeled

as an integrated Wiener process with 0 as initial condition:

$$W(t_1, t_2) = cov\left(r_s(t_1), r_s(t_2)\right) = \phi \begin{cases} \frac{t_1^2}{2}\left(t_2 - \frac{t_1}{3}\right) & t_1 \leqslant t_2 \\ \frac{t_2^2}{2}\left(t_1 - \frac{t_2}{3}\right) & t_1 > t_2 \end{cases} \tag{5.2}$$

In this formulation the kernel can correctly identify only straight-line impulse responses. Biological systems, included ASL data, are usually described by exponential impulse responses. Moreover, the variance of the process associated with the stochastic component (Eq. 5.1) increases with time, while biological systems are usually stable (i.e. the uncertainty of the impulse response decreases with time). This limitation was overcome here: the auto-covariance $W(t_1, t_2)$ of $r_s(t)$ was formulated to take into account this behavior. First of all, a time transformation $\tau = e^{-\beta t}$ (with $\beta > 0$) was applied. Secondly, $r_s(t)$ was modeled as a Wiener process with 0 as initial condition in the new domain, giving :

$$cov\left(r_s(t_1), r_s(t_2)\right) = \phi^2 W(e^{-\beta t_1}, e^{-\beta t_2}; \beta) t_1, t_2 \geqslant 0 \tag{5.3}$$

This formulation allows to describe systems in which the Bounded Input Bounded Output (BIBO) stability of the impulse response is guaranteed. In Fig. 5.1.1 it is possible to note the imposition of the BIBO stability of the system.

$r_s(t)$ contains the prior information on smoothness and stability associated with the tissue impulse response. When this latter is not well described by the prior, then the deterministic component $r_d(t)$ helps the estimator. The model chosen for $r_d(t)$ was an exponential function with two unknown parameters $[\theta, \beta]$:

$$r_d(t) = \theta e^{(-\beta t)} \tag{5.4}$$

The parameters estimation is cast as a Tikhonov problem and can give

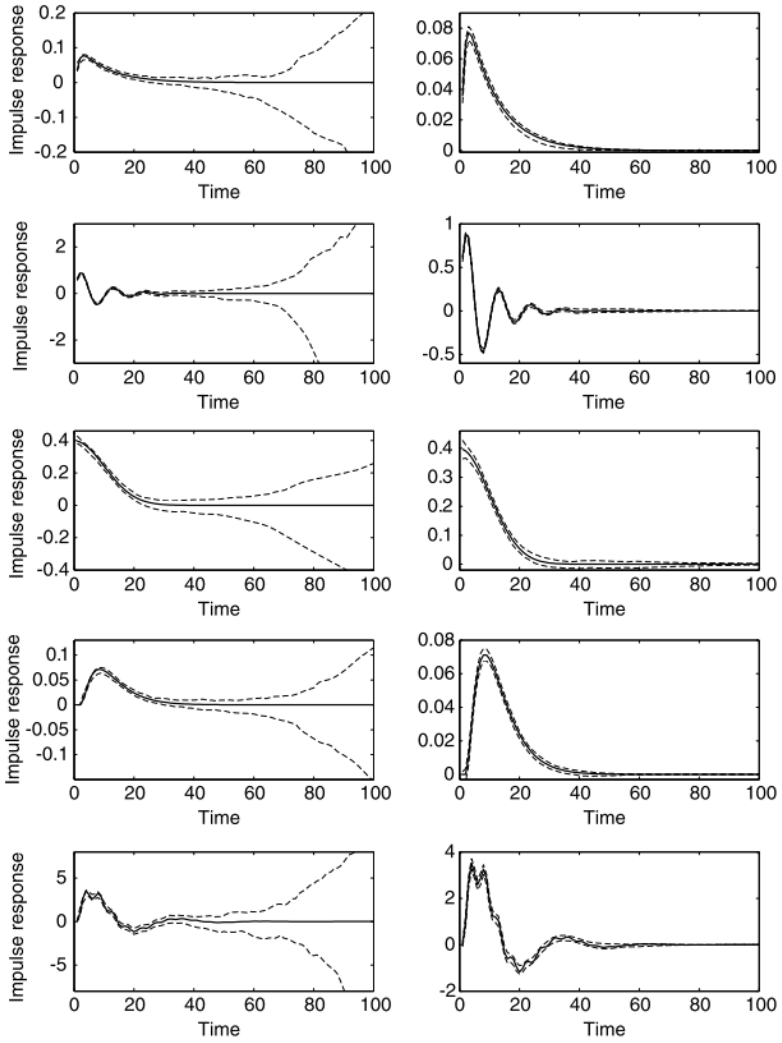

Figure 5.1.1: Results from Monte Carlo simulation using white noise as system input: true impulse response (solid line) and 99% variability bands of the estimates (dashed lines) obtained modeling the unknown function using the classic cubic kernel W (left) and the stable spline kernel K (right) where the BIBO stability of the system is guaranteed. Taken from Pillonetto and De Nicolao (2010)

the minimum variance estimate of R(t):

$$\hat{R} = \underset{R}{\operatorname{argmin}} \sum_{i=1}^{N} \left(\Delta M_i - L_i^{AIF}[R]\right)^2 + \frac{\sigma^2}{\phi^2} P[R]\|_H^2 \tag{5.5}$$

where $P[R]$ is the projection of the impulse response onto the Hilbert space (H) associated to the Kernel K and $\|\|_H$ is the norm of the Hilbert space. The estimation of R(t) can be split into two steps. Following the empirical Bayesian approach, the model parameters $p = [\beta, \phi, \sigma]$ are obtained by maximizing the marginal likelihood , i.e. maximizing the probability of the data given the residue function parameters, which can be computed following (Pillonetto and De Nicolao, 2010) :

$$\begin{aligned} \hat{p} &= \underset{p}{\operatorname{argmin}} J\left(c, p\right) \\ \hat{\theta} &= \frac{D(\hat{p})^T M(\hat{p})^- 1c}{D(\hat{p})^T M(\hat{p})^- 1D(\hat{p})} \end{aligned} \tag{5.6}$$

where

$$J(c,p) = \frac{1}{2} b(p) + \frac{1}{2} c^T A(p) c \tag{5.7}$$

$$b(p) = ln(det(M)) + ln(D^T M^- 1D) \tag{5.8}$$

$$A(p) = M^- 1 \left(I_N - D\left(D^T M^{-1} D\right)^- 1 D^T M^{-1}\right) \tag{5.9}$$

$$D(p) = \left[L_i^{AIF}[r_d], ..., L_N^{AIF}[r_d]\right]^T \tag{5.10}$$

$$M(p) = Var[c|\theta, p]^T \tag{5.11}$$

where the (i, j) element of M is defined from

$$M(p)_{i,j} = \lambda^2 L_i^{AIF} L_j^{AIF}\left[K(\cdot, \cdot; p)\right] + \sigma^2 \delta_{ij} \tag{5.12}$$

where δ is the Dirac function. θ is completely determined by p; thus, the optimization of the marginal likelihood can be performed only on three parameters (first step). Once this has been completed the minimum variance estimate of the residue function solving Eq. 5.5 can be directly

computed (no optimization is required for this second step):

$$\hat{R}(t) = \hat{\theta} e^{(-\beta ? t)} + \hat{\phi}^2 \sum_{i=1}^{N} v_i L_i^{AIF} \left[K(\cdot, \cdot; \hat{\beta}) \right] \tag{5.13}$$

where the scalars v_i are the elements of the vector obtained from:

$$v = (Var[c|\theta], \hat{p})^{-T} \left(\Delta M - \left[L_i^{AIF}[\hat{R}], ..., L_N^{AIF}[\hat{R}] \right]^T \hat{\theta} \right) \tag{5.14}$$

For a more complete description of the SS method and the proof of the formulas reported here see the original paper of the method (Pillonetto and De Nicolao, 2010). In summary, SS is a kernel method that casts the deconvolution problem as an optimization problem in an infinite dimensional functional space given by a Reproducing Kernel Hilbert Space (RKHS). In such environment, the system impulse response (i.e. the residue function in the ASL QUASAR problem) is described as a zero-mean Gaussian process whose covariance incorporates the prior knowledge. Prior knowledge can include smoothness, positivity or system stability constraints. Process covariance specifies also the kernel of the RKHS, which contains some unknown parameters that have to be estimated from the data. The choice of the kernel is therefore critical and can be seen as the choice of the model-class in a parametric approach.

5.1.1.1 Constrained Stable Spline

SS is very flexible since it can include constraints to the estimated $R(t)$. After the first step (parameter vector p has been already computed), it is possible to modify the formulation of the deterministic component and therefore include constraints on the final estimate of $R(t)$. $r_d(t)$ is fully determined for less than a factor scale parameter θ that is dependent on p. The whole second step can thus be reformulated as:

$$\mathbf{x} = [\theta, r_s^T] = [\theta, r_s(t_0), r_s(t_1), ..., r_s(t_{N-1})]^T \tag{5.15}$$

$$\mathbf{r}_{d0} = [e^{-\theta t_0}, e^{-\theta t_1}, ..., e^{-\theta t_{N-1}}]^T \tag{5.16}$$

$$\mathbf{G} = [r_{d0} I_{N\times N}] \tag{5.17}$$

$$\hat{\mathbf{R}}(\mathbf{t}) = G\hat{x} \tag{5.18}$$

where $\mathbf{r}d_0$ is the component r_d of the complete impulse response, which is fixed given the parameters $p = [\beta, \phi, \gamma]$; G can be used to estimate the complete $R(t)$ from x by a simple matrix product. The system matrix can be rewritten to incorporate the estimates of the first step:

$$\mathbf{C} = [\mathbf{AIF} \cdot \mathbf{r}_{d0}\mathbf{AIF}] = \begin{bmatrix} y_{d0}(t_0) & AIF(t_0) & 0 & \cdots & 0 \\ y_{d0}(t_1) & AIF(t_1) & AIF(t_0) & \ddots & \vdots \\ \vdots & \vdots & \vdots & \ddots & 0 \\ y_{d0}(t_{N-1}) & AIF(t_{N-1}) & AIF(t_{N-2}) & \cdots & AIF(t_0) \end{bmatrix} \tag{5.19}$$

where $\mathbf{y}_{d0}$ represents the portion of the data y explained by the deterministic component with p fixed estimated in the first step. To compute the norm of the projection of $R(t)$ on H the matrix W can be used:

$$\mathbf{W} = \begin{bmatrix} 0 & 0 \\ 0 & \mathbf{K}^{-1} \end{bmatrix} \tag{5.20}$$

Using the new notation the problem cast in Eq. 5.5 becomes:

$$\hat{\mathbf{x}} = \underset{\mathbf{x}}{\operatorname{argmin}} (y - \mathbf{C}\mathbf{x})^T \Sigma_0^{-1} (y - \mathbf{C}\mathbf{x}) + \frac{\sigma^2}{\phi^2}\mathbf{x}^\mathbf{T}\mathbf{W}\mathbf{x} \tag{5.21}$$

Using Eq. 5.18 the final estimation of $R(t)$ can be achieved. The problem can be reformulated as a quadratic problem in x:

$$\hat{\mathbf{x}} = \underset{\mathbf{x}}{\operatorname{argmin}} \mathbf{x}^T \left(\mathbf{C}^\mathbf{T}\Sigma_0^{-1}\mathbf{C} + \frac{\sigma^2}{\phi^2}\mathbf{W} \right) \mathbf{x} - 2\mathbf{y}^T\Sigma_0^{-1}\mathbf{C}\mathbf{x} \tag{5.22}$$

Many strategies can be employed to minimize a quadratic problem as

the one in Eq. 5.22. Among them, one that can introduce constraints on $R(t)$ estimates has been applied. Nevertheless, this formulation is intrinsically instable, since $\mathbf{K}$ is almost always singular. To exceed this numerical problem due to the inversion of $\mathbf{K}$, a change of coordinates has been proposed:

$$\mathbf{z} = \mathbf{U}^{-1}\mathbf{x} \tag{5.23}$$

with

$$\mathbf{U}^{-1} = \begin{bmatrix} 1 & 0 \\ 0 & \mathbf{K}^{-1} \end{bmatrix} = \begin{bmatrix} 1 & 0 \\ 0 & \mathbf{K} \end{bmatrix} \tag{5.24}$$

and combining it with $\mathbf{W}$ it is possible to perform the change of coordinates using:

$$\mathbf{WU} = \begin{bmatrix} 0 & 0 \\ 0 & \mathbf{K}^{-1} \end{bmatrix} \times \begin{bmatrix} 1 & 0 \\ 0 & \mathbf{K} \end{bmatrix} = \begin{bmatrix} 0 & 0 \\ 0 & \mathbf{I} \end{bmatrix} \tag{5.25}$$

Hence, the problem in Eq. 5.21, using the new coordinates, can be written as:

$$\hat{\mathbf{z}} = \underset{\mathbf{z}}{\operatorname{argmin}} \mathbf{z}^T \left(\mathbf{U}^T\mathbf{C}^T\Sigma_0^{-1}\mathbf{CU} + \frac{\sigma^2}{\phi^2}\mathbf{U}^T\mathbf{WU} \right) \mathbf{z} - 2\mathbf{y}^T\Sigma_0^{-1}\mathbf{CUz} \tag{5.26}$$

The change of coordinates permits to compute z without directly inverting K, gives robustness to the optimization and allows to include the following constraints on $R(t)$:

- **Positivity constraint**:

$$\begin{gathered} \mathbf{Dz} \leqslant \mathbf{b} \\ \mathbf{D} = \mathbf{D}_0\mathbf{U} = [-\mathbf{r}_{d0} - I_{N\times N}]\mathbf{U} \\ \mathbf{b} = [0, 0, \ldots, 0]^T \end{gathered} \tag{5.27}$$

- **Decreasing and positivity constraints**:

$$\begin{gathered}\mathbf{Fz} \leqslant \mathbf{b} \\ \mathbf{F} = \mathbf{F}_0\mathbf{GU} \\ \mathbf{F}_0 = \begin{bmatrix} -1 & 0 & \cdots & \cdots & 0 \\ 1 & -1 & \ddots & \ddots & \vdots \\ 0 & 1 & \ddots & \ddots & \vdots \\ \vdots & \ddots & \ddots & \ddots & 0 \\ 0 & \cdots & 0 & 1 & -1 \end{bmatrix} \\ \mathbf{b} = [0, 0, \ldots, 0]^T \end{gathered} \tag{5.28}$$

5.1.1.2 Delay Sensitivity

In this original formulation the SS algorithm is not designed to handle the problem of delay between AIF and tissue curve. The delay impacts directly the calculation of perfusion estimates. Indeed, the AIF should be corrected for T_{1b} relaxation effects and moreover the tracer will experience multiple RF pulses during the Look & Locker readout that produce a degradation related to the flip angle used (see section 3.4.2.1). If the delay is not well compensated it is possible to introduce a bias in f estimates. Combining the possible systematic errors introduced by both T_1 relaxation effects and readout it is possible to see how an error corresponding to a ΔTI can introduce a bias of 50% in the estimates. In Fig. 5.1.2 the bias is plotted in function of delay error. In the calculation the settings of the implemented QUASAR sequence were used, (ΔTI interval $300ms$ and flip angle is $35°$).

As explained in the theoretical section, SS is a two steps procedure. The first step will compute hyper-parameters of the stochastic component. Adding the delay as a further parameter it is possible to estimate it in a Bayesian framework. Since the deconvolution problem is highly not convex it is difficult to estimate the delay without a good initial guess used as a starting initialization for SS.

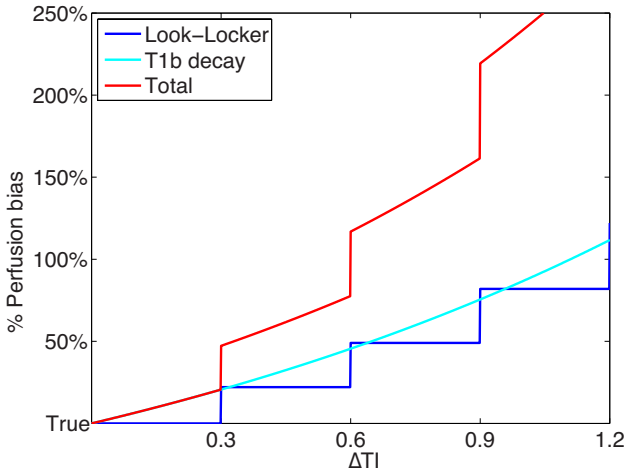

Figure 5.1.2: The bias on perfusion is plotted versus the error in delay assessment in a QUASAR experiment. A double effect is responsible for perfusion estimation errors, since the delay scale the T_{1b} and reflects the number of RF pulses employed using a Look & Locker readout.

The estimation of the starting point was achieved according to the following scheme (Fig. 5.1.3). A wavelet transform (Haar, 3 levels) is applied to the crushed data signal (tissue signal) and the last approximation of the third wavelet level is considered as a smooth approximation of the tissue signal (blue line). Secondly, the cross-correlation between the smoothed tissue curve previously computed and the AIF not corrected for delay (AIF_0) was calculated. Thirdly, the maximum of the cross-correlation function is used to align the peaks of the two curves obtaining a shifted version of the AIF (AIF_{cc}, green dashed line). Finally, an initial guess of the delay has been calculated, computing the distance between the maximum of the curves and the 5% of the maximum for both AIF and tissue signal. This distance can represent the time needed to reach the peak level and hence the differences between the two computed distances can be considered as a good initial guess for delay estimation.

The initial guess for estimated delay is then used as a further parameter in $r_s(t)$ estimation. A new implementation of the first step of SS has therefore been developed. The number of hyperparameters was in-

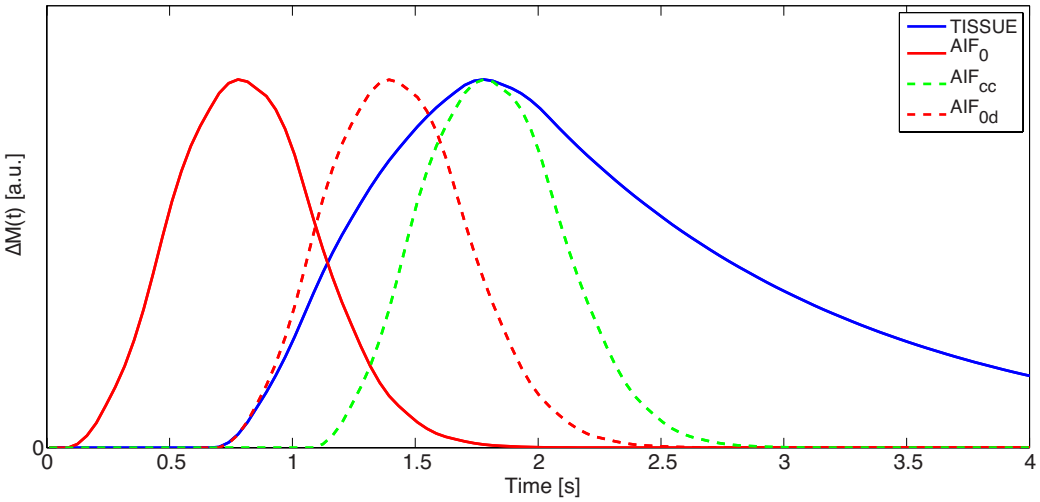

Figure 5.1.3: Initial guess estimation for delay assessment: The third level wavelet approximation is considered as a smoothed version of the tissue signal (blue line). Then the maximum of the cross-correlation between the smoothed tissue curve and the AIF not corrected for delay (AIF_0) is used to align the peaks of the two curves obtaining a shifted version of the AIF (AIF_{cc}, green dashed line). Finally, an initial guess of the delay has been calculated, computing the distance between the maximum of the curves and the 5% of the maximum for both AIF and tissue signal.

creased to include also the delay, $p = [\beta, \phi, \sigma, \delta t]$. The marginalization has not been changed and the whole framework used is still valid. The shifting procedure of the AIF was done inside the minimization of J (Eq. 5.8). This operation has beed done on the parametrized AIF, fitted from the data difference between crushed and uncrushed signal. Maximizing the marginal likelihood with the new parameter adds the possibility to translate the AIF accounting for delay and allows its estimation. Afterwards, the best solution found in the first modified step was used for the constrained estimation of $r_d(t)$ and then of $R(t)$. A constrained version of SS was employed to retrieve smooth, regular, positive and decreasing $R(t)$.

5.2 Model-based approach: estimation of flow speed

Recently a model-based approach, based on a Variational Bayes (VB) framework has been introduced as a further method to analyze QUASAR data (Chappell et al., 2013b). In particular a full model has been introduced to take into account the different direction of vascular gradients employed during the different phases of acquisition. The QUASAR sequence, when vascular crushing gradients are applied, contains a number of phases in an attempt to remove the macrovascular component. Each phase applies flow suppression in a single direction and four different phases are used to achieve a net suppression of flow in any direction (See Table 5.2.1). However, the use of single direction flow suppression will result in some residual macrovascular signal. To maximize the use of information and account for residual macrovascular signal, a model for the QUASAR data was derived that accounted for the various cycles of flow suppression (Chappell et al., 2013b).

The original version of this model used a simple relation to describe the alignment of blood velocity vector with gradients. Thus the relationship between the theoretical tissue signal $\Delta M_t(t)$ summed to the portion of the macro vascular signal modulated by a coefficient $S_c(\mathbf{a}, \mathbf{s})$ describes

Phase	Crushing direction	s
1	$+x, +y, +z$	$(1/\sqrt{3}, 1/\sqrt{3}, 1/\sqrt{3})^T$
2	$-x, +y, +z$	$(-1/\sqrt{3}, 1/\sqrt{3}, 1/\sqrt{3})^T$
3	$+x, -y, +z$	$(1/\sqrt{3}, -1/\sqrt{3}, 1/\sqrt{3})^T$
4	$-x, -y, +z$	$(-1/\sqrt{3}, -1/\sqrt{3}, 1/\sqrt{3})^T$

Table 5.2.1: Different directions adopted to crush the macro vascular signal during the phases of a QUASAR sequence.

the action of the vascular gradients applied during the *c-th* phase:

$$\Delta M_c(t) = \Delta M_t(t) + S_c(\mathbf{a}, \mathbf{s}) \Delta M_a(t) \tag{5.29}$$

where

$$S_c(\mathbf{a}, \mathbf{s}) = 1 - max(\mathbf{a} \cdot \mathbf{s}, 0) \tag{5.30}$$

and the unit vector $\mathbf{a}$ and $\mathbf{s}$ represents the blood flow and the crusher gradient direction. To model the unit vector flow direction were used two angles in polar coordinates:

$$\mathbf{a} = (sin(\phi)cos(\theta), sin(\phi)cos(\theta), cos(\phi))^T \tag{5.31}$$

In this section a more realistic relationship between the crushing gradients and the blood flow is introduced based on the real effect of the crushing on the magnetization of flowing spins (Ahn et al., 1987; Frank et al., 2008; Schepers et al., 2003). The theory of magnetization relationship between flow and bipolar crushing gradients has been already introduced in section 3.3.2. The new model describes the crushing effect using the projection of the average velocity vector along the vascular crushing gradient direction and integrating over the range of velocities in the artery. Following the work of Frank et al. (2008), a gradient pulse produces a velocity dependent total magnetization proportional to both static and flowing spins. Considering only the flowing spins and integrating over a laminar flow profile (flow in brain arteries can be reasonable described by a parabolic profile), the total magnetization in a voxel containing both

macro and micro vascular components can be written as:

$$\Delta M_c(t) = \Delta M_t(t) + Sinc(2\beta\bar{\mathbf{v}}_g)\Delta M_a(t) \tag{5.32}$$

where $\bar{\mathbf{v}}_g = \bar{\mathbf{v}} \cdot \mathbf{g}$ represents the projection of the mean velocity vector on the gradient direction and $\beta = \gamma G \Delta\delta$ (see section 3.3.2). Thus the new model parametrization is:

$$S_c(\mathbf{a}, \mathbf{s}) = Sinc\left(2\beta\bar{\mathbf{v}}_g \cdot max(\mathbf{a} \cdot \mathbf{s}, 0)\right) \tag{5.33}$$

This formulation allows to better describe the macro vascular component and to extract a new parameter, named Arterial Blood Speed (ABS), correspondent to the mean velocity of the blood. This definition can be applied to voxels where the macro vascular component is prominent. The new proposed model will be referred as the Sinc model in the following sections. The estimates in perfusion have been compared with both pre existent model-free and model-based approaches (Chappell et al., 2013a; Petersen et al., 2006) and with the novel Stable Spline method proposed.

The new description for the crusher gradients has been encapsulated in the already proposed full model (Chappell et al., 2013b). This latter comprises the description of a two components model that are estimated simultaneously. It follows the kinetic model proposed by Buxton in a VB approach :

$$\begin{aligned} \Delta M_t(t) &= 2\alpha M_{0b} f\left(c(t) \otimes r(t) \cdot m(t)\right) \\ \Delta M_a(t) &= 2\alpha M_{0b} f\left(aBV \cdot c(t)\right) \end{aligned} \tag{5.34}$$

where $c(t)$, $r(t)$ and $m(t)$ represents the same equations used in Buxton model (Eq. 4.2) for Pulsed ASL. Dispersion effects can be taken into account with this model, adding a dispersion kernel to $c(t)$ (see Eq. 4.6). The same model in order to fit the AIF used in deconvolution techniques has been employed (Chappell et al., 2013a).

5.2.1 SIMULATION

To test the Stable Spline algorithm against existing deconvolution algorithms a set of insilico data was created. The simulation was built following the Buxton model for PASL acquisitions (Eq. 4.2). In Tab. 5.2.2 are reported the parameters used in the simulation. The readout of the QUASAR sequence is accounted modifying the magnetization relaxation function accordingly to Eq. 3.22. The discretization of the ASL signal has been achieved using the same sampling grid that is used in real data to better suite the description of the kinetic curve acquired with QUASAR (equi-spaced from $40\ ms$ to $3940ms$, with ΔTI of $300\ ms$). Synthetic ASL QUASAR data have been generated assuming 3 different levels of perfusion, representing three different situations in the brain (GM 50, WM 20, hyperperfusion 90 ml/100gr/min) and 4 possible delays (0, 0.3, 0.6, 0.9 s). The residue function is assumed to be described by a mono exponential and dispersion effects have been addressed using a dispersed exponential with level of dispersion θ set to three different values (0.05, 0.1, 0.5) correspondent to low, medium and high level of dispersion.

$$d(t) = \frac{1}{\theta} e^{-\frac{t}{\theta}} \tag{5.35}$$

If dispersion is accounted for in simulation Eq. 4.1 becomes:

$$\Delta M(t) = 2M_{0b} f c(t) \otimes [d(t) \otimes r(t) \cdot m(t)] \tag{5.36}$$

For each set of parameters a Monte Carlo simulation with 100 realizations of noise has been performed. Noise level is set to achieve an SNR of 5, 10 and 20. The SNR is described as the maximum of the simulated tissue signal obtained for a voxel of pure GM according to Günther et al. (2001).

$$SNR = \frac{\Delta M_{GM}(t)}{\sigma_N} \tag{5.37}$$

where ΔM_{GM} is the simulated signal obtained for a perfusion level in GM and σ_N is the standard deviation of the noise added to the noiseless

simulated ASL kinetic. The noise is assumed to be white, with zero mean and variance σ_N^2. As discussed in section 4.4.3, in QUASAR usually the AIF is extracted locally to better cope with dispersion effects. To take into account this aspect, the AIF model used for the simulation assumed a gamma dispersion kernel (Chappell et al., 2013a) (see Eq. 4.6).

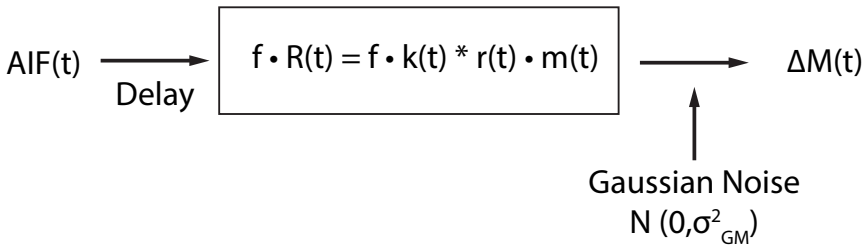

Figure 5.2.1: The illustration reports a scheme that shows how the QUASAR data have been simulated. $AIF(t)$ is modeled by a gamma dispersion kernel (Chappell et al., 2013a). $R(t)$ is modeled as a mono compartmental model and dispersion $d(t)$, modeled as a dispersed exponential has been added to it. Delay has been introduced shifting the $AIF(t)$. Noise level is regulated by GM tissue and the SNR correspondent is modeled by $SNR = max(\Delta M_{GM}/\sigma_N^2)$. Fixed values used for other parameters and range of parameters that varie in the simulation are reported in Tab. 5.2.2.

A subset of simulated signal can be seen in Fig. 5.2.2. SS results obtained using the synthetic datasets have been compared with estimates obtained on the same datasets with the cSVD and oSVD algorithms combined with Edge Detection (ED) (Chappell et al., 2013b; Petersen et al., 2006) (In the following figures the labels cSVD and oSVD will indicate the combination of cSVD and oSVD deconvolution algorithms with ED). The root mean square percentage error ($RMSPE$) of the peak of $R(t)$ ($RMSPE_p$) is computed between the true simulated value and cSVD, oSVD and SS estimates, in order to evaluate the bias on perfusion estimation. To assess the best approximation of the true $R(t)$, the $RMSPE$ of the residue function estimated curve ($RMSPE_c$) has been calculated. For this index, to not penalize SVD-based algorithms that do not shift the AIF, the interval considered for the computation of this index has been

Parameter	Range of simulated value	Unit
f	50 (GM), 20 (WM), Hyper (90)	$\frac{mL}{100g\,min}$
δt	0,0.3,0.6,0.9	s
SNR	5,10,20	a.u.
θ	0.05, 0.1, 1	a.u.
Δt_a	0.5	s
Δt_m	$\Delta t_a + \delta t$	s
τ	0.64	s
s	5	a.u.
p	0.01	s
T_{1t}	1.3 (GM), 0.83 (WM)	s
T_{1b}	1.65	s
α	1	a.u.
M_{0t}	1	a.u.
λ	0.9	$\frac{mL}{g}$
M_{0b}	M_{0t}/λ	a.u.

Table 5.2.2: List of parameter values used to simulate QUASAR data. The first portion of the table reports the range of values used for the simulation. For each combination of these parameters a Monte Carlo simulation with 100 realization has been performed. The second portion of the table reports values considered fixed in the simulation.

limited to take into account only the curve portion that follows the peak. The root mean square error ($RMSE$) of the delay ($RMSE_d$) obtained with ED and with the proposed method has been computed as well. The definitions of RMSE for the aspects considered are the following:

$$\begin{aligned} RMSPE_p &\quad \sqrt{\frac{1}{N}\sum_{n=1}^{N}\left(\frac{max(R(t))-max(R_{true}(t))}{max(R_{true}(t))}\right)^2} \\ RMSPE_c &\quad \sqrt{\frac{1}{N\cdot T}\sum_{n=1}^{N}\sum_{t=1}^{T}\left(\frac{\hat{R}(t)-R_{true}(t)}{R_{true}(t)}\right)^2} \\ RMSE_d &\quad \sqrt{\frac{1}{N}\sum_{n=1}^{N}\left(\frac{\hat{\delta}_t}{\delta_t}\right)^2} \end{aligned} \tag{5.38}$$

where N is the number of Monte Carlo realizations considered in the comparison and T is the interval of considered time samples of the impulse response. The impact of delay estimation on perfusion quantification is determined by computing the percentage differences between un-

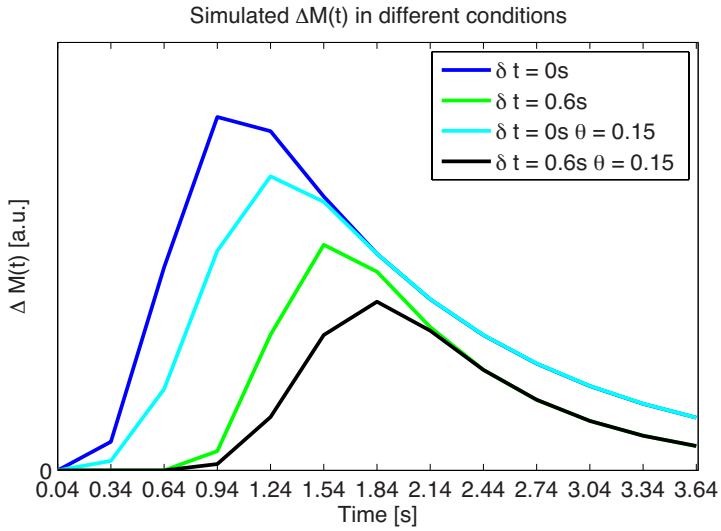

Figure 5.2.2: Example of simulated signal for assessment of performances of SS algorithm. GM simulated tissue with no delay ($\delta t = 0\ s$ blue line) and a delayed transit time of $0.6\ s$ (green line) are reported. The same parameters has been used but with additionally a dispersion to simulate the other two curves ($\theta = 0.15$, respectively light blue for $\delta t = 0s$ and black line for $\delta t = 0.6s$). The effective sampling time grid properly scaled as in QUASAR sequence is used.

biased perfusion levels (obtained by using the true simulated delay) and those obtained using the delay estimated with cSVD, oSVD and SS respectively. The method scoring the lowest $RMSPE$ or $RMSE$ is recorded and the percentage of times that each method performed better than the others has been considered as a measure of success .

5.2.2 Real Data

The real dataset has been extracted from QUASAR reproducibility study (Petersen et al., 2010b). Seven healthy subject have been included in a test retest procedure for a total of 28 scans. QUASAR scan parameters are reported in Tab. 5.2.3. The acquisition schedule is composed by 6 repetitions containing 3 non flow suppressed pairs (1 with low flip angle) and 4 pairs with flow suppression for a total of 84 measurements with duration of 5 minutes and 52 seconds. 3D high resolution T1 Magnetization Prepared Rapid Gradient Echo (MPRAGE) was included to perform

group comparison.

Parameter	Value	Unit
TR	4000	ms
TE	23	ms
ΔTI	300	ms
TI_1	40	ms
$Samples$	$40 - 3640$	ms
$Matrix\ acquired$	64×64	$a.u.$
$Slices$	7	$a.u.$
$Slice\ thickness$	6	mm
$Slice\ Gap$	2	mm
FOV	240×240	mm
$Flip\ Angle$	$35°/11.7°$	deg
$SENSE$	2.5	$a.u.$
V_{enc}	4	cm/s

Table 5.2.3: List of acquisition parameters for real QUASAR dataset. The duration of the sequence is 5 minutes and 52 seconds. The total number of measurements are respectively 48 with vascular crushing gradients on, 24 without and 12 are acquired with a lower flip angle to estimate B_1 dishomogeneities. (Petersen et al., 2010b)

5.2.2.1 Deconvolution Analysis Pipeline

Each raw dataset has been converted to be analyzed in a dedicated MATLAB software. Afterwards a fetch operation has been performed to extract the order of the different phases acquired. To avoid the inclusion of acquisitions corrupted by motion an automatic procedure has been adopted. The procedure consists in the calculation of correlation coefficients between standard deviation values of the acquired signal. The hypothesis is that the ΔM signal is invariant when considered two acquisition of the same type (crushed, uncrushed, low flip angle) and if a movement occurs the ΔM signal will be characterized by very high or very low values since control and label images are no more well aligned. Thus, the standard deviation can represent a good index of movement if calculated during the acquisition of the single phase. A correlation matrix can be created starting from each possible combination between each

standard deviation map. The result is a 2D square matrix with $N \times N$ elements (Fig. 5.2.3). The sum of each row can be seen as a goodness of alignment of the single acquisition with the others. A threshold on the mean of the rows oh the correlation matrix has been set (0.85) and all the acquisitions that scored a mean correlation below this threshold have been excluded in the estimation of the mean signal.

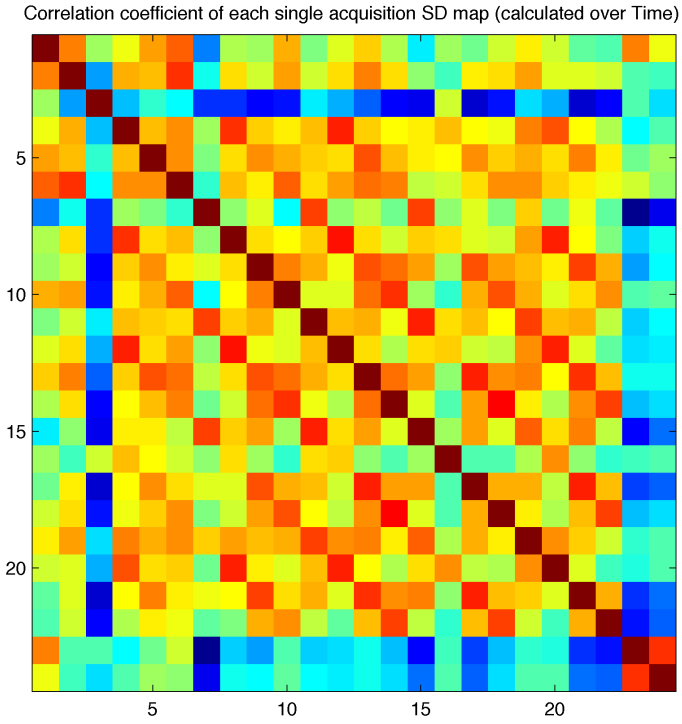

Figure 5.2.3: Pearson's correlation coefficients calculated over each single possible combination of the SD maps of crushed signal calculated over time. 24 crushed signals are acquired with QUASAR sequence. For each of this phase a SD map is then calculated, computing the SD of the signal over the 13 samples acquired with the Look & Locker readout. Each SD map is then correlated with each of the other maps forming a 2D correlation coefficients matrix. In this case phase, 3, 23 and 24 have been discarded because they produce a correlation level lower than the threshold set .

Moreover, instead of the mean, a robust M-estimator has been used

to calculate a more reliable mean across the acquisitions (Maumet et al., 2013). The extraction of the AIF and the mapping of the AIF to each tissue voxel has been performed as described in section 4.4.3. A different shape for the fitting procedure of AIF derived samples has been used. The same gamma dispersion kernel function (Chappell et al., 2013a) used for the simulation (Eq. 4.6) has been employed to fit the data and, consequently, to improve AIF description. The AIF has been fitted using a nonlinear least square approach and voxels scoring low precision in parameter estimates (coefficients of variation percentage of at least one fitting parameter higher than 100%) are discarded to avoid inclusion of inconsistent AIFs.

The estimated local AIF has been used as a parametrized input for each corresponding voxel of the crushed signal. The residue function $R(t)$ has been extracted using cSVD,oSVD and SS algorithm. A delay correction is adopted for both oSVD and cSVD-based on ED (Chappell et al., 2013b; Petersen et al., 2006). SS provides both delay and perfusion estimations for each voxel using the positivity and decreasing constraints for residue function. It has also been calculated the time arrival in macro and microvasculature. The arrival in the macrovasculature (Δt_a) has been extracted fitting the AIF with the proposed gamma kernel model. The arrival time in the microvasculature (Δt_m) has been extracted summing the delay estimated with Δt_a.

5.2.2.2 Model-Based Analysis Pipeline

All the analyses have been performed with the package QUASIL, a toolbox comprised in the fMRIB Software Library (FSL) (Jenkinson et al., 2012). The only modification has been introduced in the vascular crushing model to produce the estimates of ABS. QUASIL allows to perform the whole analysis on a command line interface. Many options can be selected. Among them it is possible to add a dispersion term. For simplicity, only the gamma dispersion kernel has been considered as an option, since it was the same model used to fit the macro vascular component in

the deconvolution pipeline. Thus, the models considered for comparison are the standard full model (VB), the same model with added the dispersion kernel (VB_d), the improved Sinc model (VB_s) and the Sinc model with dispersion kernel (VB_{sd}).

5.2.2.3 Equilibrium magnetization

Equilibrium magnetization has been estimated from a saturation recovery curve acquired with two different flip angles. A model fitting procedure built in QUASIL for saturation recovery fitting has been used to account for Look & Locker readout. The estimation of M_{0t}, T_{1t} and the actual flip angle correction factor g are the parameters to be estimated (Chappell et al., 2013b). M_{0t} has been divided by the water/blood partition coefficient of the brain to obtain M_{0b}.

5.2.3 Spatial Variability Comparison

The results obtained with each method have been compared computing the absolute and the relative percentage differences for each parameter estimated in GM and WM, respectively. To extract perfusion and other parameters distributions in GM and WM a mask for each tissue have to be calculated. To perform this task the T_1-weighted MPRAGE of each subject has been used as anatomical reference. The QUASAR acquisition space is in a different orientation respect to the anatomical reference. A co-registration step is needed to use anatomical reference information to extract GM and WM masks. The coregistration pipeline has been implemented using Advanced Normalization Tool (ANTS) (Avants et al., 2011). To obtain a mask of GM and WM in the anatomical space a segmentation algorithm has been employed (FAST implemented in FSL by Zhang et al. (2001)). GM and WM maps have been nonlinearly co-registered to the R_{1t} map ($R_{1t} = 1/T_{1t}$ estimated from the saturation recovery). The use of R_{1t} for the coregistration is preferable since it shares contrast similarities with T_1-weighted MPRAGE. The nonlinear registration has been restricted to the frequency encoding direction, where it is more probable to suffer for

distortions due to the EPI readout in the QUASAR sequence. These steps allow to calculate a mask for GM and WM (threshold level set to 70%) in QUASAR space, which have been used to build the distribution of the perfusion estimates (and other parameters of interest) with each method. To assess the performances and spatial differences in estimates obtained with the tested methods a group mean over subject has been computed. To perform a mean between subjects a further co-registration operation is needed. The anatomical T_1-weighted MPRAGE of each subject has been non linearly coregistered to the MNI 152 $2\ mm$ T_1-weighted atlas (Grabner et al., 2006). Combining the local warping and affine transformations of the two steps a transformation has been computed to move each parameter of interest from the QUASAR acquisition space to the standard MNI space to perform a group mean. Absolute and relative percentage differences for each parameter have been computed in the native QUASAR space and then transformed.

5.3 Results

5.3.1 Simulation

In this section are reviewed the results of simulated data to assess the performances of SS algorithm adapted for delay correction and estimation of perfusion from QUASAR data.

5.3.1.1 Performance indexes

Tab. 5.3.1 reports the percentage of the best performance in term of lower $RMSPE_p$ and $RMSPE_c$ scored by SS, oSVD and cSVD over all subsets of the simulated parameters conditions. Better performances are indicated by higher percentage (i.e. lower RSME scored). SS scores the best $RMSPE_p$ in 62.50% of the cases, showing a higher accuracy in the estimates of the peak and hence of the perfusion. SS exhibits a powerful advantage in estimating a physiologically interpretable R(t), scoring the best $RMSPE_c$ in 70.31% of the cases compared to SVD-based methods.

This index measures the similarity in shape between the estimated and the simulated R(t).

Index	SS	cSVD	oSVD
$RMSPEp$	62.50%	36.11%	1.39%
$RMSPEc$	70.31%	0%	29.69%
$TOTAL$	68.05%	18.05%	13.89%

Table 5.3.1: Performance comparison for residue function estimates: higher percentage values indicate lower root mean square percentage errors ($RMSPE$). Both peak level ($RMSPE_p$) and curve ($RMSPE_c$) are reported. Indexes are defined in Eq. 5.38.

Performance indexes are reported in Fig. 5.3.1, 5.3.2, 5.3.3, 5.3.4 and 5.3.5 by using 3D plots. Each plot contains the values of the index relative to the method scoring it. The axes used are respectively SNR and delay (δt) simulated values. The methods are reported by column. The first column reports SS results, the second cSVD combined with ED and the last one oSVD with ED. The indexes have been divided according to the simulated condition.

Fig. 5.3.1 exhibits $RMSPE_p$ in GM (simulated perfusion value of 50 ml/100g/min) simulated in case of un-dispersed residue function. SS shows generally a lower $RMSE_p$ than SVD-based methods and a lower degradation in performance increasing the delay.Furthermore it provides lower errors at lower SNR, degrading the performances generally less than other methods. Moreover, it shows a good approximation of the residue function shape as the graph reporting the $RMSPE_c$ in Fig. 5.3.1 shows. oSVD and cSVD instead strongly degrade the performances in the $R(t)$ shape estimation and moreover introduce a higher bias in perfusion estimation. Fig 5.3.2 displays $RMSPE_p$ in GM simulated in case of dispersed residue function. Only the case with medium dispersion has been reported as a representative case of the results obtained in case of dispersion. In general dispersion produces an underestimation effect in perfusion levels and SS provides worse performance in case of dispersion compared to its estimates in un-dispersed condition. It shows a

more stable bias than SVD-based methods, which are instead degrading the estimates introducing more bias at high delay level. Even when delay is mixed with dispersion SS provides lower $RMSPE_c$ than SVD-based methods. This is evident for delay of $0.9\ s$ at very low level of SNR.

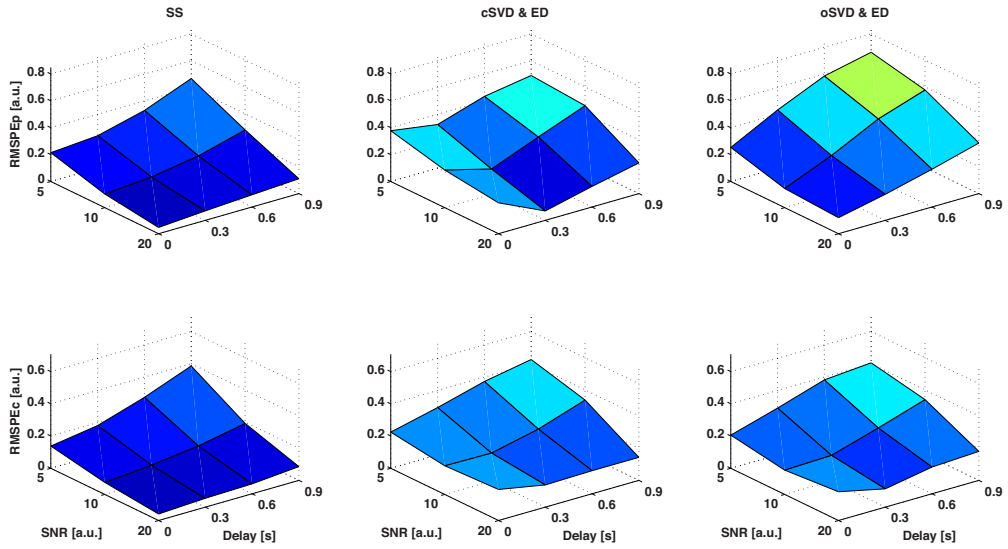

Figure 5.3.1: Root Mean Square Percentage Error ($RMSPE$) obtained with tested deconvolution methods in a GM simulated condition with an un-dispersed $R(t)$. Both $RMSPE$ of the peak level ($RMSPE_p$) and $RMSPE$ calculated over the estimated residue function ($RMSPE_c$) are plotted in function of delay and SNR.

The $RMSE_p$ in case of hyper perfusion (90 ml/100g/min) showed similar results as the simulated GM case, with a general increase in performance of SS respect to SVD-based methods. Results have not been reported for brevity. Regarding simulated WM conditions, $RMSPE_p$ and especially $RMSPE_c$ are generally higher than GM and hyper perfusion simulated conditions. As for GM the method that provides worse results in term of retrieving the residue function shape is cSVD. However it performs better in estimation of perfusion despite of the $RMSPE_c$ level. SS confirmed a good $RMSPE_p$ but compared with GM it shows a quicker degrade introducing a higher error respect to cSVD. The ability of SS in retrieving the shape of residue function is confirmed compared to SVD-

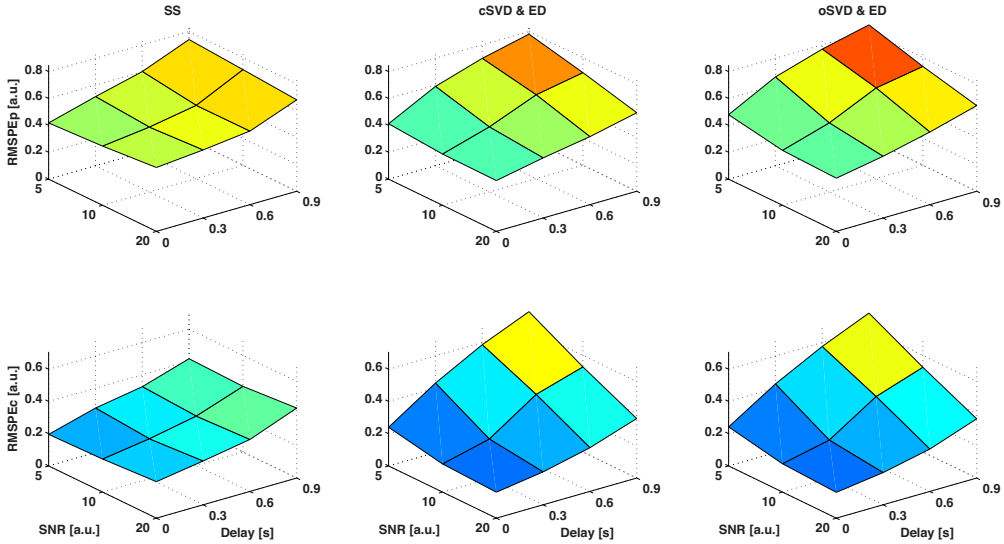

Figure 5.3.2: Root Mean Square Percentage Error ($RMSPE$) obtained with tested deconvolution methods in a GM simulated condition with a dispersed $R(t)$ and $\theta = 0.15$. Both $RMSPE$ of the peak level ($RMSPE_p$) and $RMSPE$ calculated over the estimated residue function ($RMSPE_c$) are plotted in function of delay and SNR.

based methods, as Fig. 5.3.3 reports. However when the SNR is low it tends to introduce a higher level of error in estimation of the residue function shape compared to SVD-based methods. When dispersion is coupled with low levels of perfusion as in the simulated WM case all the methods introduce higher errors in peak estimation. SVD-based methods provide worse estimation also in the approximation of the shape of $R(t)$ while SS increases in the dispersed case, especially at low SNR.

The $RMSE_d$ index indicates the precision and the robustness of estimation in case of pure delay. For this index, SS overpasses ED in the majority of the simulated cases, even in presence of dispersion (SS 87.50%, ED 12.50). In Fig. 5.3.5 the $RMSE$ in delay estimation respect to the true simulated delay is reported. The first row in the figure reports GM simulation while the plots in the second row the $RMSE_d$ in WM simulated cases. For GM and when no dispersion is introduced in the simulation, SS provides a good estimation of the delay level, while ED produces con-

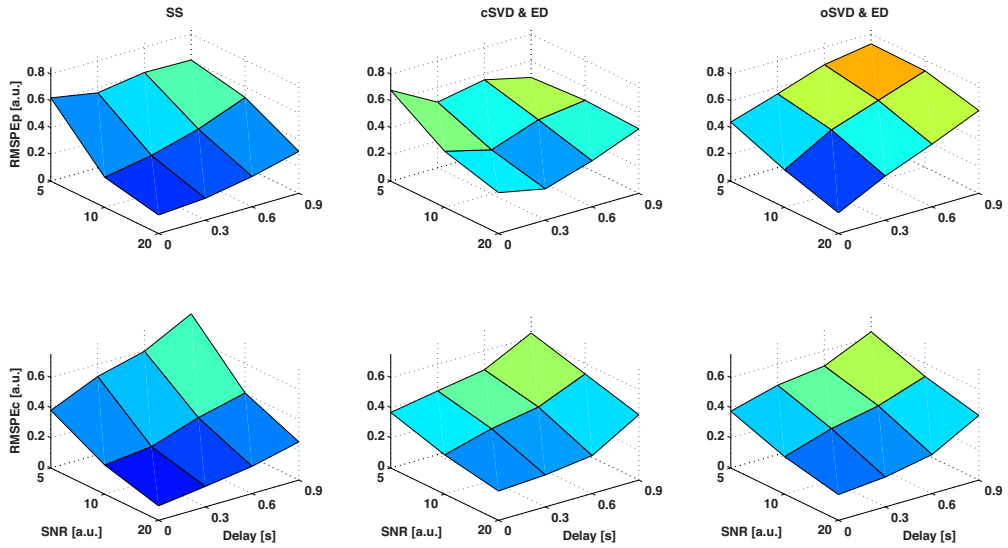

Figure 5.3.3: Root Mean Square Percentage Error ($RMSPE$) obtained with tested deconvolution methods in a WM simulated condition with an un-dispersed $R(t)$. Both $RMSPE$ of the peak level ($RMSPE_p$) and $RMSPE$ calculated over the estimated residue function ($RMSPE_c$) are plotted in function of delay and SNR.

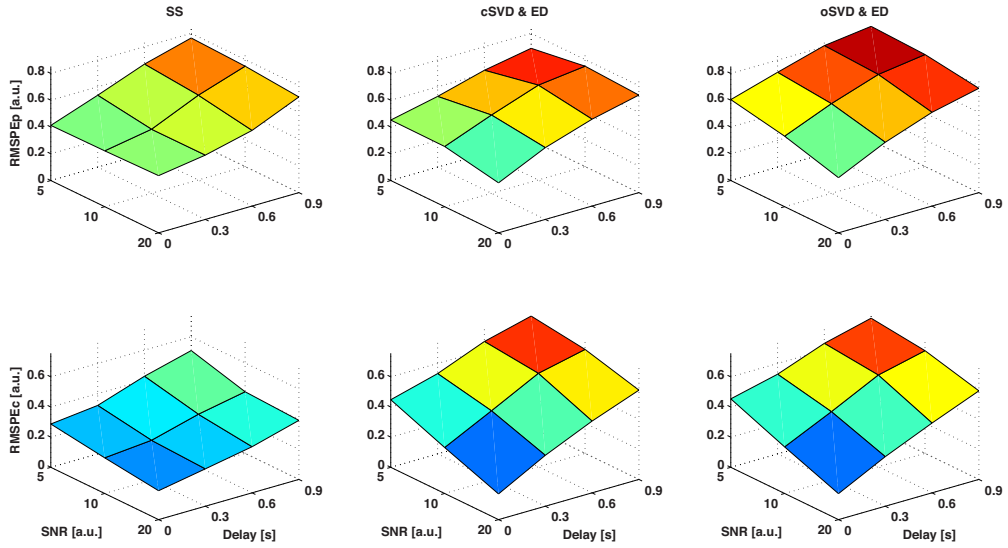

Figure 5.3.4: Root Mean Square Percentage Error ($RMSPE$) obtained with tested deconvolution methods in a WM simulated condition with a dispersed $R(t)$ and $\theta = 0.15$. Both $RMSPE$ of the peak level ($RMSPE_p$) and $RMSPE$ calculated over the estimated residue function ($RMSPE_c$) are plotted in function of delay and SNR.

stantly an higher error in estimating delay respect to SS. When dispersion is included SS introduces more error than in the un-dispersed simulated condition, but the error introduced by edge detection is still greater. In WM the delay estimates by SS are less precise and including dispersion the error introduced here is higher as for the GM simulated case. Compared to ED, SS shows lower levels of error in almost all the cases, with exception of $\delta t = 0.3$ and $SNR = 10$ where it introduces a higher level of errors than ED.

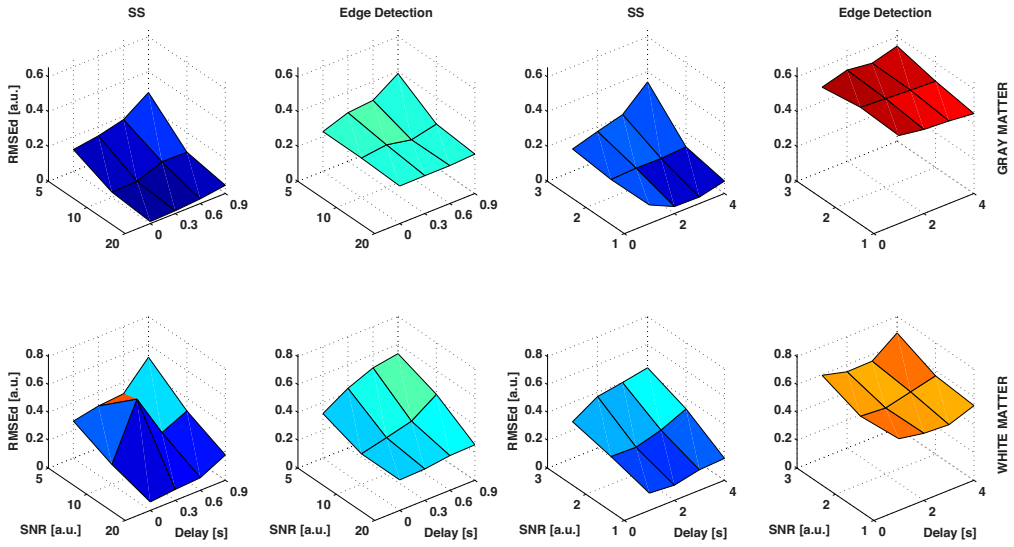

Figure 5.3.5: Root Mean Square Error (RMSE) of delay estimates obtained with Stable Spline and Edge detection are plotted in function of delay and SNR. The first row reports GM simulations while the second row WM simulation. Dispersion is introduced ($\theta = 0.15$) in the four plots on the right side of the figures, while the left side shows simulation without dispersion.

5.3.1.2 Residue function shape

The residue function shapes obtained with SS and oSVD are reported in Fig. 5.3.6. Each graph represents the median estimated $R(t)$ with the respective method and the confidential interval of the MC simulation (5^{th} and 95^{th} percentile). The simulated condition reported, as a representative situation, corresponds to GM simulated tissue and $SNR = 5$. Panel

a) shows an un-dispersed condition while b) a dispersed one ($\theta = 0.5$). For the latter a reference for the un-dispersed $R(t)$ is also displayed for comparative purpose. It is worth to note that oSVD tends to underestimate the true perfusion while SS provides more reliable estimates. When dispersion is added to the simulation both methods introduce major abnormalities in estimating the true $R(t)$ and both underestimate the true perfusion level. However SS provides narrower confidential intervals in both dispersed and un-dispersed conditions.

5.3.2 Real Data

An example for a representative GM voxel is reported in Fig. 5.3.7. The illustration reports four graphs: the first one contains the AIF fitted from the difference between uncrushed and crushed data (red dashed line) and the delay resolved AIF provided by SS (solide red line). The second one exhibits the tissue data (red circles) and the reconvolution between the estimated residue function ($R(t)$, reported in the last plot correctly scaled to extract perfusion estimates) and the AIF ($AIF(t) \otimes \hat{R}(t)$). The third one reports the weighted residuals.

5.3.3 Perfusion estimates

The novel deconvolution algorithm and the physiology based improved model have been tested on a real clinical dataset. The distributions of absolute perfusion estimates in GM and WM have been extracted and are listed in Tab. 5.3.2. The model-based approach provides a general higher perfusion level than deconvolution algorithms. In particular the SS algorithm gives a range of values more comparable to model-based approaches than SVD-based method. SVD-based methods provide a lower variance in the estimates, since their SD are lower than the ones obtained with both model-based approach and SS. The higher ratio between mean values in GM and WM has been provided by SS. The distributions in

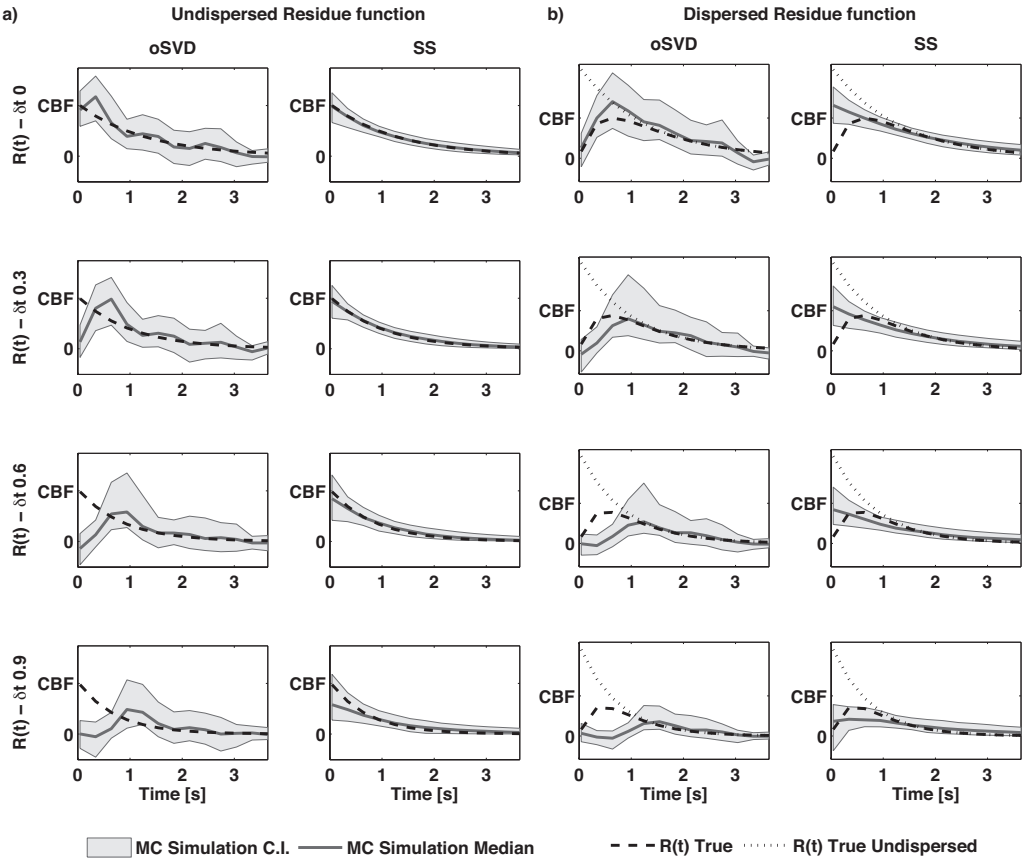

Figure 5.3.6: Residue function estimation with oSVD and SS from MC simulation with 100 realizations. The simulated condition shown here corresponds to GM condition and $SNR = 5$. Four different level of δt for un-dispersed condition: panel a) and for high dispersed $R(t)$ ($\theta = 0.5$): panel b) are reported . The graphs show in grey band MC intervals (5^{th} and 95^{th} percentile of MC simulation), in black solid line the median of the estimated $R(t)$ and in black dashed line the true simulated residue function. For the dispersion condition a reference for the un-dispersed residue function is shown.

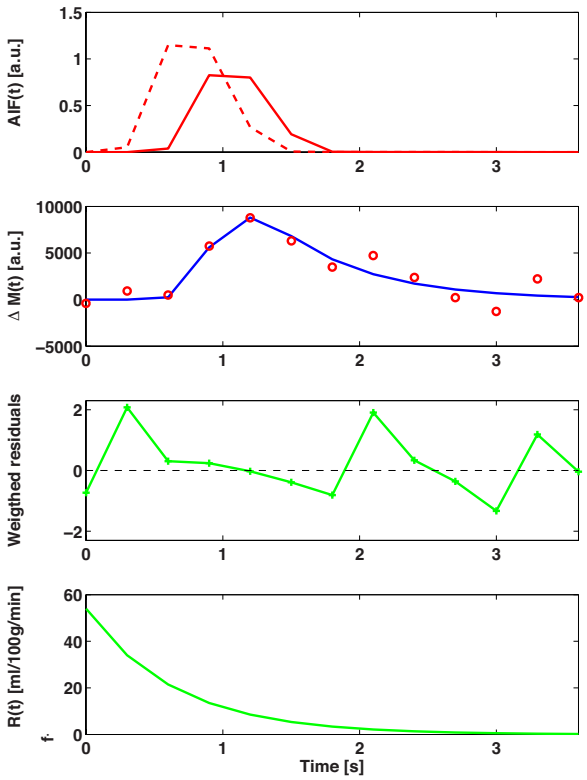

Figure 5.3.7: The illustration reports a GM voxel and the deconvolution process operated by Stable Spline, which accounted the delay between AIF and tissue. From top to bottom: Arterial Input Function (AIF) (red dashed line), delay resolved AIF provided by SS (solide red line); tissue data (red circles) and the reconvolution between the estimated residue function ($R(t)$) and the AIF; weighted residuals; residue function scaled to extract perfusion from its maximum.

both tissues provided by each method have been compared with SS estimates by using a paired t-test corrected for multiple comparisons, using Bonferroni's correction rule. Statistical significative differences were obtained for all the comparison ($p < 0.05$).

Method	GM	WM	Ratio
SS	55.49 ± 9.47	21.75 ± 7.64	2.55
$oSVD$	35.25 ± 5.30	15.31 ± 3.91	2.30
$cSVD$	42.56 ± 5.64	19.80 ± 5.13	2.15
VB	60.61 ± 8.93	25.82 ± 9.94	2.35
VB_{dk}	63.41 ± 8.72	29.94 ± 10.44	2.12
VB_s	56.60 ± 8.57	24.19 ± 9.24	2.34
VB_{sk}	59.73 ± 8.50	27.81 ± 9.81	2.15

Table 5.3.2: Absolute perfusion estimates: mean and standard deviation obtained with each tested method. The mean ratio between GM and WM has been reported for comparative purpose. All the perfusion distributions have been compared with SS estimates by a paired t-test corrected for multiple comparison, using Bonferroni's rule respectively for each distribution. Statistical significative differences were obtained for all the comparison ($p < 0.05$).

A scatterplot has been reported to compare the estimates of SS with oSVD, cSVD, VB and VB_s models (Fig. 5.3.8). The Pearson's correlation coefficient has been calculated as a measure of correlation between each method and in the two different tissues (Tab. 5.3.3). In GM a trend of correlation can be observed between SS and model-based methods while SS correlates better with SVD-based methods. General lower perfusion values are given with oSVD and cSVD respect to SS. When compared to SS the model-based approach provides very similar scatterplot distributions but with quite different absolute levels of perfusion estimates. The higher discrepancy can be observed in GM estimates between SS and model-based in the mid range of perfusion in GM ($45 - 55\ ml/100g/min$) while for higher values the methods tend to provide similar estimates. In WM the estimates are more similar between the methods, showing higher correlations. In term of absolute perfusion estimates the same observations as for GM with a minor impact could be reported. A quite relevant tail of

high values ($f > 30ml/100g/min$) have been found to be present in the WM estimates. This behavior is more evident when model-based methods are used.

Method	R^2 **- GM**	R^2 **- WM**
$oSVD$	$0.67\ (p < 0.001)$	$0.87\ (p < 0.001)$
$cSVD$	$0.84\ (p < 0.001)$	$0.85\ (p < 0.001)$
VB	$0.35\ (p < 0.001)$	$0.83\ (p < 0.001)$
VB_{dk}	$0.35\ (p < 0.001)$	$0.82\ (p < 0.001)$
VB_s	$0.37\ (p < 0.001)$	$0.82\ (p < 0.001)$
VB_{sk}	$0.39\ (p < 0.001)$	$0.80\ (p < 0.001)$

Table 5.3.3: Pearson's correlation coefficient (R^2) of the perfusion estimates calculated with all methods tested with SS as reference. Each column reports R^2 for the respective tissue and the level of significance.

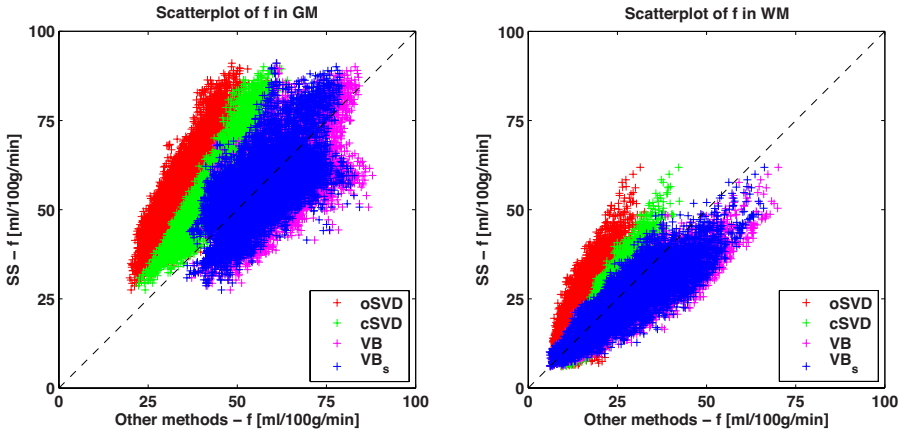

Figure 5.3.8: Scatter plot of perfusion estimates (ml/100g/min) in GM (left) and WM (right). SS is taken as reference and other methods are plotted on the opposite axis. oSVD (red crosses), cSVD (green crosses) are deconvolution methods based on SVD truncated and VB (blue crosses) and VB_s (magenta crosses) are respectively the full model-based proposed in Chappell et al. (2013b) and the improved model with a more realistic description of vascular crushing gradients.

The boxplots of the distributions of perfusion in both GM and WM are reported in Fig. 5.3.9. A line has been added to the graph as reference for GM and WM, respectively at 60 and 22 $ml/100/g/min$. Interquartile

range (IQR, between the 25^{th} and 75^{th} percentile) of estimates obtained from oSVD was the lower over all the methods in both GM and WM. In general deconvolution methods provide lower IQR intervals in both tissues than model-based approaches.

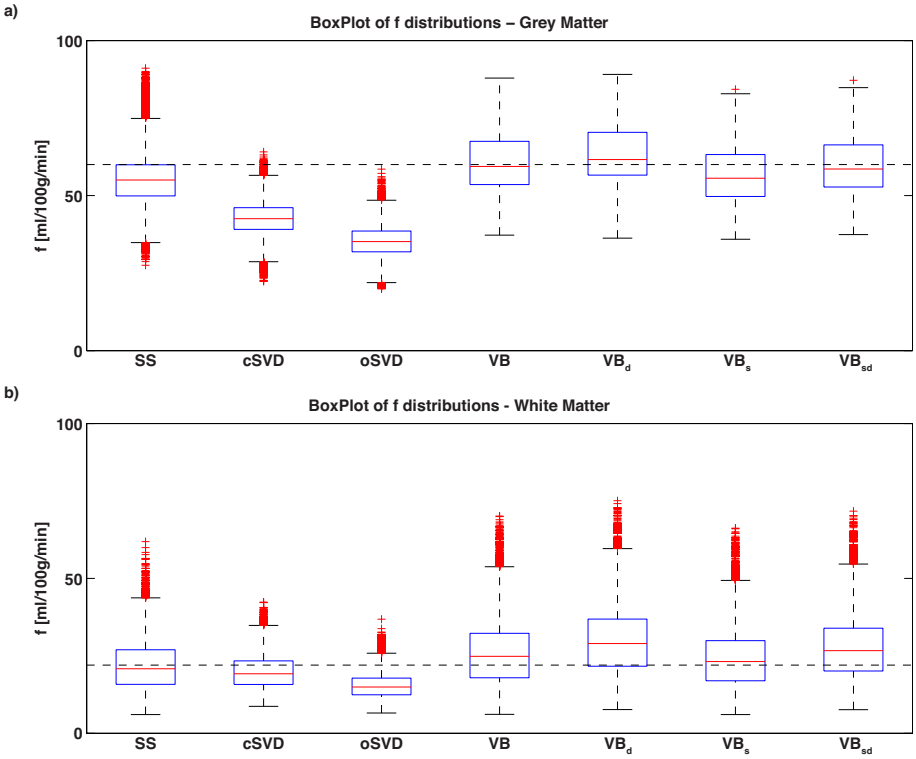

Figure 5.3.9: Boxplots of distribution of absolute perfusion estimates in GM (a) and WM (b). SS, oSVD and cSVD are deconvolution-based methods. VB is the full model proposed by Chappell et al. (2013b), and VB_s is the proposed improved model with more realistic description of vascular crushing gradients. VB_d and VB_{sd} represent the same models with added a term to take into account dispersion. Two reference lines are plotted for typical values in GM ($60\ ml/100g/min$) and WM ($22\ ml/100g/min$).

The spatial variability comparison is reported in Fig. 5.3.10 where the group mean obtained in the atlas space is displayed. The first column reports the group mean, the second the absolute difference with SS taken as reference and in the last column the percentage differences between each method and SS estimates are reported. Regarding spatial characteristics,

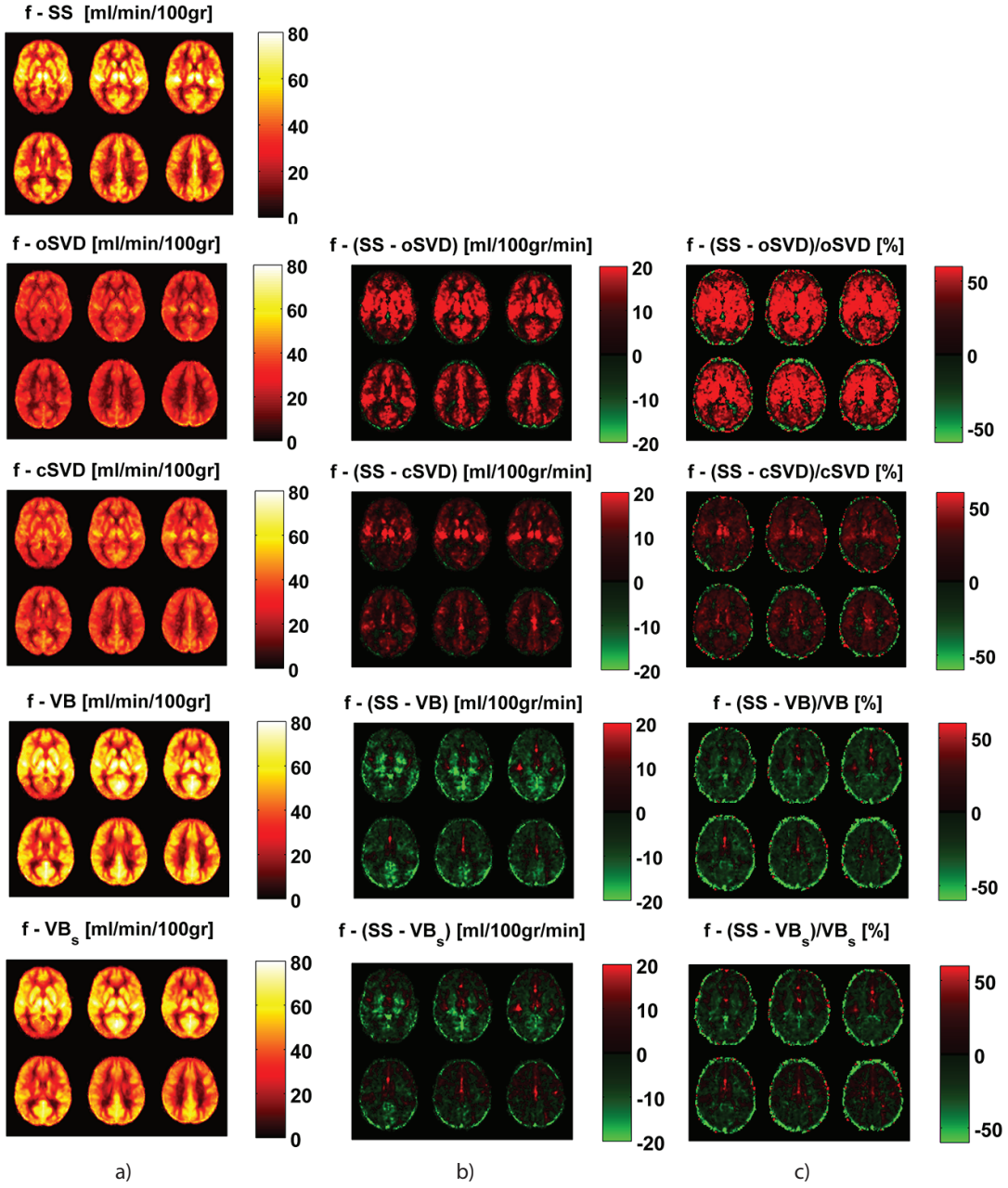

Figure 5.3.10: Spatial variability in estimation of perfusion with deconvolution and model-based techniques for central slices (z ranges from 38 to 58 in MNI152 standard space). Stable Spline results are reported in the first row as reference. a) Group mean of estimated absolute perfusion (ml/100g/min) with each method. b) Absolute differences between tested methods and SS. c) Percentage differences between tested methods and SS. Green values report higher levels of estimated perfusion and red values lower levels compared to SS.

all the images show the expected pattern for perfusion. Both SS and VB give a better contrast between GM and WM and the differences between the two tissues are more evident than with SVD-based methods. SS provides general higher values in GM than SVD-based methods. A lower difference has been found with the cSVD approach. oSVD and cSVD give higher values than SS in the deep WM areas. On the contrary, when compared with model-based methods SS estimates are generally lower but with some bright spot of higher flow located in areas where a high vascular content is expected. In particular the VB_s model, compared to VB provides closer values to SS in GM. Furthermore the differences are more enhanced in areas characterized by a high vessel content. The posterior district for circulation is also different in spatial distribution in term of perfusion estimates between tested methods. Differences between SS and VB are more evident. However, when VB_s model is used it provides estimates closer to SS and more homogeneous than standard VB estimates.

The model-based approach coupled with gamma kernel for dispersion has not been included in this spatial distribution because no evident differences have been found respect to the un-dispersed model.

5.3.3.1 Delay and Arrival time

The delay estimation feature that has been added to SS has been compared with the edge detection algorithm comparing the spatial variability of the estimates in a standard space as it has been done previously for perfusion. Moreover the delay estimated with SS has been summed to the arrival time in the macro vasculature (Δt_a), estimated from the correspondent AIF to obtain estimates of arrival time in the micro vasculature (Δt_m). This has been performed to compare the SS performance in estimation of delay and arrival time in micro vasculature. Delay estimation by SS is generally lower than the one obtained with ED, with exception of the regions where a prominent macro vascular component is expected. As for perfusion the estimated delay has been extracted in both WM and

GM. Mean and standard deviation are reported in Tab. 5.3.4. It is worth to note that major differences are located in WM, where ED provides higher estimates: statistically significant differences have been found between SS and ED delay estimates (paired t-test with significance level $p < 0.05$, corrected for multiple comparison using Bonferroni's rule).

Method	GM	WM
SS	0.42 ± 0.11	0.65 ± 0.13
ED	0.44 ± 0.13	0.71 ± 0.14

Table 5.3.4: Transit delay between macro and micro vasculature (δt in seconds): mean and standard deviation obtained with each tested method on the total 28 acquisitions.

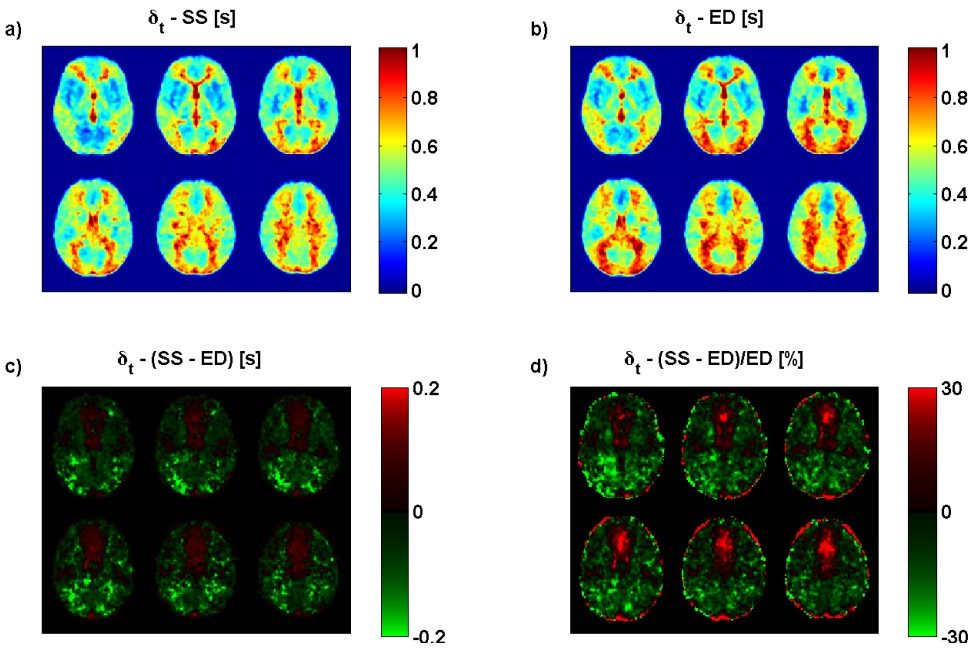

Figure 5.3.11: Spatial variability, computed as group mean, in estimation of delay between AIF and tissue, obtained with SS and ED (central slices are shown: z ranges from 38 to 58 in MNI152 standard space). a) Stable Spline b) Edge Detection c) Absolute differences between SS and ED d) Percentage differences between SS and ED. Green values report higher levels of estimated delay by ED while red values report the opposite.

Comparing the arrival time in micro vasculature estimation obtained with SS and VB, the former provides higher values for Δt_m especially where a relative high contribution of macro vascular component is not expected . The mean and standard deviation calculated over all the subjects are reported in Tab. 5.3.5. SS and ED provide both higher levels of Δt_m in WM while in GM the distributions are more comparable to model-based approaches. Anyway, paired t-tests (significance level $p < 0.05$ corrected for multiple comparison using Bonferroni's rule) between SS estimates and other methods reveal significant differences in all the cases. Introducing a dispersion component the mean value of Δt_m strongly decreases with the novel model VB_s, while a more subtle difference can be noted comparing VB and VB_d.

Method	GM	WM
SS	0.66 ± 0.16	0.88 ± 0.16
ED	0.68 ± 0.18	0.94 ± 0.17
VB	0.69 ± 0.07	0.76 ± 0.05
VB_{dk}	0.67 ± 0.09	0.74 ± 0.06
VB_s	0.60 ± 0.10	0.74 ± 0.06
VB_{sk}	0.53 ± 0.08	0.68 ± 0.07

Table 5.3.5: Arrival time in the micro vasculature (Δt_m in seconds): mean and standard deviation obtained with each method tested on the total 28 acquisitions. SS and ED arrival time has been obtained adding the arrival time in the macro vasculature (Δt_a) to the delay estimated (δt). For model-based approaches it represents the arrival time estimated as a free parameter. All the Δt_m distributions have been compared with SS estimates with a paired t-test corrected for multiple comparison, using Bonferroni's rule respectively for each distribution. All the tested conditions revealed statistical significant differences (significance level $p < 0.05$).

Spatial differences evaluation follows the same scheme as for perfusion estimates. The reference method is SS and is showed in Fig. 5.3.12 on the first row. The comparison excludes the ED method since the only differences from SS is the delay estimation, compared previously. SS provides higher estimation in Δt_m in WM compared to all tested methods. GM differences in estimated Δt_m change dependently on the model used,

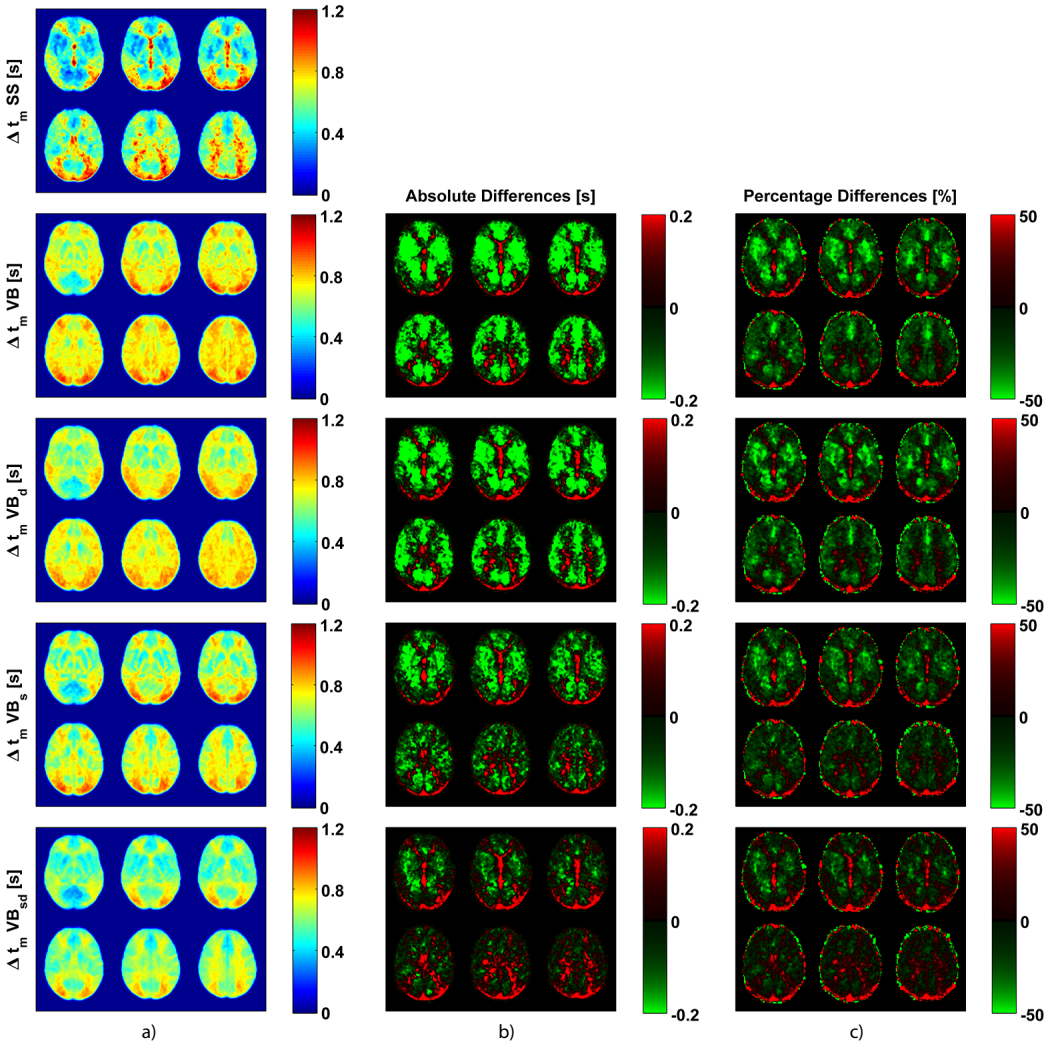

Figure 5.3.12: Spatial variability in estimation of arrival time in the micro vasculature Δt_m with SS and model-based techniques for central slices (z ranges from 38 to 58 in MNI152 standard space). Stable Spline results are reported in the first row as reference. a) Group mean of estimated Δt_m with each method. b) Absolute differences between tested methods and SS. c) Percentage differences between tested methods and SS. Green values report higher levels of estimated Δt_m and red values lower levels compared to SS.

providing major differences for VB and less for VB_s. When dispersion is introduced in the models the differences in estimating the Δt_m decrease, with major impact on the novel model VB_{sd}. WM differences remain more stable independently on the model used.

5.3.3.2 New model assessment

To assess the goodness of fit of the novel proposed model, its performances and parsimony, the negative free energy (FE) of the model fit in each voxel can be used. The FE can be calculated as part of the probabilistic method used. The FE approximates the Bayesian evidence for a model, and thus in principle it combines the accuracy of a model fit to the data with a penalty for the number of free parameters in the model (Chappell et al., 2009). In short, the closer the FE is to zero the better the model is at explaining the data. To better understand the spatial variability of the estimated, FE the same procedure employed to test both perfusion and delay estimated has been performed.

The spatial variability map of the group mean of $log(-FE)$ is shown in Fig. 5.3.13. The FE maps show a perfusion dependent pattern on the brain, exhibiting higher values where the mix of the two components, the tissue and the macro vascular, are likely to be both present. The two models have more difficulties in estimating both macro and micro vascular component simultaneously than the only tissue component. FE estimated values favor the new model introduced to better describe the macro vascular component and the crushing operation that vascular crushing gradients perform on it, while in the areas where a remarkable macro vascular component is not excepted the differences are less evident and FE values are comparable. Negative differences (green values) indicate a better performance of the VB_s model: this is primarily the case in regions of high aBV where arteries would be expected in the brain. Moreover the new model provides the possibility to estimate the spatial distribution of the mean blood velocity of the macro vascular component (ABS) in absolute unit $[cm/s]$. Estimates of mean ABS in the principal ar-

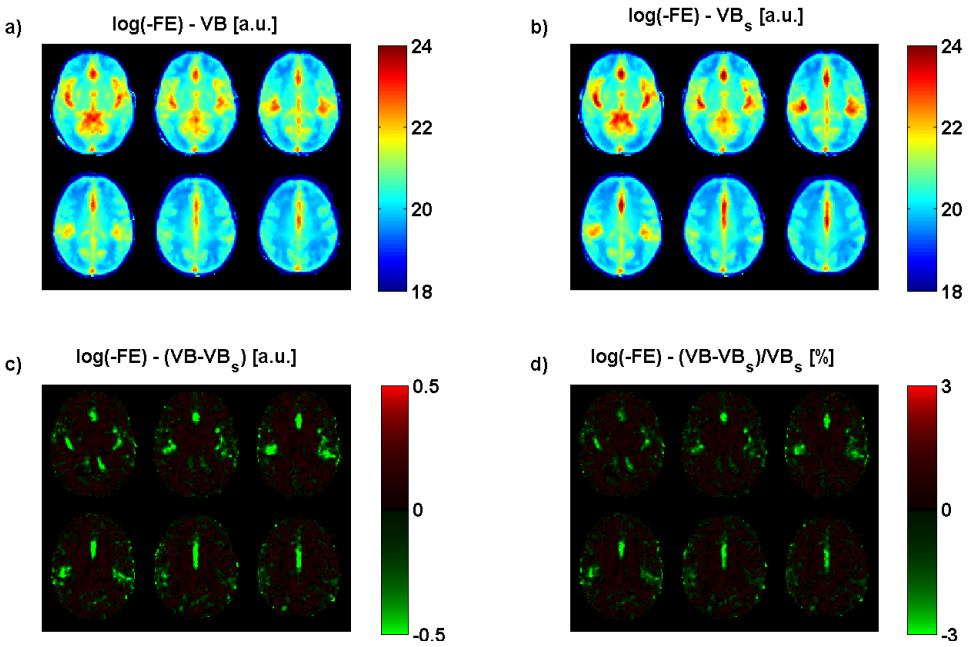

Figure 5.3.13: Group mean free energy of the proposed novel model compared to the original full model proposed by Chappell et al. (2013b) for central slices (z ranges from 38 to 58 in MNI152 standard space). Where the differences map shows green values the new model is favored compared to the original full model.

terial vessels are shown in Fig. 5.3.14 as a mean across the group: values of mean flow speed in the range $3 - 5\ cm/s$ were found in areas where middle cerebral artery branches would be expected.

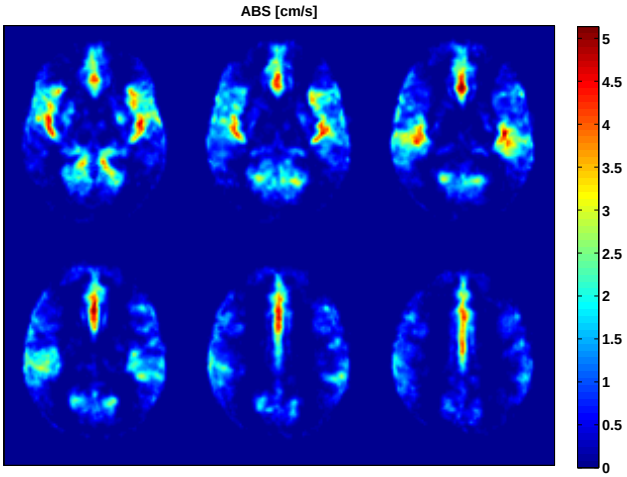

Figure 5.3.14: Group mean of the blood velocity of the macro vascular component estimated by the new proposed model VB_s for central slices (z ranges from 38 to 58 in MNI152 standard space). ABS is shown in absolute unit (cm/s)

5.4 Considerations

QUASAR data offer the unique possibility in ASL to quantify cerebral perfusion and bolus arrival time, allowing at the same time, to account for the possible presence of dispersion of the labeled bolus. This chapter introduces a novel method to quantify absolute perfusion, delay between AIF and tissue and arrival time in the micro vasculature with a kernel based deconvolution approach, named Stable Spline (Pillonetto and De Nicolao, 2010). SS takes its name from the Bounded Input Bounded Output (BIBO) stability constraint that has been introduced to provide smooth and regular impulse response estimates. Moreover, to better address the problems of ASL and achieve a physiologically interpretable impulse response, a positivity and a decreasing constraint has been included. The original implementation of SS does not allow to take into

account delay between AIF and tissue. Thus a new implementation of SS obtained modifying the first step, where the marginal likelihood is computed, has been introduced. This formulation however is not as robust as the original SS since the deconvolution problem as it is cast, is strongly not convex. To allow SS to estimate robustly δt a pre-step to provide an initial guess for this parameter has been proposed. This initial guess can be thought as an initialization step for SS that is then free to perform the minimization of the same cost function used in its original implementation, with a further parameter, i.e. the delay.

This approach has been evaluated in a broad simulated scenario, with different levels of perfusion, delay and SNR. The performances of this method have been compared with the standard deconvolution algorithms used in clinical environment, such as SVD-based methods, circular SVD and block circulant SVD. The results in the simulated scenario certify that SS provides better estimate in term of perfusion in 62.5% of the simulated cases. Moreover, the goodness in approximating the true residue function supports the superior performance of SS (exhibiting a lower error in 70.31% of the simulated cases). The analysis of these indexes can also describe how in function of δt and SNR SS performs compared to SVD-based methods. When no dispersion is introduced, SS provides better performances than other methods. However its performance degrades quicker when SNR decreases; this might be explained by the nonlinear fitting procedure introduced to take into account delay and that suffers for ill-defined initial values, which can drive the minimization to a local minimum. Nevertheless SS is able to recover a better description of the true $R(t)$ also when SNR is low, as showed in Fig. 5.3.6. When dispersion is added to GM simulated conditions, the behavior of SS degrades as the one of SVD-based methods. Its sensibility to dispersion is not related to the level of noise present in the data. Indeed $RMSPE_p$ increases only when the delay is mixed with dispersion. Moreover SVD methods perform worse when SNR is low as it is expected in dispersed conditions.

SVD-based methods combined with edge detection introduce a double bias in the estimation. Indeed, SVD-based methods are known to under-

estimate perfusion in almost all conditions due to the oscillation inserted in the $R(t)$. This is coupled with ED, which tends on the contrary to overestimate the δt: this will produce an overestimation effect also on perfusion since the delay introduces a scale factor on it. This effect can be seen as a compensatory effect but in fact the errors introduced are higher than the ones introduce by the SS framework. This behavior is amplified when dispersion is added, since it can be seen as a late arrival time of the bolus, if the sample time is not enough narrow to catch this little modification in the signal. In the case of QUASAR, the sample time is $300\ ms$ and the whole kinetic is estimated to disappear due to T_1 decay of the tracer in approximately 3 seconds. Hence, little dispersion effects can be seen as delay and vice versa. The two phenomena can be difficultly separated and both SS and SVD with ED can overestimate delay to compensate for dispersion effects. A solution could be to include in the formulation of the $R(t)$ an additional dispersion component as in Zanderigo et al. (2009) and (Ahlgren et al., 2013) where a Nonlinear Stochastic Regularization (NSR) algorithm has been employed. The main disadvantage of NSR is that it should trust the estimates of delay provided by ED that has been demonstrated to introduce a bias when dispersion is coupled to delay. Further investigations are needed to assess the feasibility of adding a dispersion component to the $R(t)$ in the SS framework.

The ability of SS to recover the true $R(t)$ when dispersion is included is demonstrated in Fig. 5.3.2 where SS shows a better and more stable error in estimating the shape of $R(t)$. oSVD shows a better performance than SS when SNR and delay are not present in the data. However its performance quickly degrades when delay increases and SNR decreases respectively. When simulations are applied to lower levels of perfusion, like WM, it is worth to be noted that the SNR level is lower compared to GM, since it is calculated on the maximum value of the noiseless signal of a pure GM voxel. This has been done to take into account real measurements of ASL data. SS performances in this case are worse than in GM (as expected) and cSVD tends to provide better perfusion estimations than SS in this condition. A note should be added in presence of disper-

sion. WM tissue perfusion estimation with ASL is prohibitive. Nevertheless, it has been shown to be feasible, with other types of sequences (van Osch et al., 2009; Wu et al., 2013). It has been proved that in healthy subjects dispersion is more present in WM than GM (Ahlgren et al., 2013). All tested methods score higher errors in the WM case. Nevertheless SS provides perfusion estimates inline with other SVD-based methods but it provides a more sensible performance in recovering the true $R(t)$.

An alternative approach to estimate f and other related parameters have been proposed by Chappell et al. (2013b). The proposed model is a full model made up by two components and that can account for vascular crushing gradients modification applied to macro-vascular component. The estimation procedure is computed by using a Variational Bayes approach to include a priori information on the estimated parameters. Here an improved model that better describes the relation introduced by the vascular crushing gradients is proposed. A $Sinc$ modulation to the scalar product of the flow direction and the gradient direction vectors has been added for this purpose. This modification permits to estimate also a new parameter, the mean blood velocity of the macro vascular component (ABS). It has been shown how it can describe the data, providing a better free energy measure than the original VB model. The range of the new parameter is approximately $3-5\ cm/s$ in large arterial branches. This result is not in line with literature value, which indicates a blood speed of a pure artery voxel in order of $25cm/s$. However, the low resolution of QUASAR can include partial volume effects than can lead to a broader dispersion of the true velocity of the vessels. Further validations are required to understand the robustness of this measurement.

The original model and the improved one and have been compared as was done in Chappell et al. (2013b) adding SS and taking it as a reference to compare the perfusion estimates and their spatial variability in the brain. The two approaches differ in how to take into account dispersion and how to model the residue function from the data. Deconvolution techniques try to infer this directly from the data while model-based approaches impose it describing the physiological system. The spatial

variability comparison is in line with simulation results obtained by Petersen et al. (2006): model-free techniques tend to underestimate perfusion while model-based approaches tend to overestimate perfusion as noise increases. This is due to the non physiologically interpretable oscillations introduced in $R(t)$ by SVD-based methods and to the restricted description of the system given by model-based approaches respectively. Scatterplots in Fig. 5.3.8 point out this general trend. However it is clear how deconvolution based methods consider the subtraction between uncrushed and crushed acquisitions to be perfect. Hence their performance suffers for the residual component not crushed by vascular crushing gradients as already confirmed by previous studies (Chappell et al., 2010, 2013b). SS tends to provide estimated values for perfusion in the middle of classical SVD methods and model-based approaches. It is promising that the discrepancy between the novel model and SS is lower than the one obtained with the previous version of VB. However when a dispersion gamma kernel is added to the proposed model it still shows a general higher level of estimated perfusion compared to SS. SS provides the higher ratio between mean value of GM and WM, and it is inline with expected ratios between the tissues.

Comparing WM estimates SS provides higher mean estimates than cSVD and oSVD, but the spatial variability maps show than in deep WM SVD-based methods provides a slightly higher level of perfusion in WM. This might be explained by the high level of dispersion and delay mixed together. The level of perfusion estimated by SVD-based methods would be lower than SS; however when it is corrected by the delay provided by ED (that has been demonstrated to overestimate the true delay) this can balance the underestimation of perfusion due to SVD. It is clear how this consideration should be first tempered with the high level of noise that is present in WM areas, especially deep WM zones.

The arrival time in the micro vasculature Δt_m, obtained summing the arrival time in macro vasculature and the delay estimated with SS, has been compared with the one extracted by model-based approaches. The range of Δt_m values provided by SS is inline with other studies (Chappell

et al., 2010; Petersen et al., 2006; Sousa et al., 2013). Moreover it is comparable with VB model-based approach in GM but in WM the estimated arrival time is higher. This is explained by the level of noise in WM and the lack of any hypothesis about residual dispersion between the local AIF and the tissue signal not taken into account in SS approach.

The major drawback of SS is its computational burden in comparison to oSVD (however less than other approaches such as NSR (Ahlgren et al., 2013)). The SS implementation used here takes approximately 30 minutes to process a complete subject. This might represent a limitation for its wider application, but this can be considered improvement over NSR in term of computational cost. Further works are needed to use parallel computing optimizations and to bring its powerful capabilities nearer to the clinical environment.

QUASAR has introduced several possibilities to study perfusion and other related parameters and numerous clinical studies have been published using since its creation (Mak et al., 2012; Noguchi et al., 2012; Paling et al., 2013). However care should be taken in choosing the best methodology for the quantification process in case of pathological conditions. The method that can better distinguish the pathological modification occurring in the tissues should be selected. At the moment it is difficult to say which technique is the most reliable to use (Chappell et al., 2013b). It might be a further direction to combine the possibility of the new proposed model with SS to better model the AIF relation that links macro and microvascular components of the signal and to limit the sensitivity of SS to macro vascular artifacts. In conclusion it has been shown, both in simulated and real case conditions, that the use of SS to estimate perfusion with QUASAR data is possible and could be used as an alternative of model-based techniques and SVD-based approaches.

Happiness lies in the joy of
achievement and the thrill
of creative effort.

Franklin D. Roosevelt

6

A two component model for quantification of pCASL with Look & Locker readout

PASL sequences suffer from lower signal to noise ratio compared to pCASL. This appealing property suggests to use pCASL as the best labeling technique. However, since the labeling period is prolonged compared to PASL it is impossible to sample the whole kinetic curve of the magnetized blood. The aim of this section is to demonstrate that it is possible to estimate the arrival time in the micro vasculature using a pCASL labeling technique and moreover that it is possible to combine different acquisitions employing vascular crushing gradients to extract also information of the macro vascular component. To accomplish this aim a Look & Locker readout has been combined with a pCASL labeling technique in order to investigate the feasibility of correction of macro vascular arti-

facts and to extract information on the macro vascular component, such as the arterial blood volume (aBV). Here an extensive section is dedicated to introduce a priori information in a nonlinear model, such as the model used for the quantification of both macro vascular and tissue components. Afterwards a two component model based on the assumption that it is possible to separate the contributions of both macro vascular signal and tissue one (Chappell et al., 2010) is presented and validated.

6.1 Real Dataset

MR images have been acquired with a Philips Achieva 3T MRI-scanner using a 8-channel head coil. Five healthy subjects (27.5 ± 1.68 years of age, 2 males) have been scanned using the same protocol. All subjects gave informed consent after the nature of the procedure examinations were explained. The acquisition session was constituted of:

- high resolution T_1-weighted MR images, acquired using a MPRAGE sequence ($256 \times 256 \times 160$ matrix dimension, $1 \times 1 \times 1\ mm^3$ voxel dimension), providing anatomical information

- perfusion-weighted ASL images acquired using a multislice 2D-EPI readout in combination with Look & Locker sampling strategy. EPI readout has been designed to accomplish the acquisition of seven axial slices (64×64 matrix, with $3.5 \times 3.5\ mm^2$ in plane resolution, slice thickness of $6\ mm$), in a temporal window of $T_{slice} = 33\ ms$ per slice. For Look & Locker readout, parameters set was given by $TI_2 = 300ms$ sampling period, $N = 15$ number of TI, and $\alpha_{LL} = 35°$ flip angle of multiple excitation pulses. With these settings, 13 images at TI ranging from $40\ ms$ to $3640\ ms$ after the end of labeling scheme, equally spaced in time by amount $\Delta TI = TI_2$, were acquired in order to adequately sample the kinetic curve of inflowing blood and allow model fitting. Label/control pairs acquisition was repeated $N = 30$ times for subsequent signal averaging.

pCASL, with a labeling duration $\tau = 1.6s$ has been used as labeling technique. The gap between labeling plane and imaging region has been set to encounter the carotid anatomy of the subject, adjusting the orientation as perpendicular as possible to them. Look & Locker pCASL experiment has been repeated with and without bipolar gradients to compare differences in perfusion-weighted images due to signal from intra-vascular blood. The bipolar crushing gradients used ($v_c = 4\ cm/s$) have been applied in the z-direction directly after readout preparation to dephase flowing spins, with $TE = 23\ ms$ long enough to accomodate their presence. All acquisitions uses a SENSE acceleration factor of 2.5.

- Saturation recovery with the same Look & Locker readout geometry and modality of pCASL has been added to estimate both M_0, T_{1t}. To allow the actual flip angle estimation a second saturation recovery with a lower flip angle (11 °) has been employed, similar to the QUASAR sequence (see Section 5.2.2.3).

6.2 Implementation of Maximum a posteriori estimator

Let 's consider the voxelwise model for ASL signal, using a vector notation:

$$y = \Delta M(p) + v$$

where y represents the acquired data, $\Delta M(p)$ the model prediction obtained with Buxton model adapted to pCASL and v is the noise in the measuring process. When a bayesian approach is performed, also a statistical description of random error vector is required. A common assumption on vector v is that it is a random error vector and considered to be a realization of an additive white gaussian noise (AWGN) process,

with zero mean and covariance matrix (of dimension $[N \times N]$) given by:

$$\Sigma_v = \begin{bmatrix} \sigma_1^2 & & \\ & \ddots & \\ & & \sigma_N^2 \end{bmatrix}$$

Note that the variance of the random process describing v is not constant in the sampling grid. This is caused by the Look & Locker readout employed. Statistical description given to random error vector can be condensated in:

$$v \sim N(0, \Sigma_v) \tag{6.1}$$

In the bayesian framework adopted, vector p contains the parameters to be estimated with a MAP estimator, that are:

$$p = [f,\, T_{1t},\, \Delta t]^T \tag{6.2}$$

A priori distributions were considered informative only for parameters T_{1t}, while no a-priori information has been used for the other parameters. This can be formally handled by associating to these parameters generic prior distributions (e.g.. normal) with infinite variance. Practically it means to use a flat prior that allows parameters to take any value with the same probability:

$$\begin{aligned} T_{1t} &\sim LN(\mu_{T_{1t}},\, \sigma_{T_{1t}}) \\ f,\, \Delta t, &\sim N(\cdot,\, \infty) \leftarrow \text{uninformative priors} \end{aligned} \tag{6.3}$$

A general statistical description of a-priori information on parameters vector p can be given in terms of mean vector (dimension $[M \times 1]$), and covariance matrix (dimension $[M \times M]$):

$$\mu_p = \begin{bmatrix} \vdots \\ \mu_{T_{1t}} \end{bmatrix} \qquad\qquad \Sigma_p = \begin{bmatrix} \infty & \\ & \sigma_{T_{1t}}^2 \end{bmatrix} \tag{6.4}$$

where the mean vector and covariance matrix are written respecting the

same order used in parameters vector definition (Eq. 6.2). Σ_p definition implicitly assumes statistical independence of parameters, denoted by null off-diagonal elements, while the absence of useful prior knowledge for some parameters is highlighted by the infinite diagonal elements.

The set of optimal parameters given by MAP estimator are those that maximize the posterior probability of parameters given the data (the objective function of estimation procedure). Remembering the considerations that lead to Eq. 4.23, $\hat{p}^{MAP}$is given by:

$$\begin{aligned}\hat{p}^{(MAP)} &= \underset{p}{argmax}\,(P(p \mid y)) \\ &= \underset{p}{argmax}\,(P(y \mid p)P(p))\end{aligned} \tag{6.5}$$

where the likelihood function $P(y \mid p)$, under assumption of independence between vector parameters p, and noise vector v, and according to random error vector v statistical description, is a multivariate normal distribution:

$$\begin{aligned}P(y \mid p) &= N(\Delta M(p),\, \Sigma_v) \\ &= \frac{1}{\sqrt{(2\pi)^N det\,[\Sigma_v]}} \mathsf{e}^{-\frac{1}{2}(y-\Delta M(p))^T \Sigma_v^{-1}(y-\Delta M(p))}\end{aligned} \tag{6.6}$$

The prior probability $P(p)$ can be expressed as the product of single parameters probability distributions, as a consequence of having assumed parameter a-priori distributions to be statistically independent:

$$\begin{aligned}P(p) &= \prod_{m=1}^{M} P(p_m) = P(T_{1t})P(p^{ni}) \\ &= \frac{1}{T_{1t}\sqrt{2\pi}\,\sigma_{T_{1t}}} \mathsf{e}^{-\frac{1}{2}\left(\frac{ln(T_{1t})-\mu_{T_{1t}}}{\sigma_{T_{1t}}}\right)^2} P(p^{ni})\end{aligned} \tag{6.7}$$

In the above equation, p^{ni} indicates the subset of parameters for which no a-priori knowledge is assumed ($p^{ni} = [f,\, \Delta t]$). It automatically means that $P(p^{ni})$ takes a constant value whatever value the parameters subset

p^{ni} assumes ($P(p^{ni}) = K,\ \forall p^{ni} \in \mathbb{R}^2$).

Taking together Eq. 6.6 and Eq. 6.7 and combining them into Eq. 6.5, optimal MAP parameter values are given by:

$$\begin{aligned}
\hat{p}^{MAP} &= \underset{p}{argmax}\,[P(y \mid p)P(p)] \\
&= \underset{p}{argmax}\left[\frac{\mathrm{e}^{-\frac{1}{2}(y-\Delta M(p))^T\Sigma_v^{-1}(y-\Delta M(p))}}{\sqrt{(2\pi)^N det\,[\Sigma_v]}}\frac{\mathrm{e}^{-\frac{1}{2}\left(\frac{ln(T_{1t})-\mu_{T_{1t}}}{\sigma_{T_{1t}}}\right)^2}}{T_{1t}\sqrt{2\pi}\,\sigma_{T_{1t}}}P(p^{ni})\right] \\
&= \underset{p}{argmax}\left[\frac{\mathrm{e}^{-\frac{1}{2}(y-\Delta M(p))^T\Sigma_v^{-1}(y-\Delta M(p))}\mathrm{e}^{-\frac{1}{2}\left(\frac{ln(T_{1t})-\mu_{T_{1t}}}{\sigma_{T_{1t}}}\right)^2}}{T_{1t}\sqrt{(2\pi)^{N+2}det\,[\Sigma_v]}}\sigma_{T_{1t}}\right]
\end{aligned} \tag{6.8}$$

where the constant value assumed by factor $P(p^{ni})$ (independent from the parameters as a consequence of flat distributions adopted) permits to discard it from the optimization function. The objective function is given by the product of non-negative monotonic functions (probability distribution), so taking the natural logarithm of Eq. 6.8 will not change the global optimum. This reduces the objective function into a form more suitable for numerical methods used to solve optimization problems, and permits to ignore in the expression the terms that not include parameters, yielding:

$$\begin{aligned}
\hat{p}^{MAP} &= \underset{p}{argmax}\,[ln\,(P(y \mid p)P(p))] \\
&= \underset{p}{argmax}\left[-\frac{1}{2}\parallel y-\Delta M(p)\parallel^2_{\Sigma_v^{-1}} -\frac{1}{2}\left(\frac{ln(T_{1t})-\mu_{T_{1t}}}{\sigma_{T_{1t}}}\right)^2 - ln(T_{1t})\right] \\
&= \underset{p}{argmin}\left[\underbrace{\parallel y-\Delta M(p)\parallel^2_{\Sigma_v^{-1}}}_{\text{fidelity to data}} + \underbrace{\left(\frac{ln(T_{1t})-\mu_{T_{1t}}}{\sigma_{T_{1t}}}\right)^2 + 2ln(T_{1t})}_{\text{lognormal prior}}\right]
\end{aligned} \tag{6.9}$$

Eq. 6.9 represents the final form of the cost function when MAP estimator is applied to obtain optimal model parameters values in a bayesian

framework. It results from the general assumptions that have been made: (a) unknown parameters p independent from noise statistical description and (b) statistical independence between parameters to be estimated. The meaning of the different terms that contribute to general cost function can be clearly recognized: the first represents cost function to be minimized when simple WNLLS approach is used for parameters estimation and the second term represents the penalty due to lognormal prior on T_{1t}. Note that as long as assumptions (a) and (b) are valid, prior knowledge on other parameters can be inserted in the computation simply by adding an appropriate (normal or lognormal) term inside the cost function (Eq. 6.9).

Eq. 6.9 shows that $\hat{p}^{MAP}$ evaluation requires the knowledge of Σ_v. Hence noise covariance matrix can be modeled as follows:

$$\Sigma_v = \sigma^2 B$$

where matrix B is known, set to the inverse of weights matrix W used in WNLLS, $B = W^{-1}$, while σ^2 is an unknown scaling factor that has to be estimated a-posteriori. Unbiased estimator of σ^2 is given by $\frac{WRSS}{N-M}$, where $WRSS$ (weighted residuals sum of square) is $\parallel y - \Delta M(p) \parallel^2_{B^{-1}}$ evaluated at its minimum (when parameters assume their optimal values). In the bayesian framework adopted, σ^2 a-posteriori estimation requires an iterative scheme since every modification of σ^2 alters the cost function optimum due to the presence of priors terms in addition to residuals sum of squares. σ^2 can be thought as a correction on relative weights of data respect to a-priori information in MAP cost function (Eq. 6.9). The following scheme can be used to determine σ^2 and the final estimations for

optimal $\hat{p}^{MAP}$:

$$\underset{\text{initialization}}{\Sigma_v^{(0)} = B}$$

$$\Downarrow$$

$$p^{MAP(0)} \Rightarrow \sigma^{2(0)} = \frac{WRSS}{N-M} \Rightarrow \underset{\text{iteration 1}}{\Sigma_v^{(1)} = \sigma^{2(0)}\Sigma_v^{(0)}} \Rightarrow \text{condition on } \sigma^{2(0)}?$$

$$\Downarrow$$

$$p^{MAP(1)} \Rightarrow \sigma^{2(1)} = \frac{WRSS}{N-M} \Rightarrow \underset{\text{iteration 2}}{\Sigma_v^{(2)} = \sigma^{2(1)}\Sigma_v^{(1)}} \Rightarrow \text{condition on } \sigma^{2(1)}?$$

$$\Downarrow$$

$$\ldots$$

At every step, covariance matrix is updated by a new a-posteriori $\sigma^{2(k)}$ correction. The termination condition is met when the last correction factor is no longer effective, that is $0.95 \leq \sigma^{2(k)} \leq 1.05$.

The final parameters vector estimation is given by $\hat{p}^{MAP(k)}$ and the a-posteriori σ^2 estimation is:

$$\sigma^2 = \prod_{i=0}^{k-1} \sigma^{2(i)}$$

where k is the iteration number in which output condition has been met. A further exit condition has been introduced to limit the maximum number of iteration to $k = 5$. This framework can be used even in presence of an initial estimate for σ^2 calculated directly from the data. Hence, the formulation chosen is to initialize B with an estimate of the noise. It is possible to calculate a guess of the uncertainty of the measurements from the background in the images. A square of 20×20 has been extracted from background of each control and label image. Considering the mean standard deviation of each control and label image through all the repetitions acquired in the experiments, this can give an approximation of the level of the noise level, but more importantly it can give a relation due

to the Look & Locker readout between each phase acquired. To calculate the initial guess for B, it is possible to insert in the diagonal elements the sum of the squares of the standard deviation previously calculated for both control and label:

$$B_0 = \hat{\Sigma}_v^{control} + \hat{\Sigma}_v^{label} \tag{6.10}$$

This probably leads to an overestimation of the noise that is present in the data, but the key is that the relative weights of data points acquired in the tail of the Look & Locker readout are characterized by higher uncertainty.

The knowledge of noise covariance matrix Σ_v make possible also the measure of the uncertainty of estimates. Cramer-Rao inequality (Carson and Cobelli, 2001) establishes a lower bound for covariance matrix of estimates, $\Sigma_{\hat{p}^{MAP}}$, and expresses it in terms of Fisher matrix information, $F(p)$, evaluated at optimal parameters vector value $\hat{p}^{MAP}$:

$$\Sigma_{\hat{p}^{MAP}} \geq \left[F(\hat{p}^{MAP})\right]^{-1} = (S^T \Sigma_v^{-1} S + \Sigma_p)^{-1} \tag{6.11}$$

where S is sensitivity matrix of dimensions $[N \times M]$, whose generic element at position $[i, j]$ is given by $\left[\frac{\partial \Delta M(t_i,p)}{\partial p_j}\right]$. The equivalence at second member of Eq. 6.11 holds if random vectors p and v are gaussian. This condition is unfortunately not satisfied because T_{1t}, belonging to parameters vector, is supposed to be lognormally distributed. However, Eq. 6.11 can considered likewise, because lognormal distributions with mean far from zero can be well approximated by normal distributions. Variance of estimated parameters can be approximated to the second member of Eq. 6.11, thus ignoring inequalities and giving an underestimation of actual estimates uncertainty. This can be viewed as a Laplace approximation on the posterior distribution, which is forced to be a multivariate normal distribution with covariance matrix $\Sigma_{\hat{p}^{MAP}}$ in the correspondence of its maximum (Okell et al., 2012). Beyond all these considerations, the effect of a-priori knowledge inclusion on parameters model identification is clearly visible: the final estimate of $\hat{p}^{MAP}$ shows smaller variance than

when no a-priori information is used and ideally yields $\Sigma_p^{-1} = 0$.

6.2.1 Optimization strategy

MAP estimation of model parameters has been performed by minimization of a cost function (Eq. 6.9), which is essentially the cost function of WNLLS approach updated by the presence of prior related terms. The estimation has been carried out in custom MATLAB code, using a trust region minimization algorithm (Coleman and Lii, 1996). In detail, the process requires the computation of the minimum, with respect to parameters, of a function made up by a sum of squares. This sum of squares is essentially the euclidean norm of a vector deriving from the evaluation of an input function $O(t,\, p)$ at a series of time points $t_1,\, t_2, \ldots,\, t_N$, i.e. the acquisition time points of the experiment. To make it clear, in data fitting problems $O(t_k,\, p)$ is simply the residual at sampling time t_k, i.e. the discrepancy between observed data and model prediction (eventually normalized by a proper weight). Hence, the minimization problem is formalized as:

$$\begin{aligned} \hat{p} &= \underset{p}{argmin} \left[\| \, O(t,p) \, \|^2 \right] \\ &= \underset{p}{argmin} \left[O(t_1,p)^2 + \ldots + O(t_N,p)^2 \right] \end{aligned} \tag{6.12}$$

where $O(t_k,\, p)$ can be interpreted as the element k of the following vector:

$$O(p) = \begin{bmatrix} O_1(p) \\ O_2(p) \\ \vdots \\ O_N(p) \end{bmatrix}$$

If a MAP estimator has to be included in this minimization approach, its cost function needs to be expressed as a sum of squares so that the appropriate vector $O(p)$ can be easily extracted. This requirement ideally could be straight satisfied by taking the square roots of each term in Eq. 6.12 to

form vector O. Unfortunately, the lognormal prior, in particular the term $ln(T_{1t})$, hinders a non trivial complication. The natural choice would lead to treat $ln(T_{1t})$ as the square of an hypothetical element vector $\sqrt{ln(T_{1t})}$. This solution is not feasible because likely to provoke the arrest of the computation, since negative values for $ln(T_{1t})$ (forbidden with $\sqrt{\cdot}$ operator) could be reached during optimization that evaluates vector $O(p)$. This happens whenever T_{1t} assumes values inferior to $1\ s$, which was a very common situation since T_{1t} values for WM and GM fall right across this critical value. For these reasons the term associated to lognormal prior has to be rearranged so that it can be expressed as a squared term.

Let K be the set of lognormal terms in Eq. 6.9, it can be elaborated as follows:

$$\begin{aligned} K &= ln(T_{1t}) + \frac{1}{2}\left(\frac{ln(T_{1t}) - \mu_{T_{1t}}}{\sigma_{T_{1t}}}\right)^2 \\ &= ln(T_{1t}) + \frac{1}{2\sigma^2_{T_{1t}}}\left(ln^2(T_{1t}) - 2ln(T_{1t})\mu_{T_{1t}} + \mu^2_{T_{1t}}\right) \\ &= \frac{1}{2\sigma^2_{T_{1t}}}\left(2\sigma^2_{T_{1t}}ln(T_{1t}) + ln^2(T_{1t}) - 2ln(T_{1t})\mu_{T_{1t}} + \mu^2_{T_{1t}}\right) \\ &= \frac{1}{2\sigma^2_{T_{1t}}}\left(ln^2(T_{1t}) + 2ln(T_{1t})(\sigma^2_{T_{1t}} - \mu_{T_{1t}}) + \mu^2_{T_{1t}}\right) \end{aligned} \tag{6.13}$$

The overall goal is to reduce K to a squared form like $Cg(p)^2$, with C scalar coefficient and $g(p)$ a scalar function of model parameters vector. Then the element of vector O associated with the lognormal prior would be clearly defined: it would be $\sqrt{K} = \sqrt{C}g(p)$. The expression in bracket in Eq. 6.13 resembles the square of a binomial, but to be exactly a square of binomial it needs an adjustment. Adding and subtracting the quantity $\sigma^4_{T_{1t}} - 2\mu_{T_{1t}}\sigma^2_{T_{1t}}$ to the third term in brackets, it results:

$$K = \frac{1}{2\sigma^2_{T_{1t}}}\left(ln(T_{1t}) + (\sigma^2_{T_{1t}} - \mu_{T_{1t}})\right)^2 + \frac{1}{2\sigma^2_{T_{1t}}}\left(-\sigma^4_{T_{1t}} + 2\mu_{T_{1t}}\sigma^2_{T_{1t}}\right)$$

Combining this new expression for lognormal term into Eq. 6.9, and

discarding the second part independent from parameter T_{1t}, MAP cost function becomes a sum of squares and can now be implemented into the minimization algorithm:

$$\begin{aligned}\hat{p}^{MAP} &= \underset{p}{argmin}\left[\frac{1}{2}\parallel y-\Delta M(p)\parallel^2_{\Sigma_v^{-1}}+\frac{1}{2}\left(\frac{M_{0b}-\mu_{M_{0b}}}{\sigma_{M_{0b}}}\right)^2+K\right]\\ &= \underset{p}{argmin}\left[\frac{1}{2}\parallel y-\Delta M(p)\parallel^2_{\Sigma_v^{-1}}+\frac{1}{2}\left(\frac{ln(T_{1t})+(\sigma^2_{T_{1t}}-\mu_{T_{1t}})}{\sigma_{T_{1t}}}\right)^2+\dots\right]\\ &\left[\dots+\frac{-\sigma^4_{T_{1t}}+2\mu_{T_{1t}}\sigma^2_{T_{1t}}}{2\sigma^2_{T_{1t}}}\right]\\ &= \underset{p}{argmin}\left[\underbrace{\parallel y-\Delta M(p)\parallel^2_{\Sigma_v^{-1}}}_{\text{fidelity to data}}+\underbrace{\left(\frac{ln(T_{1t})+(\sigma^2_{T_{1t}}-\mu_{T_{1t}})}{\sigma_{T_{1t}}}\right)^2}_{\text{lognormal prior}}\right]\end{aligned} \tag{6.14}$$

From Eq. 6.14, input vector is directly obtained by taking the square root of each term:

$$O(p)=\begin{bmatrix}\frac{y(t_1)-\Delta M(t_1,p)}{\sigma_1}\\ \frac{y(t_2)-\Delta M(t_2,p)}{\sigma_2}\\ \vdots\\ \frac{y(t_N)-\Delta M(t_N,p)}{\sigma_N}\\ \frac{ln(T_{1t})+(\sigma^2_{T_{1t}}-\mu_{T_{1t}})}{\sigma_{T_{1t}}}\end{bmatrix}$$

This shows that MAP estimator can be formulated in terms of LS approach, when normal or lognormal prior distributions for model parameters are chosen. As a consequence MAP optimal parameter values can be achieved minimizing the retrieved cost function (Eq. 6.14).

T_{1t} PRIOR DISTRIBUTION

Once the MAP estimator has been included in the optimization, the estimates of the longitudinal magnetization of the tissue T_{1t} have been set voxelwise as a prior for the Buxton model. It has been hypothesized

that the distribution of the parameter follows a lognormal distribution with mean equal to the estimates obtained from the double flip angle estimation procedure and the standard deviation has been set to a uniform value of $0.1\ s$.

6.3 Macro Vascular component

An alternative approach to correct vascular artifacts without compromising the SNR of the acquired signal has been proposed. It aims at explicitly model the intravascular signal and then at including it in a two component model to account for the effects of arterial tagged spins in multi-TI ASL data. The general expression of the two-component model is:

$$\Delta M(t, p, p_a) = (1 - aBV)\Delta M_t(t, p) + aBV\Delta M_a(t, p_a) \tag{6.15}$$

where ΔM_t is the tissue component whose expression is given by Buxton model and p is its vector of unknown parameters, ΔM_a is the new arterial component with vector of parameters p_a, and aBV is the arterial blood volume fraction, usually expressed as a percentage of the entire voxel volume.

A detailed description of model equations for the macro vascular component, as proposed by Okell et al. (2012) for estimation of angiographic ASL data is presented. $\Delta M_a(t)$, is derived with respect to the pseudo-continuous labeling schemes. In general, arterial component has to represent simply the transit of the labeled blood bolus through a large artery. To model this phenomenon, an application of the general kinetic model (see section 4.1.1) is not appropriate.

Arterial component model $\Delta M_a(t)$ is thus essentially the kinetic curve of a bolus of tagged blood that is expected to transit in large arteries. A detailed model can be derived incorporating the effects that the labeled bolus is expected to experience while traveling from the inversion plane, where it is created, to each single voxel in the imaging region. The transit through an artery in ideal conditions, can be defined by the typical box-

car shape:

$$w(t) = \begin{cases} 0 & t < \Delta t_a \\ 1 & \Delta t_a \leq t < \Delta t_a + \tau_a \\ 0 & \Delta t_a + \tau_a \leq t \end{cases}$$

where Δt_a is the arterial transit delay, and τ_a is the arterial bolus duration. The effects to be modeled are: decay of the label with time due to magnetization relaxation, signal attenuation operated by excitation RF pulses as the blood passes through the imaged region, and physiological dispersion of bolus profile as it travels along vasculature, which can be properly accounted for by the definition of three functions of time, $M(t)$, $R(t)$ and $K(t)$ respectively. Using these functions, a general model for arterial component $\Delta M_a(t)$ is derived, adopting the convolution integral formulation given by Okell et al. (2012):

$$\begin{aligned} \Delta M_a(t) &= 2\alpha M_{0b} \int_{-\infty}^{\infty} w(t - t_d) K(t_d) M(t, t_d) R(t, t_d) dt_d \\ &= 2\alpha M_{0b} \int_{t-\Delta t_a-\tau_a}^{t-\Delta t_a} K(t_d) M(t, t_d) R(t, t_d) dt_d \end{aligned} \tag{6.16}$$

The dispersion function $K(t_d)$ is a convolution kernel describing the fraction of the bolus that arrives at the voxel level delayed by time t_d (Chappell et al., 2013a). Thus $K(t)$ is given by a Gamma dispersion Kernel.

$M(t, t_d)$ describes the T_1 decay experienced by the blood after labeling during its transit from the point it has been inverted to the voxel considered. Its definition depends, of course, on the type of labeling performed and also includes the additional T_1 decay during delay t_d resulting from bolus dispersion effects, so:

$$M(t, t_d) = \mathrm{e}^{-(\frac{\Delta t_a + t_d}{T_{1b}})} \tag{6.17}$$

$R(t, t_d)$ accounts for the effects on signal amplitude of imaging pulses

used in the Look & Locker readout. Each pulse collected by blood before transit through the considered voxel reduces the longitudinal magnetization by a factor of $cos\alpha_{LL}$. Thus, function $R(t, t_d)$ is given by:

$$R(t, t_d) = (cos\alpha_{LL})^{N(t,t_d)}$$

where $N(t, t_d)$ gives the actual number of RF pulses experienced by the blood at time t since its entrance in imaging region. For sake of simplicity, in the follow the dependance of $N(\cdot, \cdot)$ on t_d is ignored, which is equivalent to consider ineffective the delay effects introduced by dispersion in the computation of the number of RF pulses experienced by blood. Even the expression of $N(t)$ depends on the type of labeling.

In pCASL, since the same coil is used both for labeling and imaging, during the labeling step no RF excitation pulses are applied to the imaging region. Starting from t_0, the sampling time in which the first pulse is played out, the number of previous pulses that at time t blood has been affected by is:

$$N(t) = floor\left(\frac{t - t_0}{TI_2}\right) \approx \frac{t - t_0}{TI_2} \tag{6.18}$$

where the continuous approximation for $N(t)$ is made, in the same manner in which Look & Locker readout pulses are incorporated into Buxton model (see section 3.4.2.1). Eq. 6.18 implicitly assumes that the imaging region encompasses everything distal to the labeling plane, but often there is a gap between labeling plane and imaging region within which blood does not experience any imaging pulses. Named δt_{min} the time that blood from feeding arteries takes to enter into the imaging region, the maximum amount of time spent in the imaging region before reaching the voxel of interest is $\Delta t_a - \delta t_{min}$. This time limits the number of RF pulses experienced by the blood, thus the expression for $N(t)$ becomes:

$$N(t) \approx min\left\{\frac{t - t_0}{TI_2}, \frac{\Delta t_a - \delta t_{min}}{TI_2}\right\} \tag{6.19}$$

where the approximated nature of $N(t)$ must be kept in mind, further-

more remembering that effects due to dispersion are not accounted for in its evaluation.

Using the former definitions, expression for arterial component model $\Delta M_a(t)$ can be obtained just placing them into the convolution integral Eq. 6.16 and solving it. The solution for pCASL is given by:

$$\begin{aligned}\Delta M_a(t) &= 2\alpha M_{0b} \int_{t-\Delta t_a-\tau_a}^{t-\Delta t_a} K(t_d)M(t,t_d)R(t,t_d)dt_d \\ &= 2\alpha M_{0b}\,(cos\alpha_{LL})^{min\left\{\frac{t-t_0}{TI_2},\,\frac{\Delta t_a-\delta t_{min}}{TI_2}\right\}}\,\mathsf{e}^{-\frac{\Delta t_a}{T_{1b}}} \int_{t-\Delta t_a-\tau_a}^{t-\Delta t_a} K(t_d)\mathsf{e}^{-\frac{t_d}{T_{1b}}}dt_d\end{aligned} \tag{6.20}$$

where the explicated integral can be solved analytically by manipulating the solution to Eq. 4.6, given in section 4.3 to define gamma dispersion on the delivery function of Buxton model $c(t)$.

6.3.1 Two component fitting procedure

The arterial model validation has been performed fitting the first contribution $aBV\Delta M_a(t)$ to a signal given by the difference between data in which no vascular suppression was applied (NVC data) and those acquired with vascular crushing (VC data). This difference signal (NVC-VC) gives the actual portion of ASL signal crushed by the application of bipolar gradients for flow suppression, and thus can be considered as a good surrogate of the real macro vascular component associated to the voxel. The fitting of the single arterial model $\Delta M_a(t)$ on this "dedicated" dataset were conducted considering as unknown the following vectors of parameters:

$$p_a = [aBV,\, \Delta t_a,\, p,\, s]$$

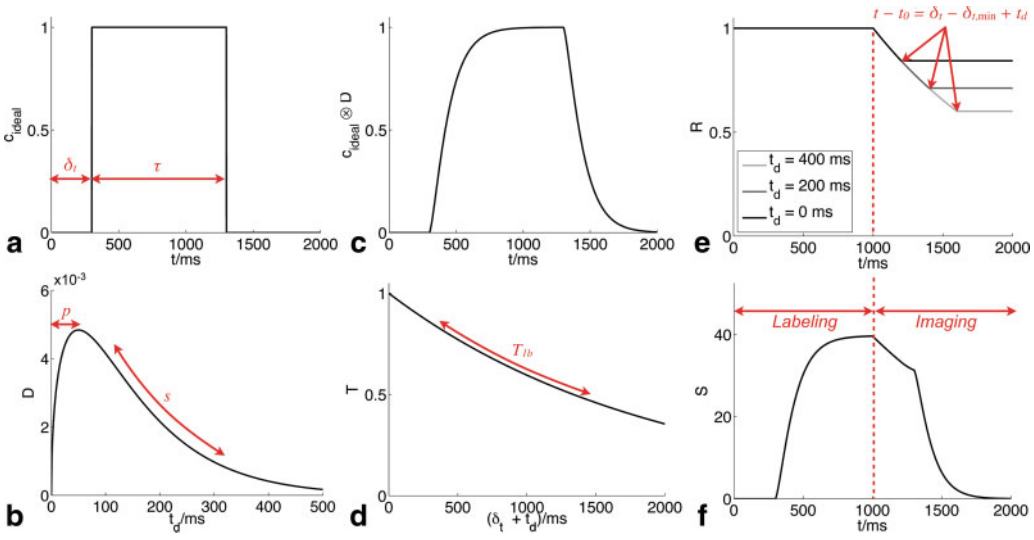

Figure 6.3.1: Illustration of the various parts of the macro vascular kinetic model describing the ASL signal evolution: the ideal labeled blood concentration is a rect function (a); convolution with a dispersion kernel (b) yields a modified curve (c); when T_1 decay is taken into account (d), and effects due to the RF excitation pulses (e, plotted for three different t_d values). Note that RF effects are not present before the start of imaging and the curve flattens out to a constant when the time relative to the start of imaging is greater than the time the blood has spent in the imaging region (which varies with t_d). Combining these effects yields the final model curve (f), which is also scaled by M_{0b} and aBV. For long labeling durations ($\tau > \delta t$), only the latter portion of the curve will be observed (as shown in (f)) as imaging cannot commence until the labeling has finished. Taken from Okell et al. (2012).

A set of a-priori knowledge (informative only on some of them) was considered, by adopting normal prior distributions to be used in a bayesian estimation framework (with MAP estimator). Prior distributions on parameters were set to values already used in literature (Chappell et al., 2010, 2013a; Okell et al., 2012) and are reported in the following Tab. 6.3.1.

Parameter	Prior distribution
aBV [%]	uninformative prior
Δt_a [s]	$\sim N(0.5, 0.1)$
p [s]	$\sim N(0.05, 0.1)$
s [s^{-1}]	$\sim N(5, 0.5)$

Table 6.3.1: Prior distribution descriptions used for macro vascular component model fitting included in the MAP estimator. These parameters have been retrieved from previous studies (Chappell et al., 2010, 2013a; Okell et al., 2012)

Parameter δt_{min} has been estimated voxelwise, extracting the voxels showing the earlier arrival time on the first slice (2% of the voxels showing the earlier time to the half of the integral of the signal), and fitting the macro vascular component imposing δt_{min} to zero. Then the arrival time estimates in these voxels has been propagated as the δt_{min} of the surrounding voxels based on the euclidean distance.

Arterial model component ΔM_a evaluated in this ideal condition, was then considered as a fixed contribution, Y_a, apart from its amplitude, letting the two component model to better describe the data, but with a prior information on aBV, derived from the MAP estimates of the macro vascular component:

$$\begin{aligned}\Delta M(t, p, p_a) &= (1 - aBV)\Delta M_t(t, p) + \underbrace{aBV \Delta M_a(t, p_a)}_{\text{NVC}-\text{VC estimate}} \\ &= (1 - aBV)\Delta M_t(t, p) + aBV \Delta M_a({p_a}^{MAP}) \end{aligned} \tag{6.21}$$

The tissue contribution, $(1-aBV)\Delta M_t(t, p)$ of the two component model, was then fitted to the NVC data, using the same estimation settings de-

fined when Buxton model parameters estimation has been described (see section 4.5.1). The aBV coefficient was constrained to satisfy a relation involving the estimates of the arterial contribution amplitude as a priori information inserted in a second MAP estimator, for the two component model. To assure coherent scaling between the two components they were estimated in separate consecutive stages (Fig. 6.3.2).

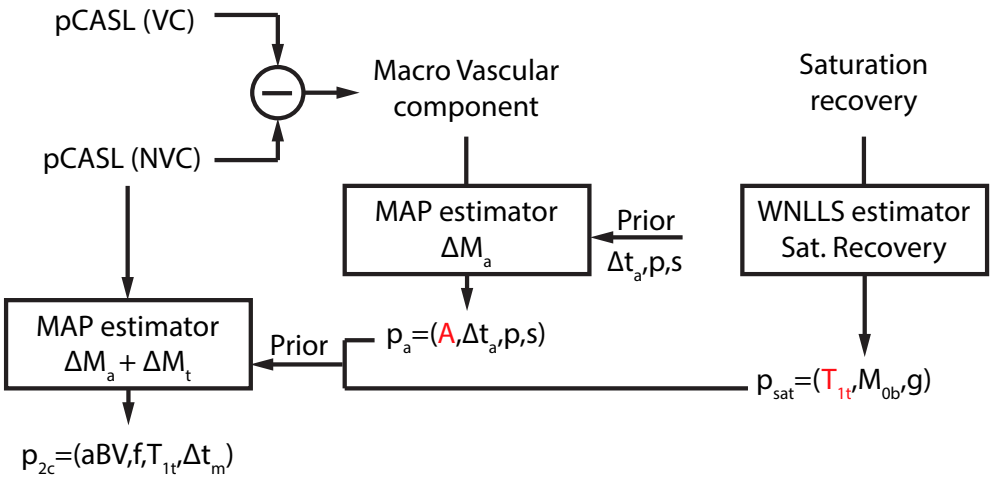

Figure 6.3.2: Pipeline of analysis for pCASL with Look & Locker readout. The pCASL uncrushed (NVC) and crushed (VC) are subtracted to obtain data to fit the macro vascular component with the model proposed by Okell et al. (2012). The estimation is carried out using a MAP estimator with prior value extracted from literature. Values of the priors can be found in Tab. 6.3.1. T_{1t} extracted from the fit of a double flip angle saturation recovery is used as a-priori information on a two component model that will fit the sum of tissue and macro vascular components, weighted by the arterial blood volume, to the NVC dataset. The estimation framework is a MAP estimator with forcing function retrieved by the macro vascular component parameters.

Performances of the novel two component model have been evaluated in both WM and GM tissues. The distribution of this parameters has been extracted using a similar approach to the QUASAR dataset (see section 5.2.3), using the T_1 MPRAGE segmented and co-registered with the pCASL space. In this case, due to the limited number of subjects no spatial variability has been performed and only an analysis of correlation to confirm that the novel model is able to provide high correlated estimates

to the Buxton model, when the former is applied to the crushed dataset, has been performed.

6.4 RESULTS

The five subjects have been analyzed to compare the performances in perfusion estimation and to evaluate the feasibility of using a two component model to correct for macro-vascular artifacts. The standard Buxton model applied to NVC data provides macro vascular artifacts that are evident from the first row of Fig. 6.4.1. The macro vascular component has been fitted to the difference signal obtained from NVC and VC data using a MAP estimator. Then the estimated parameters are used as a forcing function for the two component model, letting the estimator to be free to rescale the arterial component to better describe the NVC signal. In Fig. 6.4.1 are reported the estimates of perfusion obtained for a representative subject. It is worth noting that macro vascular artifacts are not present in the last row, when the two component model is used and the perfusion map is highly correlated to the perfusion map obtained from the standard buxton model estimates.

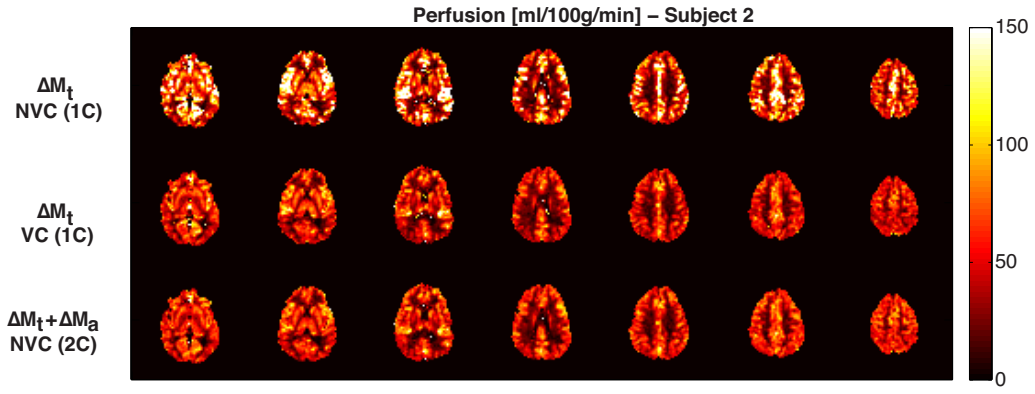

Figure 6.4.1: Absolute perfusion estimates for a representative subject, obtained with the Buxton model (1C) to the crushed (VC) and uncrushed (NVC) dataset and the proposed two component model (2C) applied to NVC data after that the macro vascular component has been estimated from the difference between the two datasets and used as a forcing function.

Mean and standard deviations of perfusion estimates obtained with both models are reported in Tab. 6.4.1. The two component model perfusion estimates are slightly higher than when Buxton model is applied to VC data (GM_{2C} = 56.64 $\pm$ 36.07,GM_{1C} = 50.23 $\pm$ 26.65). This effect is more evident in GM than in WM (WM_{2C} 28.30 $\pm$ 28.36, WM_{1C} 26.98 $\pm$ 29.71). Also the grade of variance in perfusion estimates is higher for the new model.

Subject	$\mathbf{GM}_{2C}$	$\mathbf{GM}_{1C}$	$\mathbf{WM}_{2C}$	$\mathbf{WM}_{1C}$
1	43.24 $\pm$ 30.95	39.10 $\pm$ 26.94	29.04 $\pm$ 22.55	23.76 $\pm$ 25.65
2	59.42 $\pm$ 23.11	54.85 $\pm$ 20.52	26.67 $\pm$ 12.12	25.27 $\pm$ 11.15
3	68.73 $\pm$ 40.44	61.44 $\pm$ 26.98	31.34 $\pm$ 27.25	25.77 $\pm$ 37.18
4	57.29 $\pm$ 43.93	52.82 $\pm$ 33.81	29.67 $\pm$ 34.99	33.15 $\pm$ 35.84
5	54.53 $\pm$ 33.31	46.94 $\pm$ 29.73	32.78 $\pm$ 26.12	28.96 $\pm$ 23.41
Total	56.64 $\pm$ 36.07	50.23 $\pm$ 26.65	28.30 $\pm$ 28.36	26.98 $\pm$ 29.71

Table 6.4.1: Absolute perfusion estimates in GM and WM (mean $\pm$ sd in [ml/100gr/min]), obtained with the Buxton model (1C) applied to the crushed dataset and the proposed two component model (2C) applied to uncrushed (NVC) dataset after that the macro vascular component has been estimated from the difference between the two datasets and used as a forcing function.

Pearson's correlation coefficients of perfusion estimates for both GM and WM tissue are reported in Tab. 6.4.2 for all the analyzed subjects. When considering the total distribution over all the subjects the estimates provided by the proposed two component model are highly correlated in both tissues (R^2_{GM} = 0.84, R^2_{GM} = 0.82).

The second main parameter that is affected by macro vascular artifacts is the arrival time in the micro vasculature (Δt_m). When the standard Buxton model is applied to NVC data it tends to exhibit low Δt_m values where a prominent quantity of vessels is expected, providing some kind of estimates of the arrival time in the macro vasculature. When vascular crushing gradients are used Δt_m provided from Buxton model is more reliable, and it is well correlated with the proposed two component model applied to NVC data. The macro vascular component can

Subject	$\mathbf{R}^2_{GM}$	$\mathbf{R}^2_{WM}$
1	0.84	0.77
2	0.84	0.84
3	0.81	0.88
4	0.77	0.73
5	0.98	0.97
Total	0.84	0.82

Table 6.4.2: Pearson's correlation coefficients between the perfusion estimates obtained with the standard Buxton model and crushed data versus the ones obtained by the proposed model on uncrushed data. Correlation coefficients have been reported separately for WM and GM.

also provide information on arrival time in the macro vasculature (Δt_a). This parameter is reported in the last row of Fig. 6.4.2 and it is displayed only where the macro vascular component provided reliable estimates. To assess the voxels where the macro vascular component was reliable a combined threshold on the coefficients of variation of all the four parameters below of 100% has been set. It is possible to note that the values of arrival time in the macro vasculature are lower than in the micro vasculature as expected and that the posterior circulation (fed principally by the basil artery) exhibits a longer time to reach the macro vasculature than the anterior ones.

The main parameter of the macro vascular component is the Arterial Blood Volume (aBV). The estimated spatial distribution of this parameter is reported for a representative subject in Fig. 6.4.3. This map shows only the voxel where the coefficient of variation of the all parameters estimated is below 100%. This has been set as a threshold for the goodness of fit (the same threshold used for Δt_a).

A typical example of the estimation procedure described is reported in Fig. 6.4.4 where the macro vascular component shows a detrimental effect on the tissue component, providing higher amplitude that can hamper perfusion estimates. It is possible to see how with no additional information the tissue component is very similar to the signal acquired

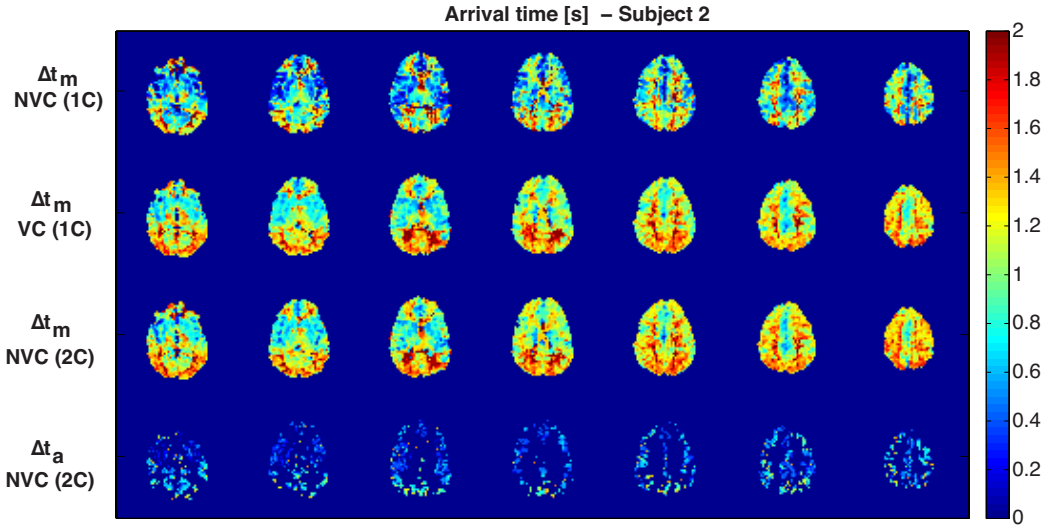

Figure 6.4.2: Arrival time in micro vasculature estimated by the Buxton model (1C) applied to the crushed (VC) and uncrushed (NVC) dataset and the proposed two component model (2C) arrival time in micro vasculature and macro vasculature when it is applied to uncrushed (NVC) dataset. The Δt_a estimated is reported on those voxels that support the data, based on a 100% threshold on coefficients of variation of each parameter of the macro vascular component.

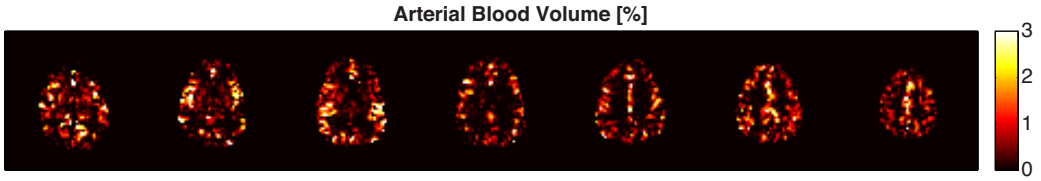

Figure 6.4.3: Arterial Blood Volume estimates obtained when the macro vascular component is fitted to the difference between crushed and uncrushed dataset.The aBV estimated is reported on those voxels that supports the data, based on a 100% threshold on coefficients of variation of each parameter of the macro vascular component.

using vascular crushing gradients (green crosses). Moreover it is possible to appreciate the difficult task that is required to retrieve both macro and micro vascular arrival time, using only the last samples of the whole curve since the first portion of the signal is employed for the labeling phase. Nevertheless, the goodness of fit is acceptable, according to the noise level, correctly estimated as prove the weighted residuals reported.

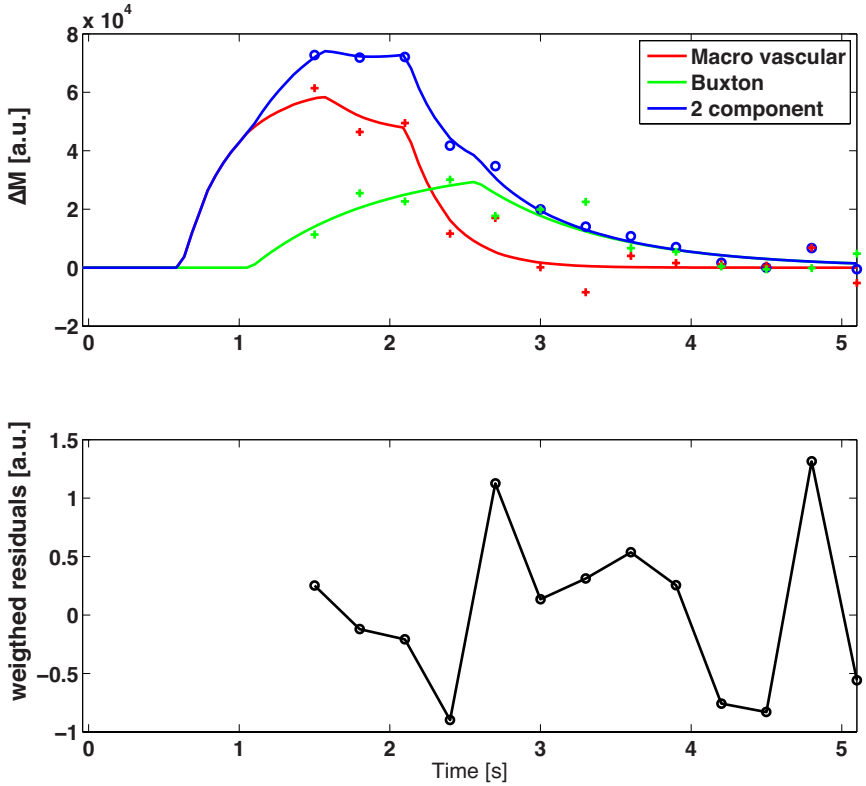

Figure 6.4.4: Example of fitting results of the two component model proposed. The first plot represents NVC dataset (blue circles) with the two component model fitted to it. VC acquired signal (green crosses) is displayed as reference for the tissue component (green solid line). The difference between NVC and VC dataset (red crosses) is reported to evaluate the goodness of the fit of the macro vascular model proposed (red solid line). The second plot reports the weighted residuals.

6.5 CONSIDERATIONS

Standard model estimation procedure has been redefined by adopting a Bayesian approach that can take into account the estimates of T_{1t} from a supplementary saturation recovery experiment. These new settings for standard model quantification have been applied to pCASL with vascular crushing (VC), and pCASL without vascular crushing (NVC). The Bayesian approach used has allowed to improve the model fitting to data, resulting in lower WRSS values compared with usual WNLLS approaches.

Considering parameters estimates, standard Buxton model has shown a markedly trend of overestimation in perfusion when NVC data are considered. The causes must be identified in the oversimplified description of the local tissue physiology assumed by standard model. GM brain tissue could not be represented by a single compartment in description of water exchanges: instantaneous and complete mixing between blood water and tissue water might be not appropriate (Parkes and Tofts, 2002). The voxel is characterized by a vascular tree that blood has to travel down before reaching capillary bed, where water exchange actually occurs. The single well-mixed assumption for tissue voxel became even more critical when large arteries are enclosed by the voxel, since a macrovascular artifact (a non perfusion contribution) is introduced into the measured signal.

Standard model perfusion estimates have shown a great improvement when data acquired with vascular crushing were considered. Estimates were acceptably placed inside the physiological range of normal perfusion values for healthy subjects. Vascular crushing thus permits to reduce discrepancies between the actual physiology reflected by measured signal and the assumptions made by the model. With the suppression of the signal for high flowing spins, only the contribution from tagged blood in capillary bed (or in proximity to capillary bed) gives rise to a detectable signal, as it flows with a velocity far below the cutoff velocity. In particular pCASL has shown to perform very well in combination with vascular

crushing application. The high SNR of pCASL has allowed to bear with the signal reduction involved by flow suppression gradients, providing good maps of perfusion estimates.

Also Δt has been estimated from data. This important parameter, used in pathology to complement information given by perfusion, showed a relevant increase when Buxton model was fitted to crushed data. This fact underlines the different meaning assumed by this parameter in dependance on the type of data set used. With uncrushed data, Δt reflects the transit delay from labeling creation to entrance into imaged voxel, while with crushed data Δt gives information about the transit delay from labeling region (or plane) to a level of voxel vasculature in proximity of capillaries. In pCASL data this parameter is difficult to extract since the initial part of the signal time course is not acquired (the coil is still employed for long labeling blood phase), and just few samples could be used to estimate it.

Buxton model describes tissue as a single well-mixed compartment in the description of water exchanges between blood and tissue. This quite simple description is a limitation on the model ability to provide reliable perfusion estimates. This fact has been discussed when perfusion estimates from data without vascular crushing have been shown. In brief, the simplicity characterizing standard model makes it sensible to intra vascular tagged blood signal, especially in a multi-TI experiment.

Several strategies have been developed to reduce this contamination, such as measurements at later TI to allow tagged blood to transit through arterial vessels, or the use of bipolar gradients to suppress the signal from fast flowing spins (mainly large arteries spins). Both these methods allow to improve the data description provided by standard model at the expense of an overall loss of signal, making SNR more critical. In the first case signal is reduced by the increased time allowed to relaxation of longitudinal magnetization of labeled blood. In the second case signal is reduced because a fraction of tagged spins is completely crushed (spins are dephased by bipolar gradients in the transverse plane, and cannot add coherently to give a net magnetization).

The correction of macrovascular artifacts by modeling approach described in section 6.3 is potentially more powerful than solutions that demand to sacrifice portion of the ASL signal. The two-component model is applicable with every labeling schemes, after a proper modeling of arterial component. The main disadvantage is that estimating the extra parameters associated with the arterial component may be detrimental to overall perfusion quantification. In particular, significant contributions from intravascular blood might only be expected in a limited number of voxels, reflecting the limited distribution of large arterial vessels in the brain. In the absence of true arterial signal, this component of the model might fit erroneously noise or a fraction of the perfusion signal, leading to overfitting and confounding effects on tissue perfusion estimates (Chappell et al., 2010). The problem of best model selection has not been addressed. Efforts have been made to extract a plausible model for arterial component, and to show the potential ability of the two-component model to eliminate macrovascular artifacts, restoring perfusion values to those obtained from the fitting of standard model to VC data. The main difficulties reside in detecting the right timing and amplitude of arterial component to properly correct the tissue component data fitting.

Macro vascular component model has been derived starting from the ideal profile of labeled bolus transit into an artery. Destructive effects introduced by acquisition scheme, dispersion and relaxation processes of the labeled tracer magnetization have been modeled by means of appropriate function, previously proposed in dynamic angiography studies based on pCASL tagging scheme. In particular, dispersion of labeled blood has been taken into account using a gamma shape kernel, since a previous study (Chappell et al., 2013a) indicated it as the best model for dispersion occurring in large arteries. Several assumptions have been made on the function describing the effects of Look & Locker readout scheme on arterial component model. First of all, the dependance of this function on dispersion effects was neglected. Then, the additional parameter required, δt_{min}, has been estimated voxel wise from the first slice and only from the most reliable voxels. In pCASL, labeling of blood is

performed on time. This implies that the labeled blood bolus does not experience Look & Locker readout pulses in the same manner: the final part of bolus experiences more RF pulses. A precise evaluation of the number of RF pulses experienced by labeled blood in time requires knowledge of transit time from labeling region to imaging region, i.e. parameter δt_{min}. Taking an approximated value for δt_{min} could be very detrimental since the portion of model sensitive to δt_{min}, is the portion sampled by acquisition scheme. Thus, a complex model requires to be fitted to a set of samples that span the time course just partially, in a temporal window where there is a strong dependence from an unknown parameter.

It could be noted that a very complex arterial component model has been used in combination with a relatively basic tissue component model, i.e. the Buxton model. The rationale of the method was to correct standard model perfusion estimates by adding a new component, so effort has been made on the arterial side of the model, leaving tissue component unchanged. However, parameters describing dispersion could be measure more easily in large arteries than tissue, using for example ASL based angiography techniques. Adopting the arterial component model (Eq. 6.20) as macro vascular contribution in the two component model (Eq. 6.15) is a viable solution to reasonably describe data with marked macro vascular artifacts, and allows to restore perfusion estimates into a physiological range of values, at least comparable with those calculated using crushed data. The addition of numerous parameters to the estimation leads to higher variance in the estimates in both GM and WM. Nevertheless the estimates on perfusion and arrival time in the micro vasculature are highly correlated to the ones obtained with the standard Buxton model.

The Bayesian framework that has been implemented it is possible to estimate the precision of the estimates in term of coefficients of variation (CV). These estimates have been evaluated in all the subjects analyzed. In Fig. 6.5.1 CV maps of a representative subject have been reported. They display an acceptable range of values for perfusion, arrival time in the microvasculature and T_1 decay of tissues. WM CV estimates shows

higher values respect to GM due to the low SNR. It is worth noting that GM exhibits spots of augmented CV corresponding to areas of where the macro vascular component is present. This means that the two compartment model, having more parameters, can introduce a higher variance in the estimates. This is confirmed also from CV of the aBV, that show very high values in correspondence to low value of the parameter. This is reflecting the fact that the model is trying to fit something that is not supported by the data.

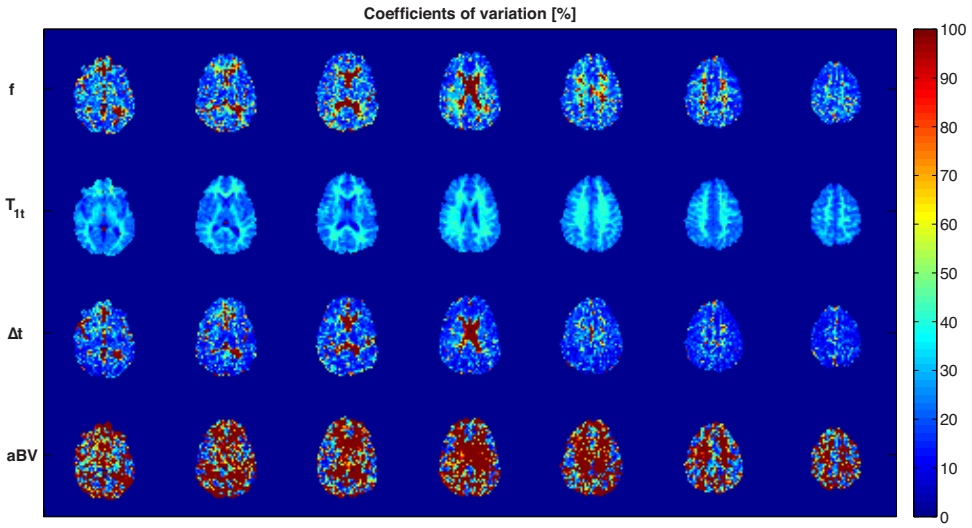

Figure 6.5.1: Coefficient of variations ($\%$) of parameters estimated in the last step using the two component model. The first row reports perfusion CV. T_{1t} CV estimates using a prior on it retrieved from the saturation recovery acquisition are reported in the second row. Δt_m CV are reported in the third row. aBV CV are reported in the fourth row, showing high value in correspondence of very low aBV estimates.

Another limitation might reside in the acquisition of the dataset. The flip angle used (35°) can enhance the macro vascular artifacts and suppress the magnetization of the residual micro vascular component. Further investigations are required to enlarge the cohort of subjects and to explore more reliable readout approaches such as variable flip angle to take into account the shape of the kinetic curve and to regolate the acquired SNR in consequence.

It is no good to try to stop knowledge from going forward. Ignorance is never better than knowledge.

Enrico Fermi

7

In-vivo automatic labeling efficiency estimation

Labeling efficiency plays a critical role in perfusion quantification from ASL data as it has been already presented in section 3.1.5. Expecially for pCASL acquisitions it depends on factor whose entity shows both inter and intra-subject variability, making numerical simulations an inappropriate tool to assess its value. For these reasons, the most appropriate way to take inversion efficiency into account is to directly estimate it from data. In Aslan et al. (2010) a method for in vivo determination of inversion efficiency in pCASL experiment is proposed. The idea underlying this method is to obtain two measures of total perfusion (or whole-brain perfusion) of the same subject in the same physiological state, in which one measure does not require any inversion mechanism, and the other is consequence of inversion pulses application. Namely, the two measurements are performed respectively with phase-contrast

(PC) MRI, and pCASL techniques. pCASL, and in general ASL techniques, estimate total perfusion (whole-brain perfusion) using information originated by blood flow in capillaries, by averaging the local perfusion measures over the whole brain. PC quantifies total perfusion using a global approach, measuring the blood flow in the brain feeding-vessels and normalizing this value by the whole-brain mass extracted from a high-resolution anatomical image. PC-MRI technique has been shown to provide reliable measurements of total perfusion both in term of accuracy and reproducibility (Spilt et al., 2002). Ideally, these two methods must give the same total perfusion measure. The discrepancy is due to the unknown labeling efficiency, which can be isolated from the ratio of the two total perfusion measures exploiting the global scaling role played by labeling efficiency in perfusion estimation from pCASL data. In Aslan et al. (2010) the normalization factor provided by PC for labeling efficiency estimation is evaluated using a manual procedure that consists in vessel contours delineation in PC images performed by an expert operator. Here a in vivo labeling efficiency estimation using PC-MRI images is performed by means of a completely automated procedure which aims at reducing the long time required by the previously proposed manual analysis method, and at avoiding any inter- and intra-observer variability, improving both accuracy and reproducibility of labeling efficiency estimation, and consequently of perfusion estimation. All these steps are built in a completely automatic pipeline of analysis, named Automatic Tool for Labeling Efficiency eStimation (ATLES).

7.1 ATLES: A NOVEL AUTOMATIC PROCEDURE FOR LABELING EFFICIENCY ESTIMATION

As proposed by Aslan et al. (2010) labeling efficiency is estimated in vivo using phase-contrast (PC) images by the independent estimation of three quantities:

- the total brain blood flow ($\mathbf{F}_{tot}$) from PC image

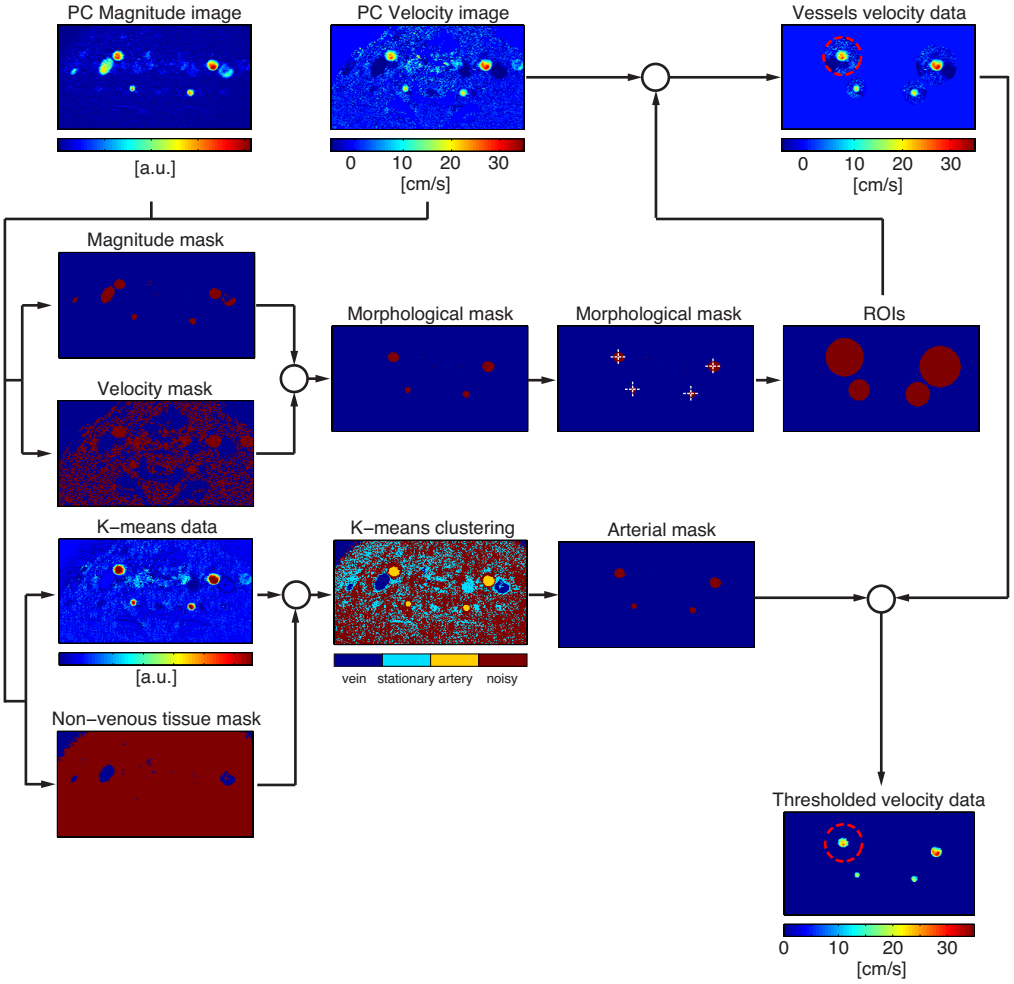

Figure 7.0.1: ATLES pipeline: Phase Contrast magnitude image is thresholded using Otsu's algorithm (Otsu, 1979) to extract the background. Then phase images are thresholded to take into account only positive values (excluding venous signal) and combined with the raw mask created on the magnitude image. The morphological mask with the feeding artery is obtained and used to estimate the center of the vessels. Afterwards ROIs are used to define the research domain of the non linear least square estimator to be used with a laminar flow model. In parallel a K-means cluster algorithm is applied on the velocity image with masked venous flow and the cluster providing the higher mean velocity value is extracted. The arterial mask is then used to not consider voxels of PC image not classified as artery in the fitting procedure.

- the brain mass ($\mathbf{M}_b$) from anatomical reference, in this implementation a T_1-weighted image
- the average whole-brain perfusion uncorrected for labeling efficiency (${}^{unc}\mathbf{f}_{pCASL_{tot}}$) from pCASL images

For each of these quantities, robust and user-independent methods for quantification have been developed.

7.1.1 Quantification of total brain blood flow using Phase Contrast

Under the following conditions:

- PC acquisition plane is perpendicular to imaged vessels
- PC acquisition plane intersects all the brain-feeding vessels, and all imaged vessels are destined to perfuse the brain
- maximum encoded velocity is higher than maximum velocity inside imaged vessels

PC images can be used for total brain blood flow quantification. It simply requires the integration of velocity estimates, provided by PC velocity image, over the cross section of every imaged vessel. This operation is performed automatically with the procedure described below.

The analysis of PC images for $\mathbf{F}_{tot}$ determination is basically divided in two steps:

1. Localization of brain-feeding vessels in PC image
2. Quantification of blood flow, in unit of [ml/min], of each imaged vessels

Region-of-interests that encompass the imaged vessels are easily identified exploiting the high contrast provided by the PC magnitude image. After the exclusion of non-tissue voxels, a threshold on the normalized PC magnitude image is used to select vessels structures. This threshold

is set to the value that maximize the interclass variance of the vessels and non-vessel groups of voxels (Otsu, 1979). Afterwards, only voxels with positive values in PC velocity image are kept, to discard venous voxels. Isolated voxels, and very small structures are excluded from the analysis. In particular, are considered only the connected groups of voxels with an estimated region diameter higher than $1\ mm$ (Krejza et al., 2006; Mitchell and McKay, 1995) as brain-feeding vessel. Finally, to delineate circular ROIs that encompass the entire vessel and a portion of surrounding tissues, the estimated diameter of each connected group is increased by a factor of 3. In each ROI, the blood flow inside the considered vessel is evaluated using a model-based approach. Two assumptions are made: a vessel can be thought as a cylinder perpendicular to the imaging plane, i.e. the vessel has a circular section in PC images and blood flow follows a laminar law, i.e. velocity profile in every vessel section is parabolic. These assumptions require imaging plane of PC acquisition to be placed perpendicular to brain-feeding vessels, and far enough (few centimeters) to any vessels bifurcation, so that each imaged vessel can be characterized by a circular section and a fully developed steady parabolic profile in PC images. According to these two assumptions, blood velocity, $v(x, y)$, in a specific voxel contained in the selected ROI, can be described by:

$$v(x,y) = \begin{cases} v_{max}\left[1 - \frac{(x-x_c)^2+(y-y_c)^2}{R^2}\right] & (x-x_c)^2 + (y-y_c)^2 \leqslant R^2 \\ 0 & (x-x_c)^2 + (y-y_c)^2 > R^2 \end{cases} \tag{7.1}$$

where v_{max} is the maximum velocity inside the vessel in $[cm/s]$, x_c and y_c are the coordinates of vessel center, and R is vessel radius in $[cm]$. Eq. 7.1 is commonly known as the Poiseuille's law for laminar flow (Sutera and Skalak, 1993), and it is characterized by time-independence and axial symmetry. From this model, blood flow of the considered vessel, $\mathbf{F}$, can be evaluated by the integration of velocity values over the section of the

vessel. This integral is resoluble analytically:

$$F = \int_A v dA = \frac{v_{max}}{2} \cdot \pi R^2 \tag{7.2}$$

The total brain blood flow, $\mathbf{F}_{tot}$, is obtained by adding the blood flow measurements evaluated in each vessel identified:

$$\mathbf{F}_{tot} = \sum_{i=1}^{N_{vessels}} F_i = \frac{\pi}{2} \sum_{i=1}^{N_{vessels}} v_{max} \cdot R^2 \tag{7.3}$$

where $\mathrm{N}_{vessels}$ is the number of vessels identified in the PC images. Eq. 7.3 shows that the quantification of F_{tot} from PC velocity image requires the knowledge of the maximum velocity v_{max}, and the radius R of each imaged vessel. These parameters are estimated by fitting the model (Eq. 7.1) to velocity data in each selected ROI, through a non-linear least squares (NLLS) estimator. The fitting procedure is preceded by a pre processing step to confer more stability to the parameters estimation. Data z_j used in minimization of **J** are not all the measured velocity data. A selection step, accomplished by means of an automatic procedure, is performed prior to model parameters estimation with the aim of reducing partial volume effects, slow flow artifacts and noise contribution in parameter estimation, achieving a more stable fitting procedure. The selection is made by a clustering method applied on magnitude data weighted by velocity data sign, after the exclusion of veins structure and non tissue voxels. K-means clustering method is used, and three clusters are expected, representing stationary tissues, noisy and interface (edge or border) voxels and arteries. Clustering procedure is iteratively repeated to ensure the reproducibility of the final classification. The selection of the arterial cluster is made automatically by choosing the cluster with the higher mean velocity. Only velocity data individuated by the arterial cluster are kept to their original value in parameters estimation, while velocity data outside that cluster (within the considered ROI) are set to zero. The optimal parameters values are those which minimized the cost function **J**, given by the weighted sum of squares difference between model

prediction v_j, and velocity data z_j:

$$J = \sum_{j=1}^{N} [w_j(z_j - v_j)]^2 \tag{7.4}$$

where N is the total number of voxels considered by the selected ROI, and w_i are the weights associated to each measure. In the model proposed the weight of each measure is uniform and constant, i.e. each measure has the same weight. Minimization of J is performed with a MATLAB tool for optimization of nonlinear cost functions, which requires a set of initial points for the parameters to be estimated. Initial points are extracted using the properties of each ROI previously defined: the estimated center of the region as coordinates of the center of vessel x_c and y_c, the velocity value in the center of the region as peak velocity v_{max}, and the estimated radius of the vessel estimated in the pre evaluation analysis of each single connected component. Finally, a post-processing step is performed prior to $\mathbf{F}_{tot}$ calculation by Eq. 7.3, to exclude spurious vessel structures that automatic procedure for vessel localization did not discard. A combined analysis, that accounts for CV of parameter estimates and simple physiological considerations regarding number of vessels and their geometry and symmetry, is used to ensure that only vertebral and internal carotid arteries are considered in $\mathbf{F}_{tot}$ calculation. CV threshold has been set to 100 $\%$.

7.2 Intracranial mass estimation

The whole-brain mass (or intracranial mass), $\mathbf{M}_b$, is obtained by the product of intracranial volume, V_b, (obtained summing CSF, GM and WM volumes) with an average density value for brain tissue ρ_b, equals to 1.06 g/ml (Herscovitch and Raichle, 1985). In particular, V_b is extracted from a high resolution T_1-weighted acquisition using a specific tool for brain extraction, called BET, included in FSL (Jenkinson et al., 2012; Smith, 2002). Several options can be set prior the application of this tool, to remove contamination of neck and eyes regions in brain edges determination and to

reduce the bias on the final result due to the unknown coordinates of the brain center. An iterative procedure to ensure that all these aspects are kept into account has been built. The final brain mask is computed from three masks obtained separately from BET ran with each option and then combined by AND logical operator. The optimal choice of BET parameters in each options settings is defined on the basis of a previous study (Popescu et al., 2012).

7.3 Reliable whole brain perfusion estimation

A measure of whole-brain perfusion can be obtained from pCASL images, by averaging over the whole brain volume the voxel-wise perfusion estimates provided by quantification of ASL data. Firstly, pCASL data is converted into perfusion map through a fitting procedure, using the Buxton model adapted for pCASL (Eq. 4.5). The parameters to be estimated are as usual perfusion (**f**) and arrival time in micro vasculature (Δt). T_{1t} is calculated by fitting the incomplete saturation recovery model ($S(t) = M_{0t}(1 - Ae^{-t/T_1 t})$) to the data acquired with saturation recovery experiment, M_{0b} is calculated using the common relation $M_{0b} = M_{0t}/\lambda$ to obtain a voxel-wise M_{0b} value able to correct both for variable coil sensitivity and field inhomogeneities.

However, the quantification procedure of pCASL images is slightly modified, as the labeling efficiency is unknown. Labeling efficiency α is coupled with **f**, to form the voxel-wise **f** uncorrected for labeling efficiency:

$$\mathbf{f}^{unc} = \alpha \mathbf{f} \tag{7.5}$$

In Eq. 4.2, the apparent longitudinal relaxation time for tissue ($T_{1t,app}$) follows the usual rule: $1/T_{1t,app} = 1/T_1 t + \mathbf{f}/\lambda$. Thus, this parameter can be estimated from data using LS approach, after that the dependence of $1/T_{1t,app}$ on **f** is eliminated. This can be accomplished by fixing **f** to a plausible value, i.e. the mean value for gray matter $\mathbf{f} = 0.01\ ml/g/s$, in

the expression for $T_{1t,app}$, at the expense of a negligible bias in the final estimate, since the term $\mathbf{f}/\lambda$ is dominated by $1/T_{1t}$. This expedient allows the voxel-wise calculation of $\mathbf{f}^{unc}$, using a model fitting approach. Afterwards, averaging $\mathbf{f}^{unc}$ estimates in every voxel within brain volume, the average whole-brain $\mathbf{f}$ uncorrected for labeling efficiency (${}^{unc}\mathbf{f}_{pCASL_{tot}}$) is obtained. However, if all the voxels contained in the brain tissue mask are considered in the averaging procedure, a bias is expected to be introduced, due to partial volume effects, imperfections in brain tissue mask definitions and non reliable estimates resulted from non-linear estimation. A robust averaging procedure for ${}^{unc}\mathbf{f}_{pCASL_{tot}}$ evaluation is defined, exploiting the degree of estimates reliability described by the CV, provided as output by the parameters estimation. Thus, the CV distribution of $\mathbf{f}^{unc}$ estimates is fitted to a skew-t distribution (Azzalini, 2005) with 1 degree of freedom (i.e. a skew-Cauchy distribution). The initial points for parameters of distribution (location, scale and shape) are chosen among a pool of possible candidates values determined experimentally through some initial fitting experience. Then the best fit is chosen based on calculation of the root sum of squares of residuals. A threshold on the fitted distribution is placed at the 95^{th} percentile, and the group G of voxels whose CV value is below that threshold is defined. Finally, ${}^{unc}\mathbf{f}_{pCASL_{tot}}$ is obtained averaging values of all the voxels contained in G:

$$
\begin{aligned}
{}^{unc}\mathbf{f}_{pCASL_{tot}} =& 6000\frac{1}{N_G}\sum_{i\in G}\mathbf{f}^{unc} = 6000\frac{1}{N_G}\sum_{i\in G}\alpha\mathbf{f}_i = 6000\alpha\left(\frac{1}{N_G}\sum_{i\in G}\mathbf{f}_i\right) && (7.6)\\
=& 6000\alpha\mathbf{f}_{pCASL_{tot}} && (7.7)
\end{aligned}
$$

where the factor 6000 represents the conversion factor needed to obtain absolute perfusion values from $[s^{-1}]$ to $[ml/100g/min]$, and α is a global parameter that can be extracted from the sum. As described by Aslan et al. (2010), the two measures of total perfusion provided by ASL and

PC techniques should be the same, and thus:

$$\mathbf{f}_{PC,tot} = \mathbf{f}_{pCASL_{tot}} \rightarrow \frac{\mathbf{F_{tot}}}{M_b} = \frac{\mathbf{f}^{unc}_{pCASL_{tot}}}{\alpha} \tag{7.8}$$

labeling efficiency can be estimated by the ratio:

$$\alpha = \frac{\mathbf{f}^{unc}_{pCASL_{tot}}}{\frac{F_{tot}}{M_b}} \tag{7.9}$$

where the tree fundamental quantities that enter in its estimation (total whole-brain perfusion uncorrected for labeling efficiency, total brain blood flow and brain mass) are calculated with the automatic methods previously described.

7.4 REAL DATASET

Acquisitions were performed on a Philips 3T Achieva MR scanner. Seven healthy subjects (26 ± 3 years) underwent the same protocol, after they had given informed consent. The acquisition protocol was composed by: a static non-triggered single slice phase-contrast (PC) image, high-resolution 3D T_1-weighted acquisition, and multi-TI pseudo-Continuous Arterial Spin Labeling session. PC acquisition was performed oriented perpendicular to the major brain feeding arteries (Fig 7.4.1). It was preceded by a time-of-flight (TOF) angiography scan to visualize the anatomy of the feeding vasculature proximal to the brain and optimize the localization of PC acquisition plane. PC MRI parameters used were: voxel size of $0.45 \times 0.45 \times 5\ mm^3$, flip angle $15°$, maximum encoding velocity of $80\ cm/s$, for a total scan duration of about 40s. High-resolution 3D T_1-weighted acquisition was performed with an isotropic voxel dimension of $1 \times 1 \times 1\ mm^3$, repetition time/echo time of $9.88\ ms$ / $4.59\ ms$, flip angle $8°$, to allow a precise evaluation of brain volume and mass.

ASL data acquisition was performed combining a balanced pseudo-Continuous labeling scheme with single shot multi-slice 2D EPI readout repeated at seven different post-labeling delays, equally spaced in time

Figure 7.4.1: Typical slice positioning of Phase Contrast sequence based on Time of Flight angiography.

from $100\ ms$ to $1800\ ms$. ASL sequence parameters were: labeling duration of $1.8\ s$, voxel size of $3 \times 3 \times 4\ mm^3$ with an inter slice gap of $0.5\ mm$, a total number of 22 slices acquired in ascending order, and per slice acquisition time of $38\ ms$. ASL data SNR was improved averaging 30 pairs of label/control images, while to avoid macro-vascular artifacts in the measured signal, vascular bipolar crushing gradients were applied (only on z-axis) with a cut-off velocity of 4 cm/s. After ASL session, a saturation recovery experiment was performed with 10 sampling points, equally spaced from $100\ ms$ to $1900\ ms$, with the same imaging parameters of ASL sequence, to allow the estimation of the longitudinal relaxation time (T_{1t}) and equilibrium magnetization of blood (M_{0b}) required for ASL quantification.

7.5 Results

Vessels parameters are estimated fitting the blood velocity model to the data individuated by the ROIs automatically defined. Four ROIs have been automatically extracted in all subjects analyzed, indicating left, right internal carotid (L-R ICA) and vertebral arteries (L-R VB). In Tab. 7.5.1, radius and maximum velocity estimates are reported for the 4 vessels of each subject. Considering internal carotid arteries average radius exhibits $3.15 \pm 0.3\ mm$ and average peak velocity $35.84 \pm 4.5\ cm/s$, while for

vertebral arteries average radius found was $1.64 \pm 0.4\ mm$ and an average peak velocity of $24.51 \pm 4.6\ cm/s$ has been estimated.

Subject	Left ICA		Right ICA		Left VB		Right VB	
	R $[mm]$	$\mathbf{v}_{max}$ $[cm/s]$	**R** $[mm]$	$\mathbf{v}_{max}$ $[cm/s]$	**R** $[mm]$	$\mathbf{v}_{max}$ $[cm/s]$	**R** $[mm]$	$\mathbf{v}_{max}$ $[cm/s]$
1	2.88	34.2	2.82	36.1	1.18	15.8	1.90	27.0
2	3.63	37.2	3.22	37.1	1.83	30.2	1.11	23.9
3	3.09	36.6	3.09	35.9	1.71	24.4	1.88	27.8
4	2.83	46.7	3.11	35.4	0.95	23.9	1.91	35.6
5	3.45	27.1	3.72	31.3	1.88	22.7	2.20	22.0
6	3.15	41.1	3.35	33.3	1.47	20.7	2.13	23.7
7	3.00	34.4	2.72	35.3	1.41	22.0	1.47	23.5
Mean	3.15	36.8	3.15	34.9	1.49	22.8	1.80	26.2
Sd	0.29	6.1	0.33	2.0	0.34	4.3	0.38	4.6

Table 7.5.1: Radius R and maximum velocity v_{max} estimates for each vessel (Right / Left Carotid and Vertebral arteries) with the proposed model.

A typical example of model fitting for internal carotid artery is shown in Fig. 7.5.1. Waveforms along different sections obtained with nontriggered PC (black points) are reported with model prediction (in red) and considered data in the fitting procedure obtained by K-means clustering (blue circles). The post-processing analysis of estimation results, built to discard spurious ROIs fit, was essential in 2 of the 7 subjects, where, 2 ill-defined ROIs have been included in the vessel set by the K-means clustering. The post-processing criteria successfully discard all the ill-defined vessels.

In Tab. 7.5.2, the three main quantities required for labeling efficiency estimation are reported for each subject. In the group of healthy controls studied, the average total blood flow to brain (F_{tot}) is $803 \pm 121.1\ ml/min$, the average intracranial mass (M_b) that has been estimated is $1640.2 \pm 204.3\ g$ and the average whole-brain **f** uncorrected for labeling efficiency (${}^{unc}\mathbf{f}_{pCASL_{tot}}$) is $42.4 \pm 4.1\ ml/100g/min$. Average labeling efficiency between subjects is 0.867 ± 0.03.

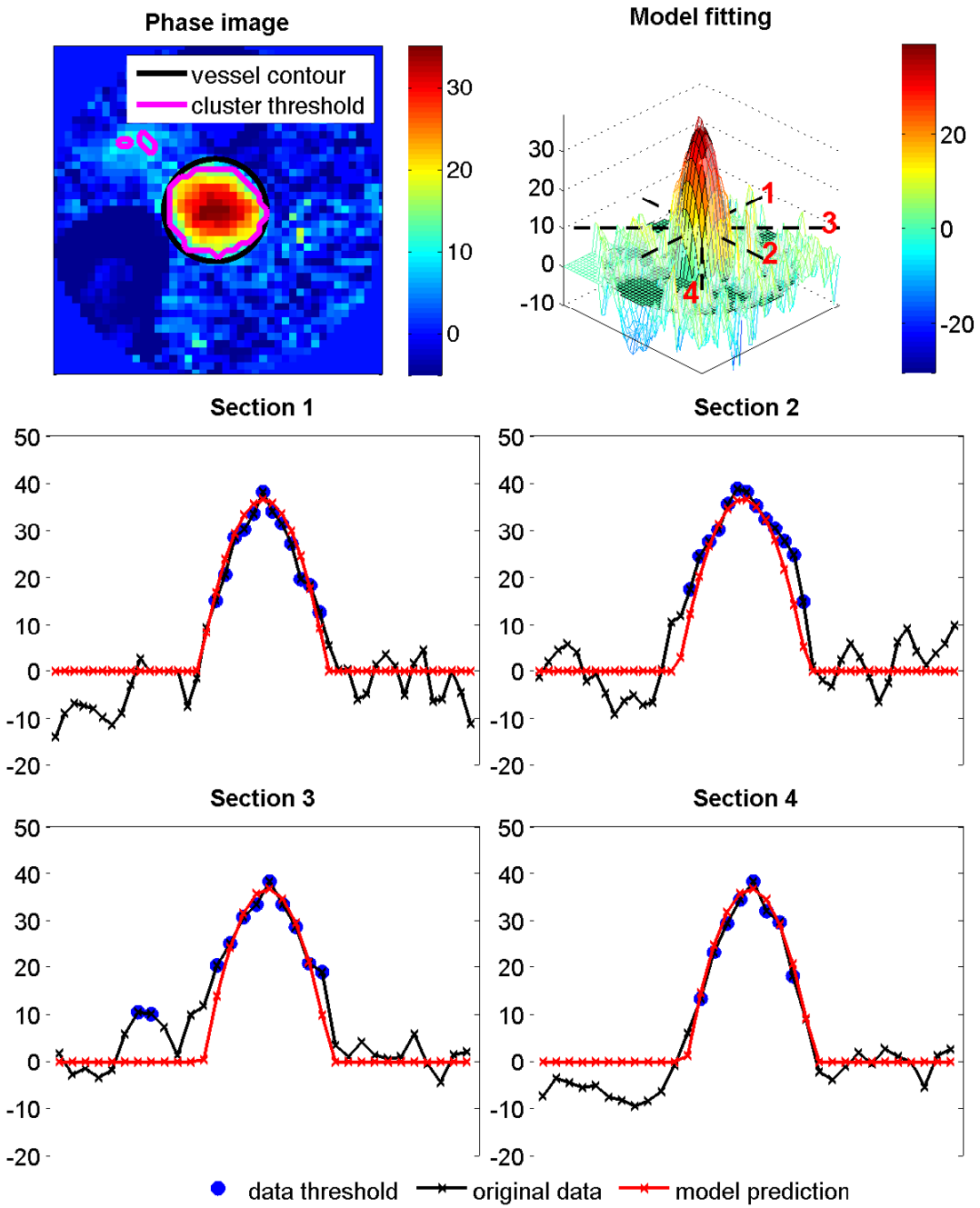

Figure 7.5.1: Typical model fitting result obtained from L-ICA of subject #6. The phase image with estimated vessel contour and clustering threshold used to weight the data are reported in the image at top left. Four major sections are reported to evaluate the goodness of the fit of model prediction (red line) versus data considered in the fit (blue circles). The original data, before the selection procedure operated by clustering, are also reported (black line). The domain of possible values, estimated from the morphological mask calculated from the data, are represented by the outer circles on the phase image.

Subject	$\mathbf{F}_{tot}$ $[ml/min]$	$\mathbf{M}_b$ $[g]$	${}^{(unc)}\mathbf{f}_{pCASL_{tot}}$ $[ml/100g/min]$	α $[\%]$
1	651.7	1533.5	37.3	0.88
2	946.3	1802.5	43.6	0.83
3	814.2	1484.3	46.6	0.85
4	816.0	1569.1	48.0	0.92
5	888.2	1739.3	42.8	0.84
6	879.8	1968.5	37.9	0.85
7	626.8	1383.9	40.6	0.90
Mean	803.3	1640.2	42.4	0.867
Sd	121.1	204.3	4.1	0.03

Table 7.5.2: Parameters needed to quantify the labeling efficiency in vivo, following the method proposed by Aslan et al. (2010), i.e. total brain blood flow ($\mathbf{F}_{tot}$), brain mass ($\mathbf{M}_b$) and the average whole-brain perfusion uncorrected for labeling efficiency (${}^{unc}\mathbf{f}_{pCASL_{tot}}$).

Average gray matter (GM) and white matter (WM) perfusion have been evaluated in tissue type masks composed by N=1000 voxels. Those masks are provided by the FAST tool for brain segmentation (Zhang et al., 2001), applied on the T_1-weighted images after the co-registration with the R_{1t} estimated map from saturation recovery experiment in a procedure similar to the one used for QUASAR data in section 5.2.3. For the co-registration step the Advanced Normalization Tool (ANTS) (Avants et al., 2011) has been employed. The voxels have been ranked according to their tissue type probability (provided by the segmentation tool), and the first 1000 were considered in the averaging, as representatives of pure tissue type voxels. Average GM and WM perfusion is respectively $49.66 \pm 5.87\ ml/100g/min$ and $26.51 \pm 3.33\ ml/100g/min$, with an average ratio GM-to-WM of 1.89 ± 0.3.

7.6 Considerations

A novel automatic tool (ATLES) has been proposed. It is an evolution of the work proposed by Aslan et al. (2010) and it uses a completely auto-

Subject	$\mathbf{f}_{GM}$ $[ml/100g/min]$	$\mathbf{f}_{WM}$ $[ml/100g/min]$
1	41.5 ± 41.1	27.8 ± 47.5
2	60.9 ± 66.9	30.6 ± 43.5
3	51.3 ± 44.4	26.8 ± 18.6
4	48.0 ± 36.6	22.9 ± 21.7
5	50.4 ± 49.1	21.1 ± 21.1
6	50.4 ± 49.1	28.4 ± 22.4
7	48.4 ± 34.9	28.4 ± 22.4

Table 7.5.3: Perfusion estimates from the multiTI pCASL (mean and SD), corrected with the in-vivo labeling efficiency estimated using ATLES.

matic procedure to estimate labeling efficiency of ASL acquisitions. The method proposed by Aslan et al. (2010) to estimate in vivo labeling efficiency is based on the extraction of a normalization factor for perfusion estimates using a non-triggered 2D PC-MRI acquisition. Non-triggered single slice phase contrast acquisition is a very flexible tool, as it has a straightforward implementation (avoiding triggering problems of the gated acquisition), and does not require long scanning time to assess total blood flow (about 30-40s). In Spilt et al. (2002) non-triggered 2D PC has been demonstrated a reliable method to assess total cerebral blood flow in terms of both accuracy and reproducibility. A relative error lower than 11% was found in measurements obtained in a phantom, and the CV of repeated total perfusion measurements was lower than 11%, with non-triggered PC. These findings have suggested that non-triggered 2D PC is as accurate as triggered PC to assess blood flow in weakly pulsatile vessels (as internal carotid and vertebral or basilar arteries), and thus in that cases it should be preferred to gated PC because of its appealing properties. Other studies have shown that when pulsatile effects become more prominent, non-triggered 2D PC loses its accuracy. Pulsatility causes image artifacts that can result in errors in the velocity determined. These errors depend on the actual velocity time function and the acquisition parameters (Hofman et al., 1993). The estimation of labeling efficiency implemented as proposed by Aslan et al. (2010) consists in

a manual segmentation of vessels that contribute to perfuse brain tissues. This step might be a limiting factor to the application of this method, especially to large datasets. For this reason, an automatic method to extract vessels from PC images that combine clustering techniques and automatic threshold determination has been proposed. Furthermore a model-based approach is also proposed to estimate the effective total flow. This method is developed and tested on a healthy controls cohort. Being completely automatic, this method can be applied to large datasets without the necessity to employ trained people. Thus, the reproducibility of the method is guaranteed by its intrinsic property: no interaction with the user is required. Moreover a check in presence of outlier in any of the estimated parameters (diameter of the vessels or maximum velocity) could provide a metric to exclude problematic subjects.

The fitting procedure of the PC phase images with the laminar flow model proposed, requires the definition of a weight for each available measure. Three weights types have been tested and the final model used was a uniform weight for each measure. This is a trade-off between weights proportional or inversely proportional to the data. The former provided an overestimated vessels radius, driven by the higher values present in the center of the vessels. The latter overestimated the maximum velocity of the vessels.

Providing that PC images have been acquired properly (perpendicular to feeding vessels, and with optimal parameters), the model-based approach for total blood flow quantification relies on two main assumptions: vessels have circular shape cross-section, and blood velocity has a parabolic profile. The first assumption is generally accepted in the context of intra- and extra-cranial circulation (brain and neck region), where the arteries are smaller and subjected to lower pulsatiliy effects and strain fields. In normal condition, the second assumption is generally adopted in the description of intra- and extracranial circulation, where the pulsatility properties of blood motion can be ignored (Bakker et al., 1996). Neglecting the pulsatile behavior of blood flow, a fully developed steady laminar flow can be ideally encountered, when acquisi-

tion plane is placed far enough from a vessel bifurcation (the distance is function of Reynolds number and vessel diameter), so that the portion of vessel imaged can be considered as a straight tube. In this flow regime, blood velocity inside vessels follows the parabolic profile, described by Poiseuille law (Sutera and Skalak, 1993).

Waveforms along different sections obtained with non-triggered PC demonstrate the validity of the model choosen for blood velocity description (Fig. 7.5.1). The parameter estimation has been repeated several times with different initial points for vessel center coordinates (x_c and y_c) and maximum velocity (v_{max}), to evaluate the influence of local optimum of the cost function in the final results. However, the fitting procedure resulted to be highly stable to variations up to $\pm 20\%$ of initial values, automatically determined, of those parameters.

The Buxton model is considered as the standard approach for voxel-wise quantification of perfusion with multi-TI ASL data, and has been proved to provide reliable perfusion estimates when used in combination with vascular crushing for suppression of macro-vascular artifacts. In the implemented version of Buxton model a fixed value of $0.01 s^{-1}$ of **f** has been introduced in the definition of the T_{1eff} . This modification has a very low impact on perfusion quantification ($< 5\%$) providing more stable fit results (Xie et al., 2008). Results of labeling efficiency estimated by ATLES are in agreement with both simulated and real data (Aslan et al., 2010; Dai et al., 2008) suggesting that this method might be applied to a larger cohort reducing the time needed to complete the analysis. The mean vessels radius are in agreement with literature values for carotid arteries (Krejza et al., 2006). A major variability has been found for vertebral arteries: showing lower mean diameter and higher standard deviation compared to carotid arteries and giving slightly higher values than literature (Mitchell and McKay, 1995) This might be caused by the relatively low in-plane spatial resolution (0.45x0.45) respect to vertebral arteries size. The total flow values observed and reported in Tab 7.5.2 are in agreement with previous studies (Spilt et al., 2002).

Intracranial mass estimation was accomplished using an iterative pro-

cedure (Popescu et al., 2012). T_1 anatomical reference might be suboptimal since both CSF and skull are partly dark. A combined approach to include also T_2 measurements will be addressed in further investigation.

Introducing a method to completely automatically estimate labeling efficiency is very useful because it can provide a subject specific scale factor that can incorporate subject variability and might reduce the variance in perfusion estimation in large datasets. However, it is of note that this estimation is derived from 3 different quantitative steps. Respectively a measure of total flow (PC non-triggered) that has shown to be reliable and reproducible has been employed, an estimation of total intracranial mass from T_1 high-resolution images and tissue perfusion provided with multi-TI ASL has been used. Each of these measurements have an estimation error. And each of them will contribute to scale errors in the estimation of labeling efficiency. Outliers in the population of each of the estimates that contribute to the labeling efficiency calculation should be carefully taken into account.

This method is very flexible, requires only 40 seconds of additional scanning time and can be applied to every ASL scheme: interesting possible applications of this method would involve vessel encoded ASL (Okell et al., 2013) or super selective ASL (Hartkamp et al., 2013). Theoretically it is possible to extract the total mass of tissues fed by a single artery and thus it could be possible to apply this approach also to a single vessels. In the light of the validation of the vessel segmentation step, future investigations will include also ASL modalities that can extract information on feeding territories.

To conclude phase contrast acquisitions provides a measure of total brain blood flow that can be used to scale quantitative perfusion estimates with ASL, by estimating the actual labeling efficiency. An automatic version of phase contrast normalization methods for labeling efficiency in vivo estimation (ATLES) is presented. The proposed tool is completely automated, and thus less time consuming. Moreover, it does not suffer from operator-dependent errors and can be used to perform quantitative comparison of results between different ASL studies.

It's a dangerous business
going out your front door.

J. R. R. Tolkien

8 Conclusions

The quantitative knowledge of the blood brain perfusion is of fundamental importance not only to understand the physiological mechanisms acting in the brain but also to comprehend the pathogenesis of important diseases, with high social impact, such as Alzheimer or multiple sclerosis. Arterial spin labeling (ASL) allows the non-invasive imaging of cerebral perfusion without the necessity of exogenous tracers. Quantification of ASL can be performed by using the simple Buxton model, that makes many assumptions, returning a simplified description of the endogenous tracer kinetic that is far from the real complexity of the phenomenon. Quantification of ASL can be also attached by using more complex structures allowing a better description of the system and the estimation of additional physiological information.

In this thesis, it has been shown how it is possible to use Bayesian model-based or model-free deconvolution strategies to model the peculiarities of the system without the simplifications used by the Buxton model. Two different and relevant ASL MR images have been considered due to their impact also in the current

clinical studies.
QUASAR is a very powerful technique already used in clinical environments that however suffers the lack of robustness of conventional analysis methods. In this work a new method based on Stable Spline kernel to perform deconvolution has been proposed. It is able to overcome the major problems of standard SVD-based deconvolution techniques and can reduce the delay sensitivity characteristic of ASL acquisitions performed with QUASAR.
Furthermore, it has also been shown how it is possible to enrich existing models to better cope with physiology and acquisition effects on the signal. Finally a comparison between the model-based and deconvolution approaches has been carried out, pointing out that the two methodologies are alternative and can exhibit different results.
pCASL labeling, developed to enhance signal-to-noise ratio and considered as the gold standard in clinical application for ASL, has been combined with a Look & Locker readout to allow the use of complex model in the estimation. Data acquired with this sequence have been analyzed with a new Bayesian Maximum a posteriori estimator to correct macro vascular artifacts and to provide supplementary information on the macro vascular component. It has been shown how it is possible to take advantage of using vascular crushing gradients, also in the modeling and estimation steps, to recover both micro and macro vascular components descriptions. These results, evaluated on healthy subjects, are promising. Therefore this technique will soon be applied to study pathological conditions, i.e. tumors in collaboration with Dr. Carlo Boffano, IRCSS C. Besta, Milan, Italy and multiple sclerosis in collaboration with Dr. Massimilano Calabrese, Neurology Section of Department of Neurological and Movement Sciences ,University of Verona, Italy. Thanks to the higher number of parameters that can be estimated, it is likely that a deeper description of the pathology under examination can be provided.
Eventually, an improved method to estimate labeling efficiency in-vivo from phase contrast images has been presented. This method can potentially be used with every ASL technique to improve the quantification process, making the absolute quantification more precise. It is applicable on large datasets in a completely automatic pipeline.

Bibliography

Ahlgren, A., Wirestam, R., Petersen, E. T., Stå hlberg, F., and Knutsson, L. Perfusion quantification by model-free arterial spin labeling using nonlinear stochastic regularization deconvolution. *Magn. Reson. Med.*, 70(5):1470–80, 2013.

Ahn, C. B., Lee, S. Y., Nalcioglu, O., and Cho, Z. H. The effects of random directional distributed flow in nuclear magnetic resonance imaging. *Med. Phys.*, 14(1):43–8, 1987.

Alsop, D. C. and Detre, J. a. Reduced transit-time sensitivity in noninvasive magnetic resonance imaging of human cerebral blood flow. *J. Cereb. Blood Flow Metab.*, 16(6):1236–49, 1996. ISSN 0271-678X.

Aslan, S., Xu, F., Wang, P. L., Uh, J., Yezhuvath, U. S., van Osch, M., and Lu, H. Estimation of labeling efficiency in pseudocontinuous arterial spin labeling. *Magn. Reson. Med.*, 63(3):765–71, 2010.

Avants, B. B., Tustison, N. J., Song, G., Cook, P. a., Klein, A., and Gee, J. C. A reproducible evaluation of ANTs similarity metric performance in brain image registration. *Neuroimage*, 54(3):2033–44, 2011. ISSN 1095-9572.

Azzalini, A. The skew-normal distribution and related multivariate families*. *Scandinavian Journal of Statistics*, 32(2):159–188, 2005.

Bakker, C. J. G., Hartkamp, M. J., and Mali, W. Measuring blood flow by nontriggered 2D phase-contrast {MR} angiography. *Magn. Reson. Imaging*, 14(6):609–614, 1996.

Balteau, E., Vidorreta, M., Fernandez-Seara, M. A., De Vita, E., and Thomas, D. L. New segmentation scheme for improved point spread function in multi-shot 3d-grase pcasl. *ESMRMB 2013, 30th Annu. Sci. Meet. Toulouse, Fr. 3-5 Oct. Abstr. Friday, Magn. Reson. Mater. Physics, Biol. Med.*, 26(S1):259–260, 2013.

Barbier, E., Silva, A., Kim, S., and Koretsky, A. Perfusion imaging using dynamic arterial spin labeling (dasl). *Magnetic Resonance in Medicine*, 45(6):1021–1029, 2001.

Bernstein, M., King, K., and Zhou, X. *Handbook of MRI Pulse Sequences*. Elsevier Science, 2004.

Boscolo Galazzo, I., Chappell, M. A., Thomas, D. L., Manganotti, P., and De Vita, E. Evaluation of an improved framework for minimizing blurring artifacts in 3D-GRASE Arterial Spin Labeling data. *ESMRMB 2013, 30th Annu. Sci. Meet. Toulouse, Fr. 3-5 Oct. Abstr. Friday, Magn. Reson. Mater. Physics, Biol. Med.*, 26(S1):258–259, 2013.

Brookes, M. J., Morris, P. G., Gowland, P. a., and Francis, S. T. Noninvasive measurement of arterial cerebral blood volume using Look-Locker EPI and arterial spin labeling. *Magn. Reson. Med.*, 58(1):41–54, 2007.

Buxton, R. B., Frank, L. R., Wong, E. C., Siewert, B., Warach, S., and Edelman, R. R. A general kinetic model for quantitative perfusion imaging with arterial spin labeling. *Magn. Reson. Med.*, 40(3):383–96, 1998.

Buxton, R. *Introduction to functional magnetic resonance imaging: principles and techniques*. Cambridge University press, Cambridge UK, 2002.

Buxton, R. B. Quantifying cbf with arterial spin labeling. *Journal of magnetic resonance imaging*, (22):723–726, 2005.

Canny, J. A computational approach to edge detection. *IEEE Trans. Pattern Anal. Mach. Intell.*, 8(6):679–98, 1986.

Carson, E. and Cobelli, C. *Modelling methodology for physiology and medicine*. Academic press, 2001.

Chappell, M., a.R. Groves, Whitcher, B., and Woolrich, M. Variational Bayesian Inference for a Nonlinear Forward Model. *IEEE Trans. Signal Process.*, 57(1):223–236, 2009.

Chappell, M. a., MacIntosh, B. J., Donahue, M. J., Günther, M., Jezzard, P., and Woolrich, M. W. Separation of macrovascular signal in multi-inversion time arterial spin labelling MRI. *Magn. Reson. Med.*, 63(5): 1357–65, 2010.

Chappell, M. a., Woolrich, M. W., Kazan, S., Jezzard, P., Payne, S. J., and MacIntosh, B. J. Modeling dispersion in arterial spin labeling: validation using dynamic angiographic measurements. *Magn. Reson. Med.*, 69(2):563–70, 2013a.

Chappell, M. a., Woolrich, M. W., Petersen, E. T., Golay, X., and Payne, S. J. Comparing model-based and model-free analysis methods for QUASAR arterial spin labeling perfusion quantification. *Magn. Reson. Med.*, 69(5):1466–75, 2013b.

Chen, Y., Wang, D. J. J., and Detre, J. A. Comparison of arterial transit times estimated using arterial spin labeling. *MAGMA*, 25(2):135–44, 2011.

Cobelli, C., Foster, D., and Toffolo, G. *Tracer kinetics in biomedical research*. Kluwer academic publisher, 2002.

Coleman, T. F. and Lii, Y. An interior, trust region approach for nonlinear minimization subject to bounds. *SIAM Journal on Optimization*, 6:418–445, 1996.

Coleman, T. F. and Li, Y. An interior trust region approach for nonlinear minimization subject to bounds. *SIAM Journal on optimization*, 6(2):418–445, 1996.

Dai, W., Garcia, D., de Bazelaire, C., and Alsop, D. C. Continuous flow-driven inversion for arterial spin labeling using pulsed radio frequency and gradient fields. *Magn. Reson. Med.*, 60:1488–97, 2008.

Dai, W., Shankaranarayanan, A., and Alsop, D. C. Volumetric measurement of perfusion and arterial transit delay using hadamard encoded continuous arterial spin labeling. *Magnetic Resonance in Medicine*, 2012.

Detre, J. A., Leigh, J. S., Williams, D. S., and Koretsky, A. P. Perfusion imaging. *Magn. Reson. Med.*, 23(1):37–45, January 1992.

Dixon, W. T., Du, L. N., Faul, D. D., Gado, M., and Rossnick, S. Projection angiograms of blood labeled by adiabatic fast passage. *Magn. Reson. Med.*, 3(3):454–62, 1986.

Duhamel, G., de Bazelaire, C., and Alsop, D. C. Evaluation of systematic quantification errors in velocity-selective arterial spin labeling of the brain. *Magn. Reson. Med.*, 50(1):145–53, 2003.

Edelman, R. R., Siewert, B., Darby, D. G., Thangaraj, V., Nobre, A. C., Mesulam, M. M., and Warach, S. Qualitative mapping of cerebral blood flow and functional localization with echo-planar MR imaging and signal targeting with alternating radio frequency. *Radiology*, 192(2):513–20, 1994. ISSN 0033-8419.

Edelman, R. R. and Chen, Q. EPISTAR MRI: Multislice mapping of cerebral blood flow. *Magn. Reson. Med.*, 40(6):800–805, 1998.

Figueiredo, P. M., Clare, S., and Jezzard, P. Quantitative perfusion measurements using pulsed arterial spin labelling: effects of large region-of-interest analysis. *Journal of magnetic resonance imaging*, 21:676–682, 2005.

Francis, S. T., Bowtell, R., and Gowland, P. a. Modeling and optimization of Look-Locker spin labeling for measuring perfusion and transit time changes in activation studies taking into account arterial blood volume. *Magn. Reson. Med.*, 59(2):316–25, 2008.

Frank, L. R., Lu, K., and Wong, E. C. Perfusion tensor imaging. *Magn. Reson. Med.*, 60(6):1284–91, 2008. doi: 10.1002/mrm.21806.

Garcia, D. M., Duhamel, G., and Alsop, D. C. Efficiency of inversion pulses for background suppressed arterial spin labeling. *Magn. Reson. Med.*, 54(2):366–72, 2005.

Golay, X., Stuber, M., Pruessmann, K. P., Meier, D., and Boesiger, P. Transfer insensitive labeling technique (TILT): application to multislice functional perfusion imaging. *J. Magn. Reson. Imaging*, 9(3):454–61, 1999.

Golay, X., Petersen, E. T., and Hui, F. Pulsed star labeling of arterial regions (PULSAR): a robust regional perfusion technique for high field imaging. *Magn. Reson. Med.*, 53(1):15–21, 2005.

Gowland, P. and Mansfield, P. Accurate measurement of T1in vivo in less than 3 seconds using echo-planar imaging. *Magn. Reson. Med.*, 30 (3):351–354, 1993.

Gowland, P. A. and Leach, M. O. Fast and accurate measurements of T1 using a multi-readout single inversion-recovery sequence. *Magn. Reson. Med.*, 26(1):79–88, 1992.

Grabner, G., Janke, A., Budge, M., Smith, D., Pruessner, J., and Collins, D. Symmetric atlasing and model based segmentation: An application to the hippocampus in older adults. In *Medical Image Computing and Computer-Assisted Intervention MICCAI 2006*, volume 4191 of *Lecture Notes in Computer Science*, pages 58–66. Springer Berlin Heidelberg, 2006. ISBN 978-3-540-44727-6.

Günther, M., Bock, M., and Schad, L. R. Arterial spin labeling in combination with a look-locker sampling strategy: inflow turbo-sampling EPI-FAIR (ITS-FAIR). *Magn. Reson. Med.*, 46(5):974–84, 2001.

Günther, M., Oshio, K., and Feinberg, D. a. Single-shot 3D imaging techniques improve arterial spin labeling perfusion measurements. *Magn. Reson. Med.*, 54(2):491–8, 2005.

Haacke, E., Brown, R., Thompson, M., and Venkatesan, R. *Magnetic Resonance Imaging:Imaging: Physical Principles and Sequence Design*. John Wiley and Sons New York, 1999.

Hahn, E. L. Spin echoes. *Phys. Rev.*, 80:580–594, 1950.

Harbe, J. and Lewis, D. P. Two analytical solutions for model of pulsed arterial spin labeling with randomized blood arrival times. *Journal of magnetic resonance imaging*, 167:49–55, 2004.

Hartkamp, N. S., Helle, M., Chappell, M. A., Okell, T. W., Hendrikse, J., Bokkers, R. P. H., and van Osch, M. J. P. Validation of planning-free vessel-encoded pseudo-continuous arterial spin labeling MR imaging as territorial-ASL strategy by comparison to super-selective p-CASL MRI. *Magn. Reson. Med.*, July 2013.

Helpern, J. A., Branch, C. A., Yongbi, M. N., and Huang, N. C. Perfusion imaging by un-inverted flow-sensitive alternating inversion recovery (UNFAIR). *Magn. Reson. Imaging*, 15(2):135–9, 1997.

Herscovitch, P. and Raichle, M. E. What is the correct value for the brain-blood partition coefficient for water? *J. Cereb. Blood Flow Metab.*, 5(1): 65–9, 1985.

Hofman, M. B., Kouwenhoven, M., Sprenger, M., van Rossum, A. C., Valk, J., and Westerhof, N. Nontriggered magnetic resonance velocity measurement of the time-average of pulsatile velocity. *Magn. Reson. Med.*, 29(5):648–55, 1993.

Jenkinson, M., Beckmann, C. F., Behrens, T. E. J., Woolrich, M. W., and Smith, S. M. FSL. *Neuroimage*, 62(2):782–90, 2012.

Kim, S.-G. Quantification of relative cerebral blood flow change by flow-sensitive alternating inversion recovery (FAIR) technique: Application to functional mapping. *Magn. Reson. Med.*, 34(3):293–301, 1995.

Krejza, J., Arkuszewski, M., Kasner, S. E., Weigele, J., Ustymowicz, A., Hurst, R. W., Cucchiara, B. L., and Messe, S. R. Carotid artery diameter in men and women and the relation to body and neck size. *Stroke.*, 37 (4):1103–5, 2006.

Kwong, K. K., Chesler, D. A., Weisskoff, R. M., Donahue, K. M., Davis, T. L., Ostergaard, L., Campbell, T. A., and Rosen, B. R. Mr perfusion studies witht1-weighted echo planar imaging. *Magn. Reson. Med.*, 34 (6):878–887, 1995.

Look, D. C. and Locker, D. R. Time Saving in Measurement of NMR and EPR Relaxation Times. *Rev. Sci. Instrum.*, 41(2):250, 1970.

Lu, H., Clingman, C., Golay, X., and van Zijl, P. C. M. Determining the longitudinal relaxation time (T1) of blood at 3.0 Tesla. *Magn. Reson. Med.*, 52(3):679–82, 2004.

Luh, W. M., Wong, E. C., Bandettini, P. a., and Hyde, J. S. QUIPSS II with thin-slice TI1 periodic saturation: a method for improving accuracy of quantitative perfusion imaging using pulsed arterial spin labeling. *Magn. Reson. Med.*, 41(6):1246–54, 1999.

Maccotta, L., Detre, J. a., and Alsop, D. C. The efficiency of adiabatic inversion for perfusion imaging by arterial spin labeling. *NMR Biomed.*, 10(4-5):216–21, 1997.

MacIntosh, B. J., Lindsay, a. C., Kylintireas, I., Kuker, W., Günther, M., Robson, M. D., Kennedy, J., Choudhury, R. P., and Jezzard, P. Multiple inflow pulsed arterial spin-labeling reveals delays in the arterial arrival time in minor stroke and transient ischemic attack. *AJNR. Am. J. Neuroradiol.*, 31(10):1892–4, 2010a.

MacIntosh, B. J., Filippini, N., Chappell, M. a., Woolrich, M. W., Mackay, C. E., and Jezzard, P. Assessment of arterial arrival times derived from multiple inversion time pulsed arterial spin labeling MRI. *Magn. Reson. Med.*, 63(3):641–7, 2010b.

Mai, V. M., Hagspiel, K. D., Christopher, J. M., Do, H. M., Altes, T., Knight-Scott, J., Stith, A. L., Maier, T., and Berr, S. S. Perfusion imaging of the human lung using flow-sensitive alternating inversion recovery with an extra radiofrequency pulse (FAIRER). *Magn. Reson. Imaging*, 17 (3):355–61, 1999.

Mak, H. K. F., Chan, Q., Zhang, Z., Petersen, E. T., Qiu, D., Zhang, L., Yau, K. K. W., Chu, L.-W., and Golay, X. Quantitative assessment of cerebral hemodynamic parameters by QUASAR arterial spin labeling in Alzheimer's disease and cognitively normal Elderly adults at 3-tesla. *J. Alzheimers. Dis.*, 31(1):33–44, 2012.

Mani, S., Pauly, J., Conolly, S., Meyer, C., and Nishimura, D. Background suppression with multiple inversion recovery nulling: Applications to projective angiography. *Magn. Reson. Med.*, 37(6):898–905, 1997.

Maumet, C., Maurel, P., Ferré, J.-C., and Barillot, C. Robust perfusion maps in Arterial Spin Labeling by means of M-estimators. In *Proceedings ISMRM 2013*, page 3037, Salt Lake City, United States, April 2013.

Meakin, J. a. and Jezzard, P. An optimized velocity selective arterial spin labeling module with reduced eddy current sensitivity for improved perfusion quantification. *Magn. Reson. Med.*, 69(3):832–8, 2013.

Mitchell, J. and McKay, A. Comparison of left and right vertebral artery intracranial diameters. *Anat. Rec.*, 242(3):350–4, 1995.

Nishimura, D. G., Macovski, A., Pauly, J. M., and Conolly, S. M. MR angiography by selective inversion recovery. *Magn. Reson. Med.*, 4(2): 193–202, 1987.

Noguchi, T., Yoshiura, T., Hiwatashi, A., Togao, O., Yamashita, K., Nagao, E., and Honda, H. Arterial spin-labeling magnetic resonance imaging: the timing of regional maximal perfusion-related signal intensity revealed by a multiphase technique. *Jpn. J. Radiol.*, 30(2):137–45, 2012.

Norris, D. G. High field human imaging. *J. Magn. Reson. Imaging*, 18(5): 519–29, 2003.

Ogg, R. J., Kingsley, P. B., and Taylor, J. S. WET, a T1- and B1-insensitive water-suppression method for in vivo localized 1H NMR spectroscopy. *J. Magn. Reson. B*, 104(1):1–10, 1994.

Okell, T. W., Chappell, M. a., Woolrich, M. W., Günther, M., Feinberg, D. a., and Jezzard, P. Vessel-encoded dynamic magnetic resonance angiography using arterial spin labeling. *Magn. Reson. Med.*, 64(2):430–8, 2010.

Okell, T. W., Chappell, M. a., Schulz, U. G., and Jezzard, P. A kinetic model for vessel-encoded dynamic angiography with arterial spin labeling. *Magn. Reson. Med.*, c:1–11, 2012.

Okell, T. W., Chappell, M. A., Kelly, M. E., and Jezzard, P. Cerebral blood flow quantification using vessel-encoded arterial spin labeling. *J. Cereb. Blood Flow Metab.*, 33(11):1716–24, 2013.

Oshio, K. and Feinberg, D. A. GRASE (Gradient- and spin-echo) imaging: a novel fast MRI technique. *Magn. Reson. Med.*, 20(2):344–9, 1991.

Østergaard, L., Weisskoff, R. M., Chesler, D. A., Gyldensted, C., and Rosen, B. R. High resolution measurement of cerebral blood flow using intravascular tracer bolus passages. part i: Mathematical approach and statistical analysis. *Magnetic Resonance in Medicine*, 36(5):715–725, 1996.

Otsu, N. A Threshold Selection Method from Gray-Level Histograms. *IEEE Trans. Syst. Man. Cybern.*, 9(1):62–66, 1979.

Paling, D., Thade Petersen, E., Tozer, D. J., Altmann, D. R., Wheeler-Kingshott, C. A., Kapoor, R., Miller, D. H., and Golay, X. Cerebral arterial bolus arrival time is prolonged in multiple sclerosis and associated with disability. *J. Cereb. Blood Flow Metab.*, (April):1–9, September 2013.

Parkes, L. M. Quantification of cerebral perfusion using arterial spin labeling: two-compartment models. *J. Magn. Reson. Imaging*, 22(6):732–6, 2005.

Parkes, L. M. and Tofts, P. S. Improved accuracy of human cerebral blood perfusion measurements using arterial spin labeling: accounting for capillary water permeability. *Magn. Reson. Med.*, 48(1):27–41, 2002.

Peruzzo, D., Zanderigo, F., Bertoldo, A., Pillonetto, G., Cosottini, M., and Cobelli, C. Assessment of clinical data of nonlinear stochastic deconvolution versus block-circulant singular value decomposition for quantitative dynamic susceptibility contrast magnetic resonance imaging. *Magn. Reson. Imaging*, 29(7):927–36, 2011.

Petersen, E. T., Lim, T., and Golay, X. Model-free arterial spin labeling quantification approach for perfusion MRI. *Magn. Reson. Med.*, 55(2): 219–32, 2006.

Petersen, E. T., Golay, X., and study, T. Q. R. The effect of bolus length and dispersion on Arterial Spin Labeling flow quantification. In *18th Annu. Meet. Exihibition Int. Soc. Magn. Reson. Med. (ISMRM 2010), Stock. Sweden, 30 April. May 2010. Proc. 18th ISMRM, 2010, no. 514*, page 514, 2010a.

Petersen, E. T., Mouridsen, K., and Golay, X. The QUASAR reproducibility study, Part II: Results from a multi-center Arterial Spin Labeling test-retest study. *Neuroimage*, 49(1):104–13, 2010b.

Petr, J., Schramm, G., Hofheinz, F., Langner, J., and van den Hoff, J. Partial volume correction in arterial spin labeling using a Look-Locker sequence. *Magn. Reson. Med.*, 70(6):1535–43, 2013.

Pillonetto, G. and De Nicolao, G. A new kernel-based approach for linear system identification. *Automatica*, 46(1):81–93, 2010.

Popescu, V., Battaglini, M., Hoogstrate, W. S., Verfaillie, S. C. J., Sluimer, I. C., van Schijndel, R. a., van Dijk, B. W., Cover, K. S., Knol, D. L., Jenkinson, M., Barkhof, F., de Stefano, N., and Vrenken, H. Optimizing parameter choice for FSL-Brain Extraction Tool (BET) on 3D T1 images in multiple sclerosis. *Neuroimage*, 61(4):1484–94, 2012.

Schepers, J., Van Osch, M. J. P., and Nicolay, K. Effect of vascular crushing on FAIR perfusion kinetics, using a BIR-4 pulse in a magnetization prepared FLASH sequence. *Magn. Reson. Med.*, 50(3):608–13, 2003.

Schmid, S., Ghariq, E., Teeuwisse, W. M., Webb, A., and van Osch, M. J. P. Acceleration-selective arterial spin labeling. *Magn. Reson. Med.*, 71(1): 191–9, 2014.

Shin, D. D., Liu, T. T., Wong, E. C., Shankaranarayanan, A., and Jung, Y. Pseudocontinuous arterial spin labeling with optimized tagging efficiency. *Magn. Reson. Med.*, 68(4):1135–44, 2012.

Smith, S. M. Fast robust automated brain extraction. *Hum. Brain Mapp.*, 17(3):143–55, 2002.

Sousa, I., Vilela, P., and Figueiredo, P. Reproducibility of the quantification of arterial and tissue contributions in multiple postlabeling delay

arterial spin labeling. *Journal of Magnetic Resonance Imaging*, page Epub ahead of print, 2013. doi: 10.1002/jmri.24493.

Spilt, A., Box, F. M. a., van der Geest, R. J., Reiber, J. H. C., Kunz, P., Kamper, A. M., Blauw, G. J., and van Buchem, M. a. Reproducibility of total cerebral blood flow measurements using phase contrast magnetic resonance imaging. *J. Magn. Reson. Imaging*, 16(1):1–5, 2002.

St Lawrence, K. S., Frank, J. a., and McLaughlin, a. C. Effect of restricted water exchange on cerebral blood flow values calculated with arterial spin tagging: a theoretical investigation. *Magn. Reson. Med.*, 44(3):440–9, 2000.

Sutera, S. P. and Skalak, R. The History of Poiseuille's Law. *Annu. Rev. Fluid Mech.*, 25(1):1–20, 1993.

Teeuwisse, W. M., Schmid, S., Ghariq, E., Veer, I. M., and van Osch, M. J. Time-encoded pseudocontinuous arterial spin labeling: Basic properties and timing strategies for human applications. *Magnetic Resonance in Medicine*, page In press, 2014.

van Osch, M. J. P., Teeuwisse, W. M., van Walderveen, M. a. a., Hendrikse, J., Kies, D. a., and van Buchem, M. a. Can arterial spin labeling detect white matter perfusion signal? *Magn. Reson. Med.*, 62(1):165–73, 2009.

Vidorreta, M., Wang, Z., Rodríguez, I., Pastor, M. a., Detre, J. a., and Fernández-Seara, M. a. Comparison of 2D and 3D single-shot ASL perfusion fMRI sequences. *Neuroimage*, 66C:662–671, 2012.

Wells, J. A., Lythgoe, M. F., Gadian, D. G., Ordidge, R. J., and Thomas, D. L. In vivo hadamard encoded continuous arterial spin labeling (h-casl). *Magnetic Resonance in Medicine*, 63(4):1111–1118, 2010a.

Wells, J. a., Thomas, D. L., King, M. D., Connelly, A., Lythgoe, M. F., and Calamante, F. Reduction of errors in ASL cerebral perfusion and arterial transit time maps using image de-noising. *Magn. Reson. Med.*, 64(3):715–24, 2010b.

Williams, D., Detre, J., Leigh, J., and Koretsky, A. Magnetic resonance imaging of perfusion using spin inversion of arterial water. *Proc. Natl. Acad. Sci.*, 89(1):212, 1992.

Wong, E. C., Buxton, R. B., and Frank, L. R. Quantitative imaging of perfusion using a single subtraction (QUIPSS and QUIPSS II). *Magn. Reson. Med.*, 39(5):702–8, 1998.

Wong, E. C., Buxton, R. B., and Frank, L. R. Implementation of quantitative perfusion imaging techniques for functional brain mapping using pulsed arterial spin labeling. *NMR Biomed.*, 10(4-5):237–49, 1997.

Wong, E. C., Cronin, M., Wu, W.-C., Inglis, B., Frank, L. R., and Liu, T. T. Velocity-selective arterial spin labeling. *Magn. Reson. Med.*, 55(6):1334–41, 2006.

Wu, O., Ø stergaard, L., Weisskoff, R. M., Benner, T., Rosen, B. R., and Sorensen, a. G. Tracer arrival timing-insensitive technique for estimating flow in MR perfusion-weighted imaging using singular value decomposition with a block-circulant deconvolution matrix. *Magn. Reson. Med.*, 50(1):164–74, 2003.

Wu, W.-C. and Wong, E. C. Intravascular effect in velocity-selective arterial spin labeling: the choice of inflow time and cutoff velocity. *Neuroimage*, 32(1):122–8, 2006.

Wu, W.-C., Jiang, S.-F., Yang, S.-C., and Lien, S.-H. Pseudocontinuous arterial spin labeling perfusion magnetic resonance imaging–a normative study of reproducibility in the human brain. *Neuroimage*, 56(3): 1244–50, 2011.

Wu, W.-C., Lin, S.-C., Wang, D. J., Chen, K.-L., and Li, Y.-D. Measurement of Cerebral White Matter Perfusion Using Pseudocontinuous Arterial Spin Labeling 3T Magnetic Resonance Imaging - an Experimental and Theoretical Investigation of Feasibility. *PlosONE*, 8(12):e82679, 2013.

Xie, J., Gallichan, D., Gunn, R. N., and Jezzard, P. Optimal design of pulsed arterial spin labeling MRI experiments. *Magn. Reson. Med.*, 59 (4):826–34, 2008.

Ye, F. Q., Frank, J. a., Weinberger, D. R., and McLaughlin, a. C. Noise reduction in 3D perfusion imaging by attenuating the static signal in arterial spin tagging (ASSIST). *Magn. Reson. Med.*, 44(1):92–100, 2000.

Ye, F. Q., Mattay, V. S., Jezzard, P., Frank, J. A., Weinberger, D. R., and McLaughlin, A. C. Correction for vascular artifacts in cerebral blood flow values measured by using arterial spin tagging techniques. *Magn. Reson. Med.*, 37(2):226–235, 1997.

Zanderigo, F., Bertoldo, A., Pillonetto, G., and Cobelli Ast, C. Nonlinear stochastic regularization to characterize tissue residue function

in bolus-tracking MRI: assessment and comparison with SVD, block-circulant SVD, and Tikhonov. *IEEE Trans. Biomed. Eng.*, 56(5):1287–97, 2009.

Zhang, Y., Brady, M., and Smith, S. Segmentation of brain mr images through a hidden markov random field model and the expectation-maximization algorithm. *Medical Imaging, IEEE Transactions on*, 20(1): 45–57, 2001.

Acknowledgments

Above all else, I would like to state my thankfulness to my advisor Prof. Alessandra Bertoldo for the tireless support, motivation and spur to do that she disclosed during these three years. Thanks for all the opportunities given to me. I would not expect a better mentor.
A great thank must go to my colleagues at the department of information engineering, Prof. Enrico Grisan, Denis Peruzzo, Mattia Veronese, Elisa Veronese, Gaia Rizzo, Letizia Squarcina and Enea Poletti that helped me every time I asked.
To the crew of the "PhD Student's room" , Mattia Zanon, Federica Eduati, Francesco Micheletto, Anna Largajolli and Elisabetta Pasqualotto: we had great time together.
A special thank should go to Dr. Michael Chappell, Amit Mehndiratta and Ilaria Boscolo Galazzo, we worked in armory in Oxford.
Thanks to everyone that contribute to the realization of this work.